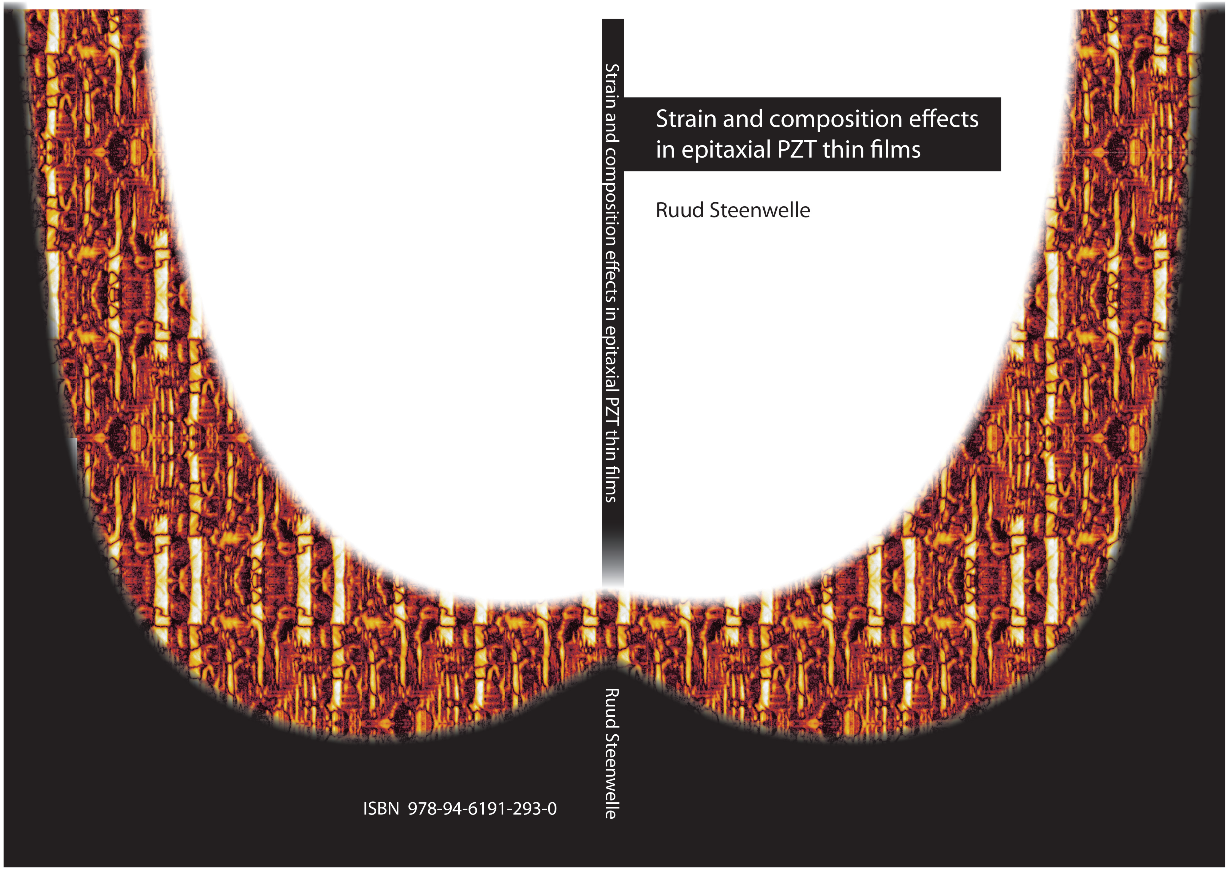

Strain and composition effects in epitaxial PZT thin films

Ruud Steenwelle

Strain and composition effects in epitaxial PZT thin films

Ruud Steenwelle

ISBN 978-94-6191-293-0

Op 11 mei 2012
verdedig ik mijn proefschrift

Strain and composition effects in epitaxial PZT thin films

in de Prof. dr. G. Berkhoff-zaal
van gebouw de Waaier
van de Universiteit Twente.

Om 16:30 zal ik een
inleiding geven.
De verdediging start
om 16:45.
Aansluitend vindt een
receptie plaats.

Tevens bent u van harte
uitgenodigd voor het feest
in "Cafe de Pimpelaar"
Oude Markt 22, Enschede
vanaf 21:00 uur

Ruud Steenwelle
S.L. Louwesstraat 198
7545 EZ Enschede

Paranimfen:
Xin Wan
Jeroen Stopel

Strain and composition effects in epitaxial PZT thin films

Ruud Steenwelle

Cover

The cover image shows the domain structure of a 1 μm $Pb(Zr_{0.2},Ti_{0.8})O_3$ thin film deposited on a $DyScO_3$ substrate with a 100 nm $SrRuO_3$ bottom electrode, using the amplitude of the in-plane signal of a Piezo Force Microscope. The macroscopic shape of the image is derived from the ferroelectric double-well potential for different strain states, as is used in Landau-Devonshire phenomenological modelling.

Ph.D. committee

Chairman and secretary
    Prof. dr. Gerard van der Steenhoven (University of Twente)

Supervisors
    Prof. dr. ing. Guus Rijnders (University of Twente)
    Prof. dr. ing. Dave Blank (University of Twente)

Assistant supervisor
    Dr. ir. Gertjan Koster (University of Twente)

Members
    Prof. dr. Kathrin Dörr (MLU Halle-Wittenberg)
    Prof. dr. ir. Sybrand van der Zwaag (Technical University of Delft)
    Prof. dr. ir. Rob Lammertink (University of Twente)
    Prof. dr. Han Gardeniers (University of Twente)

Paranymphs

Xin Wan MSc.
Ing. Jeroen Stopel

The research described in this thesis was performed with the Inorganic Materials Science group and the MESA+ Institute for Nanotechnology at the University of Twente, Enschede, the Netherlands. The authors gratefully acknowledge the support of the SmartMix Programme 'Smartpie' of the Netherlands Ministry of Economic Affairs and the Netherlands Ministry of Education, Culture and Science.

R.J.A. Steenwelle
Strain and composition effects in epitaxial PZT thin films

Ph.D. thesis University of Twente, Enschede, the Netherlands.
ISBN 978-94-6191-293-0

Printed by Ipskamp Drukkers, Enschede, The Netherlands

STRAIN AND COMPOSITION EFFECTS IN EPITAXIAL PZT THIN FILMS

PROEFSCHRIFT

ter verkrijging van
de graad van doctor aan de Universiteit Twente,
op gezag van de rector magnificus,
prof. dr. H. Brinksma,
volgens besluit van het College voor Promoties
in het openbaar te verdedigen
op vrijdag 11 mei 2012 om 16:45 uur

door

Ruud Johannes Antonius Steenwelle

geboren op 14 januari 1983
te Almelo

Dit proefschrift is goedgekeurd door de promotoren
Prof. dr. ing. A.J.H.M. Rijnders
Prof. dr. ing. D.H.A. Blank

en de assistent-promotor
Dr. ir. G. Koster

Contents

Chapter 1

Introduction

Piezoelectric materials are able to convert electrical energy into mechanical energy and vice versa. The word *piezoelectric* is derived from the Greek *piezein*, which means to squeeze or to press, and *electron*, which stands for amber, an ancient source of electric charge [1]. Piezoelectricity was discovered in 1880 by the Curie brothers in quartz and rochelle salt. Since the fifties of the twentieth century, the attention shifted towards lead zirconate titanate (Pb(Zr,Ti)O_3, PZT), as it has high electromechanical coupling coefficients in a wide temperature range. In the meantime, a multi-billion dollar industry is already aware of the technological capabilities of this material. Prominent applications range from fuel-injection systems to lighters and from switches to ultrasound systems.

In traditional piezo technology, powders are sintered into bulk crystals and processed using coarse techniques such as grinding, sawing, glueing. However, these methods are less suitable on length-scales well-below a millimeter. Therefore, a different approach is developed: by depositing a layer of piezoelectric material onto a substrate in combination with the use of accurate patterning techniques, piezoelectric Micro Electro Mechanical Systems (piezoMEMS) are developed [2, 3]. This technology is capable of fabricating thousands of actuating or sensing devices simultaneously on a silicon wafer, leading to a drastic reduction of the cost per device. The resulting devices are characterized by high sensitivity, low power consumption and relatively straightforward operation. Applications of PiezoMEMS are inkjet printing, radio frequency (RF) MEMS, auto-focussing for smartphone cameras, piezoelectric Micromachined Ultrasound Transducers (pMUT) [4], micro-valves, micro-mirrors, or even *in vivo* sensors or energy-harvesters [5, 6]. Regarding the patterning of devices, an extensive toolbox with methods is available, consisting of processes related to CMOS technologies [7], such as chemical etching, physical etching in combination with optical lithography, or more experimental techniques such as ion-beam milling, shadow-masked deposition or self-assembly [8].

The PZT thin films can be deposited by chemical methods [9–11], or physical vapor deposition [12–15]. An important advantage of PZT thin film growth over bulk processing, is the ability to grow relatively easily single crystalline materials.

The epitaxial relation between the substrate, buffer layers, electrodes and film can be maintained throughout a complete multilayer stack. In this way, it is possible to optimize the properties of PZT heterostructures along certain crystallographic directions and to study these properties without the undesirable effects of defects. An additional advantage is that no poling is needed after growth, since the ferroelectric domains are coherently oriented in the single crystalline matrix. However, the realization of such films on silicon substrates is challenging since only a few oxide materials are chemically stable in contact with silicon. The achievement of epitaxial buffer layers of yttria-stabilized zirconia [16] and strontium titanate [17] are part of an ongoing process to bring the oxide heterostructures into silicon technology [18, 19]. The integration of PiezoMEMS using (epitaxial) PZT films with silicon technology is seen as a pioneering technology in this process. Therefore it is necessary to explore new ways to fabricate PZT films on buffer layers. This is described in chapter 3, where PZT is grown by Pulsed Laser Deposition.

Pulsed laser deposition of PZT films at a high temperature and the subsequent cooling to room temperature introduces thermal strain due to the difference in thermal expansion coefficients between the film and the substrate. For thick PZT films (> 100 nm), the epitaxial strain is relaxed through formation of defects. On silicon, the PZT is under tensile strain, in contrast to the compressive strain on typical perovskite single crystalline substrates. The bulk unit-cell is deformed, which results in a change of symmetry. As a consequence, the functional properties polarization, dielectric constant, piezoelectric coefficient and transition temperature are altered. Next to the strain, the composition (the ratio between zirconium and titanium) of the solid solution PZT allows tuning of the crystallographic phase and properties. In bulk, the largest electromechanical properties are found at the structural phase boundary between the tetragonal and rhombohedral phase, the morphotropic phase boundary. In strained thin films the effect of composition is different from the bulk and the interaction of strain and composition results in phenomena that are not present in bulk. For example, crystallographic phase boundaries and the associated polarization states may be shifted as a function of composition. Certain new phases may be created of altered and intricate polydomain structures may be formed. Basically, two regimes can be recognized. The tetragonal phase at low Zr-content show large domains and the phase near the morphotropic phase boundary at intermediate Zr-content, does not show these large domains.

For the tetragonal PZT phase, a large spontaneous strain arises upon cooling through the ferroelectric transition, inducing domains with out-of-plane oriented polarization (c-domains) and domains with in-plane oriented polarization (a-domains) [20]. The fraction of the c-domains is sensitive to the substrate induced strain [21]. With increasing Zr content, the spontaneous strain decreases and the domain fractions become more sensitive to the thermal expansion coefficient of the substrate. In order to obtain crystallographic matching at the domain-wall between the c and a domains, a characteristic domain tilting is present in ferroelectric polydomain films. The absolute tilting angle of the individual domain depends on the substrate induced strain, while the relative tilt between the a and c-domains only depends on the composition controlled spontaneous strain. These

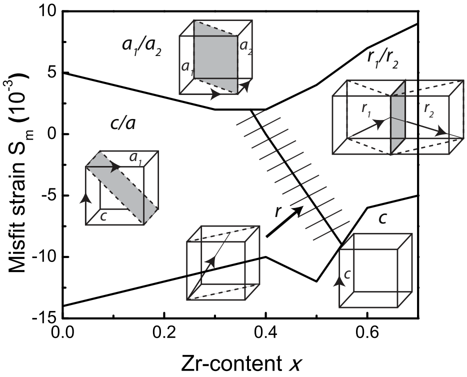

Figure 1.1: Phase diagram for $\mathrm{Pb(Zr}_x\mathrm{,Ti}_{1-x}\mathrm{)O}_3$ films at room temperature. Polarization states as a function of misfit strain and composition

aspects are discussed in chapter 4.

The crystallographic and functional properties of the compositional region near the morphotropic phase boundary (MPB) have been underexposed with respect to the tetragonal phase of PZT thin films. The reason for this is that several crystallographic changes are below the detection resolution, and that these changes are highly sensitive to external influences. For bulk, the explanation of the crystallography and properties near this composition are attempted using the coexistence of rhombohedral domains and tetragonal domains [22], the formation of a monoclinic crystal phase [23] and the presence nanoscale domains with low-domain wall energy [24]. Here, using composition and strain in single crystalline PZT thin films may elucidate certain aspects of these hypotheses. X-ray diffraction reveals ferroelectric domains with nanoscale dimensions by an interference effect. Indeed, piezo force microscopy and transmission electron microscopy suggest nanoscale domains below 20 nm in size. This phase shows a low or negative domain-wall energy, resulting in an adaptive phase for which the domain fraction can be easily adjusted in order to obtain stress relaxation. The lattice parameters that are obtained from x-ray diffraction as function of temperature, misfit strain and composition, closely agree to expectations using a model for this adaptive phase. In order to achieve this, an adjustment to the original adaptive phase theory has to be made that accounts for the thermal strain and the typical PZT domain structure consisting of a, b and c-domains. These described in chapter 5.

The properties of PZT films for all compositions and misfit strains can be understood with the use of thermodynamic Landau-Devonshire (LD) theory. From the minimization of the free energy as function of misfit strain, composition and temperature follows the crystallographic phase and its properties. A single domain model describes the effects on a uniformly polarized material [25]. A polydomain model extends the model for polydomain films [26]. Figure 1.1 shows a phase diagram for PZT films that is constructed with several polydomain polarization states. In general, the polarization vector is either oriented fully in-plane, fully out-of-plane, or is mixed in the in-plane and out-of-plane directions. The instabilities in the polarization at a phase boundary cause the divergence of the dielectric tensor [27] and the piezoelectric coefficients [28, 29]. These thermodynamic models have not been validated by experiments extensively in literature. In order to have an accurate comparison of the experimental and theoretical values, conventions for determining of the exact experimental misfit strain values of all single domain and polydomain phases need to be created. Subsequently, the experiments can be interpreted using the misfit strain / temperature phase diagram and the misfit strain / composition phase diagram. The experimental values of polarization, dielectric constant, piezoelectric coefficient and transition temperature show a remarkable good match to the phenomenological theory for several compositions and strain values, as described in chapter 6.

The application of PZT thin films in piezoMEMS can offer a compactness and resolution that is not readily achievable with current bulk piezoelectric ceramics technology. In order to show the applicability of PZT films by pulsed laser deposition, single element devices of PZT films on silicon membranes are fabricated and characterized as described in chapter 7.

1.1 References

[1] Online etymology dictionary, January 2012.

[2] S Tadigadapa and K Mateti. Piezoelectric mems sensors: state-of-the-art and perspectives. *Meas. Sci. Technol.*, 20(092001):1–30, 2009.

[3] H.A. Trolier-Mckinstry and P. Muralt. Thin film piezoelectrics for mems. *J. Electroceram.*, 12(1):7–17, 2004.

[4] D.E. Dausch, J.B. Castellucci, D.R. Chou, and O.T. van Ramm. Piezoelectric micromachined ultrasound transducer (pmut) arrays for 3d imaging probes. *IEEE Ultras. Symp.*, pages 930–933, Oct 2006.

[5] S. Roundy, V. Sundararajan, J. Baker, E. Carleton, E.K. Reilly, B. Otis, J.M. Rabaey, E.K. Reilly, and P.K. Wright. *Energy Scavenging in Support of Ambient Intelligence: Techniques, Challenges, and Future Directions*, volume AmIware: Hardware Technology Drivers of Ambient Intelligence, pages 265–284. Springer-Verlag, 2006.

[6] K.D. Wise. Integrated sensors, mems, and microsystems: Reflections on a fantastic voyage. *Sens. Act. A.*, 136(1):39–50, 2007.

[7] J. Baborowski. Microfabrication of piezoelectric mems. *J. Electroceram.*, 12(1):33–51, 2004.

[8] A. Rüdiger, T. Schneller, A. Roelofs, S. Tiedke, T. Schmitz-Kempen, and R. Waser. Nanosize ferroelectric oxides–tracking down the superparaelectric limit. *Appl. Phys. A.*, 80(6):1247–1255, 2005.

[9] T.A. Berfield, R.J. Ong, D. A. Payne, and N. R. Sottos. Residual stress effects on piezoelectric response of sol-gel derived lead zirconate titatnate thin films. *J Appl Phys*, 101(024102):1–7, 2007.

[10] Y. Otani, S. Okamura, and T. Shiosaki. Recent developments on mocvd of ferroelectric thin films. *J. Electroceram.*, 13(1):15–22, 2004.

[11] H.C. Lee and W.J. Lee. Characterization of $Pb(Zr, Ti)O_3$ thin films fabricated by plasma enhanced chemical vapor deposition on Ir-based electrodes. *J. Vac. Sci. Technol. A.*, 20:1939, 2002.

[12] T. Maeder, P. Muralt, L. Sagalowicz, and N. Setter. In-situ sputter deposition of pt and pzt films on platinum and RuO_2 electrodes. *Microel. eng.*, 29(1-4):177–180, 1995.

[13] B.E Park, S Shouriki, E Tokumitsu, and H Ishiwara. Fabrication of $PbZrTiO_3$ films on Si structures using Y_2O_3 buffer layers. *Jpn. J. Appl. Phys.*, 37:5145–5149, 1998.

[14] C.B. Eom, R.B. Van Dover, J.M. Phillips, D.J. Werder, J.H. Marshall, C.H. Chen, R.J. Cava, R.M. Fleming, and D.K. Fork. Fabrication and properties of epitaxial ferroelectric heterostructures with $SrRuO_3$ isotropic metallic oxide electrodes. *Appl. Phys. Lett.*, 63(18):2570–2572, 1993.

[15] J.F.M. Cillessen, M.W.J. Prins, and R.A. Wolf. Thickness dependence of the switching voltage in all-oxide ferroelectric thin-film capacitors prepared by pulsed laser deposition. *J. Appl. Phys.*, 81:2777, 1997.

[16] D.K. Fork, D.B. Fenner, A. Barrera, J.M. Phillips, T.H. Geballe, G.A.N. Connell, and J.B. Boyce. Buffer layers for high-quality epitaxial $YBCO$ films on Si. *IEEE Transact. Appl. Supercond.*, 1(1):67–73, 1991.

[17] R.A. McKee, F.J. Walker, and M.F. Chisholm. Crystalline oxides on silicon: The first five monolayers. *Phys. Rev. Lett.*, 81(14):3014–3017, 1998.

[18] P. Zubko, S. Gariglio, M. Gabay, P. Ghosez, and J.M. Triscone. Interface physics in complex oxide heterostructures. *Annu. Rev. Condens. Matter Phys.*, 2(1):141–165, 2011.

[19] J.W Park, D.F Bogorin, C Cen, D.A Felker, Y Zhang, C.T Nelson, C.W Bark, C.M Folkman, X.Q Pan, M.S Rzchowski, J Levy, and C.B Eom. Creation of a two-dimensional electron gas at an oxide interface on silicon. *Nat. Comm*, 1(7):1–6, Oct 2010.

[20] P.E Janolin. Strain on ferroelectric thin films. *J. Mater. Sci.*, 44:5025, 2009.

[21] J.S. Speck and W. Pompe. Domain configurations due to multiple misfit relaxation mechanisms in epitaxial ferroelectric thin films. I. theory. *J. Appl. Phys.*, 76:466, 1994.

[22] W. Cao and E. Cross. Theoretical model for the morphotropic phase boundary in lead zirconate–lead titanate solid solution. *Phys. Rev. B.*, 47(9):4825, 1993.

[23] B. Noheda, D.E. Cox, G. Shirane, J.A. Gonzalo, L.E. Cross, and S.E. Park. A monoclinic ferroelectric phase in the $Pb(Zr,Ti)O_3$ solid solution. *Appl. Phys. Lett.*, 74:2059, 1999.

[24] Y.M. Jin, Y.U. Wang, A.G. Khachaturyan, J. Li, and D. Viehland. Conformal miniaturization of domains with low domain-wall energy: Monoclinic ferroelectric states near the morphotropic phase boundaries. *Phys. Rev. Lett.*, 91(19):197601, 2003.

[25] N.A. Pertsev, V.G. Kukhar, H. Kohlstedt, and R. Waser. Phase diagrams and physical properties of single-domain epitaxial $Pb(Zr_{1-x},Ti_x)O_3$ thin films. *Phys. Rev. B.*, 67(5):054107, 2003.

[26] V.G. Kukhar, N.A. Pertsev, H. Kohlstedt, and R. Waser. Polarization states of polydomain epitaxial $Pb(Zr_{1-x},Ti_x)O_3$ thin films and their dielectric properties. *Phys. Rev. B.*, 73(21):214103, 2006.

[27] K.M. Rabe. Theoretical investigations of epitaxial strain effects in ferroelectric oxide thin films and superlattices. *Current opinion in solid state & materials science*, 9(3):122–127, 2005.

[28] N.A. Pertsev, A.G. Zembilgotov, and A.K. Tagantsev. Effect of mechanical boundary conditions on phase diagrams of epitaxial ferroelectric thin films. *Phys. Rev. Lett.*, 80(9):1988–1991, 1998.

[29] N.A. Pertsev and A.Y. Emelyanov. Domain–wall contribution to the piezoelectric response of epitaxial ferroelectric thin films. *Appl. Phys. Lett.*, 71:3646, 1997.

Chapter 2

Ferroelectrics and piezoelectrics

Abstract

In this chapter, the theory of ferroelectrics and piezoelectrics and PZT thin films is described, focussing on the concepts that are appropriate for this thesis. This includes the basic ferroelectric, piezoelectric properties, phase transitions and properties of PZT, the effect of substrate, clamping and strain and the phenomenological Landau - Ginzburg theory for epitaxial (001)-oriented single domain films and polydomain films.

2.1 Bulk ferroelectrics and piezoelectrics

Ferroelectricity is the phenomenon whereby a spontaneous polarization P_s occurs in a crystalline material, which can be reversed by an external electric field. Ferroelectricity occurs only in non-centrosymmetric crystal structures. A material is piezoelectric if a strain is created upon application of an electric field, or vice versa, an electric field is created as the material is strained. As is shown in fig. 2.1(a), all ferroelectrics are piezoelectric to a degree, but not all piezoelectrics are ferroelectric. If a material is piezoelectric but not ferroelectric, no spontaneous polarization is present and is induced by an electric field. Some of the highest piezoelectric coefficients occur in multicomponent inorganic oxides that are in the class of perovskites, for example $BaTiO_3$, $Pb(Zr,Ti)O_3$, $BiFeO_3$, $LiNbO_3$. Fig. 2.1(b) shows the perovskite unit-cell with ABC_3 crystal structure, where C is oxygen.

Despite the fact that ferroelectric materials do not contain iron, the name was derived from ferromagnetism due to some strong analogies in properties between

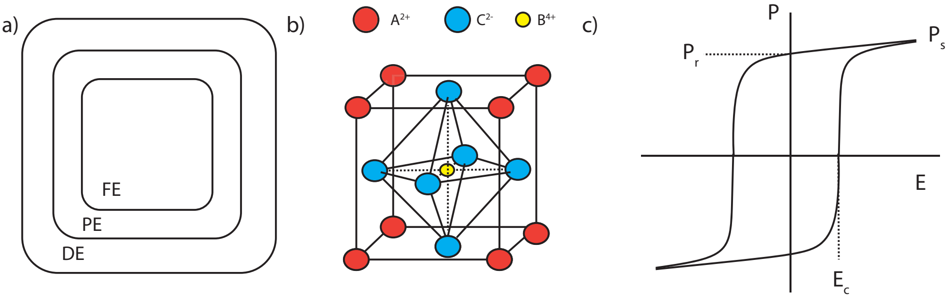

Figure 2.1: a) Classification of ferroelectric (FE), piezoelectric (PE) and dielectric (DE) materials, b) Image of a perovskite unit-cell with A, B and C-site ions, and c) a typical polarization hysteresis loop, with remanent polarization P_r, saturation polarization P_s and coercive field E_c.

both material classes. Firstly, spontaneous polarization occurs if a material is cooled below a transition temperature, the so-called Curie temperature T_C. Secondly, the temperature dependence of the dielectric permittivity ϵ follows a Curie-Weiss law, just as the magnetic permeability of ferromagnetic materials,

$$\frac{\epsilon}{\epsilon_0} = \frac{C}{T - T_0} \tag{2.1}$$

where ϵ_0 is the vacuum permittivity, T_0 the Curie-Weiss temperature, C a constant. Thirdly, different regions of the materials may be polarized in different directions, leading to ferroelectric domains. A balance between the depolarizing fields and ferroelectric space charge is pursued by reorienting domains to obtain energy minimization. Fourth a highly non-linear dielectric behavior occurs in the ferroelectric state. Hysteretic loops are observed for dielectric displacement $D = \epsilon E + P_s$ as a function of electric field E with spontaneous polarization P_S, similar to the dependence of the induction B on magnetic field strength H in ferromagnetic materials [1], see fig. 2.1(c).

Figure 2.2 shows the evolution of the free energy potential F as function of the order parameter polarization P for first and second order phase transitions as function of temperature. One can see that for the second-order phase transition (fig. 2.2(a)) the ferroelectric state has two minima corresponding to two ferroelectric polarization states at $P = P_0$. The polarization shows a gradual decrease toward T_0, and the dielectric constant ϵ_r is showing a peak at T_0, where the dielectric stiffness χ (=$\sim 1/\epsilon_r$) is zero, as shown in fig. 2.2(c)). The first-order ferroelectric state has three minima, two at finite positive and negative polarization values and one polarization value at P=0, see fig 2.2(d). The polarization decreases towards T_C and shows a sharp decrease at that temperature, see fig. 2.2(e). Fig. 2.2(f) illustrates that the dielectric stiffness χ is not zero at T_C.

What distinguishes ferroelectrics from ferromagnetics is the electromechanical coupling. Typically, the electromechanical coupling (or electrostrictive coupling) is much higher than magnetostrictive effects. It originates in the outstanding coupling of polarization with strain fields [3]. Fig. 2.1(a) shows the classification of

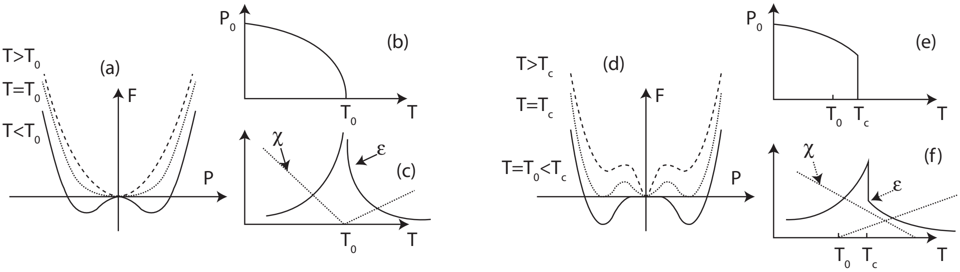

Figure 2.2: The second order phase transition (a), (b) (c), and the first order phase transition (d), (e) and (f), reproduced from ref. [2]

ferroelectrics, piezoelectrics and dielectric materials. Ferroelectrics are a subgroup of piezoelectrics and piezoelectrics are a subgroup of dielectrics. In a piezoelectric that is non-ferroelectric, a polarization is induced by an external electric field, causing a crystalline deformation. In a piezoelectric that is a ferroelectric, the polarization is spontaneous and can be changed by an electric field. On applying an electric field parallel to the spontaneous polarization P_s, it is augmented by an induced polarization P_{ind}, which adds an induced strain Δx to the lattice strain

$$x = x_s + \Delta x = Q(P_s + P_{ind})^2 = QP_s^2 + 2QP_sP_{ind} + QP_{ind}^2 \tag{2.2}$$

where Q is the electrostriction coefficient and x_s is the spontaneous strain [4]. The strain-electric field coupling is described by the linear part (second term) and the non-linear part (third term), and both are governed by the electrostrictive coefficient Q. This derivation holds for a tetragonal unit-cell, the polarization vector and applied electric field are directed in the same direction. An interesting insight emerges: piezoelectricity is electrostrictive behavior linearized by the spontaneous polarization [5]. For small fields the linear piezoelectric effect is found back. Using $P_{ind} = \epsilon_0\epsilon_r E$ and the approximation $\epsilon_r \sim \frac{dP}{dE}$, for small fields the induced strain Δx and piezoelectric constant d=$\Delta x/E$ are

$$\Delta x \sim 2QP_s\epsilon_0\epsilon_r E = dE \qquad\qquad d = 2\epsilon_0 QP_s\epsilon_r \tag{2.3}$$

An important example of ferroelectric materials in terms of applications is PZT, a solid solution of the ferroelectric $PbTiO_3$ and the anti-ferroelectric $PbZrO_3$. Lead ions are on the A-site, a titanium ion or zirconium ion on the B-site and oxygen ions form tetraeders, see fig. 2.3(b). At the Zr-rich side of the phase diagram, the lattice is rhombohedral, whereas it is tetragonal at the Ti-rich side. In the rhombohedral phase the polarization vector is along the body diagonal of the unit-cell, thus 8 possible domain states are possible. For the tetragonal phase the polarization is along the elongated direction. 6 possible domain states are possible, depending on the direction of the long axis. At high temperature the lattice is cubic centrosymmetric and non-ferroelectric.

The region where the rhombohedral phase transforms in the tetragonal phase is the morphotropic phase boundary (MPB) and is the region where the largest

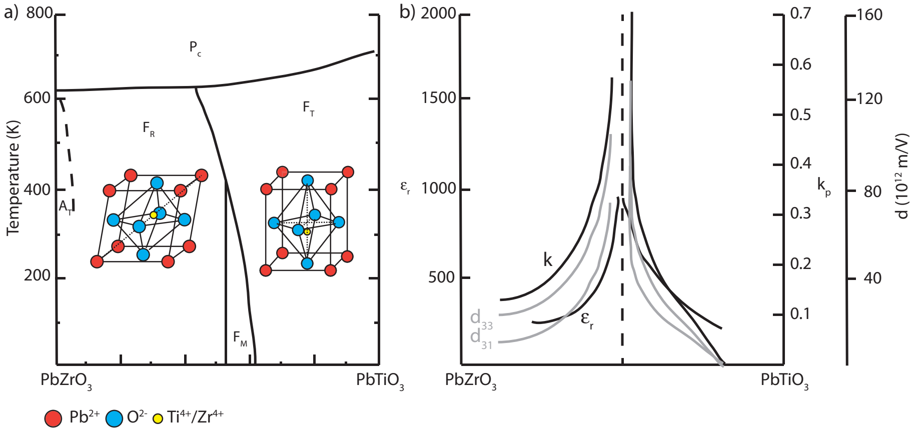

Figure 2.3: a) Phase diagram of PZT with the ferroelectric rhombohedral phase F_R, the ferroelectric tetragonal phase F_T, the paraelectric cubic phase P_C and a antiferroelectric orthorhombic phase A_T, and b) the effect of composition on the longitudinal piezoelectric coefficient d_{33}, the transferal piezoelectric coefficient d_{31}, the dielectric coefficient ϵ_r and the electromechanical coupling factor k_p in PZT ceramics at room temperature [7] [9]

piezoelectric properties have been found, see figure 2.3(b). The longitudinal piezoelectric coefficient d_{33}, the transversal piezoelectric coefficient d_{31}, the electromechanical coupling coefficient k and the dielectric coefficient ϵ_r are all showing a sharp increase towards this composition. The nearly vertical line indicating the MPB in the phase diagram shows that the MPB is practically independent of temperature and this is an important reason for the wide-spread application of PZT in devices, making device properties not sensitive to temperature change.

Piezoelectric materials such as PZT are often classified as 'hard' or 'soft'. A hard PZT is used to designate PZTs with the properties of a higher coercive field (E_c), lower losses for $E<E_c$, and lower weak-field susceptibilities [6]. PZT ceramics can be made hard or soft by addition of higher or lower valence substituents on either the A- or B-cations site [7].

As a final remark, it is noted that bulk PZT typically are fabricated as polycrystalline ceramics and that the growth of single-crystals of PZT was achieved only recently [8]. The method of growing from a single crystal from a melt is a process that is difficult to control. It shows a low growth speed and therefore resulting in relatively small crystals.

2.2 Thin films

2.2.1 Mechanical and crystalline effects of the substrate

Clamping of the thin film by a rigid substrate limits the in-plane deformation of the material. Moreover it imposes a deformation through epitaxial strain and

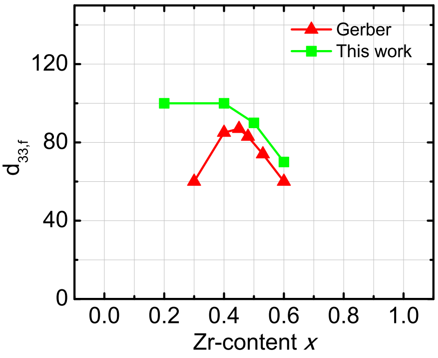

Figure 2.4: Piezoelectric coefficient $d_{33,f}$ at remanence (E = 0 V) for (001) oriented film, fabricated by chemical solution deposition (sol-gel) [10] (red) and this work fabricated by pulsed laser deposition on $SrTiO_3$ substrates (green).

through thermal strain after cooling from deposition temperature. Drastic effects on the functional properties of films may occur, due to changes in the crystallographic symmetry, phases, polarization states, functional properties, transition temperatures or phase transition order.

2.2.2 Effect of clamping on the piezoelectric effect

The clamping of a film on a substrate can be described, using the elastic properties in three dimensions [11]. No out-of-plane stress is present (X_3=0) since the film is free to move in this direction, and the in-plane stresses are assumed to be equal, $X_1 = X_2$. The in-plane strains x_1 and x_2 are zero, because of clamping to the substrate

$$\begin{aligned} x_1 = x_2 &= (s_{11}^E + s_{12}^E)X_1 + s_{13}^E X_3 = 0 \\ x_3 &= 2s_{12}^E X_1 + s_{11}^E X_3 \end{aligned} \tag{2.4}$$

where s_{ij} are the elastic compliances at constant electric field, X_i the stress, at constant electric-field and with respect to the cartesian coordinate system with the axes 1 and 2 in-plane and 3 out-of-plane.

The electric displacement D_3 in the film under an applied stress X_3 is

$$D_3 = d_{31}X_1 + d_{31}X_2 + d_{33}X_3 \tag{2.5}$$

where d_{ij} are the piezoelectric coefficients. Because of condition (2.4), this can be written as

$$D_3 = \left(d_{33} - 2d_{31}\frac{s_{13}^E}{s_{11}^E - s_{12}^E}\right)X_3 \tag{2.6}$$

using $d_{32} = d_{31}$ and $s_{13} = s_{12}$.

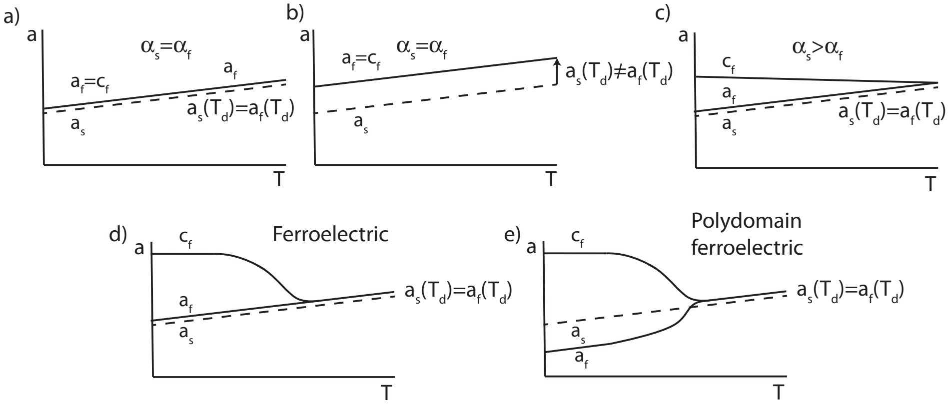

Figure 2.5: Lattice parameters evolution as function of temperature for the film a_f (in-plane) and c_f (out-of-plane) and the substrate a_s, for a) a film without epitaxial relaxation, thermal expansion differential with the substrate or ferroelectric transition, b) a film with epitaxial relaxation at deposition temperature, c) a film with a thermal expansion difference, and d) a film with a ferroelectric transition, and e) a film with ferroelectric transition and polydomain formation.

The effective piezoelectric coefficient for the film is thus given by

$$d_{33,f} = d_{33} - 2d_{31}\frac{s_{13}^E}{s_{11}^E - s_{12}^E} \tag{2.7}$$

The effective piezoelectric coefficients is typically smaller than the intrinsic piezoelectric coefficient, and often reduced by a factor 2 or more [12]. A number of measured piezoelectric coefficients of films are shown in fig. 2.4. The values are between 60 and 100 pm/V, significantly lower than on the unclamped ceramics, shown in fig. 2.3(b). Note that the sol-gel film shows the peak in $d_{33,f}$ around the MPB, whereas the epitaxial film this work shows saturation of d_{33} in the tetragonal phase.

2.2.3 Stress and strain

If a single domain film is clamped on a substrate, during cooling, the in-plane parameter of the film follows that of the substrate. If the strain is not relaxed by defect creation, the in-plane strain at temperature T with respect to the cubic phase at deposition temperature is

$$x = \Delta a / a_c = \alpha_s \Delta T \tag{2.8}$$

with Δa the in-plane change in lattice parameter, a_c the lattice parameter at deposition temperature T_d, α_s the thermal expansion coefficient of the substrate and ΔT the temperature difference with respect to the cubic phase at deposition temperature T_d.

Fig. 2.5 shows several effects in the films using the lattice parameter temperature evolution. If a films is grown at T_d and cooled to room temperature, various trends can be identified by measuring the lattice parameter evolution. For a cubic epitaxial film with equal thermal expansion coefficient of the film α_f and the substrate α_s, the lattice parameters show the trend as illustrated in 2.5(a). If the lattice parameter of the film and substrate are not equal, misfit dislocations will occur during growth of a relatively thick film ($>$ 100 nm), to relax the stress at deposition temperature, see fig. 2.5(b). If a cubic material has a smaller (larger) thermal expansion coefficient than the substrate, the in-plane clamping of the substrate will elongate (shorten) the out-of-plane lattice parameter c_f, see fig. 2.5(c). In a ferroelectric material, a spontaneous transition from cubic into for example a tetragonal material occurs for which c_f to differs from a_f, see fig. 2.5(d). Therefore a polydomain film will typically form in order to lower the generated stress, see chapter 4. These domains are twin-related and consist of tetragonal cells lying in-plane and out-of-plane. The resulting typical lattice parameter evolution is shown in fig. 2.5(e): here a_f is not equal to a_s. In real-world PZT thin films, all described effects play a role and will be studied in the coming chapters.

The polydomain formation can be explained using the lattice parameters of bulk PZT as function of temperature as shown in fig. 2.6 [13]. The expansion of the PZT due to the paraelecric-ferroelectric phase transition can be extracted from the spontaneous deformation Δa_1 and Δa_3 of the short and the long unit-cell axis of bulk PZT. The resulting expansion can be quantified using a quasi-thermal expansion coefficient α_f of the PZT film, that uses the contraction or expansion that is linearized between deposition temperature and room temperature. The obtained values for α_f are much higher than that of a typical substrate, both shown in fig. 2.6(b). $Pb(Zr_{0.2},Ti_{0.8})O_3$ shows $\alpha = -61 \cdot 10^{-6}$ K^{-1} in the a_3 direction and $\alpha = 28 \cdot 10^{-6}$ K^{-1} in the a_1 direction, whereas the substrates all have α_s between $2.8 \cdot 10^{-6}$ K^{-1} and $11.0 \cdot 10^{-6}$ K^{-1}. This effect is present for $Pb(Zr_{0.52},Ti_{0.48})O_3$ to a lesser extent. During cooling down from the deposition temperature (600 °), the difference in thermal contraction of the film and substrate generate a large stress. Ferroelectric domains form to relax this stress. The quasi-thermal expansion coefficient of the short axis a_1 and of the long axis a_3 have opposite sign and the domain fraction of the in-plane and out-of-plane oriented domains results in the match of the temperature dependent strain of the film to the rigid substrate. The domain fraction is adjusted relax the stress in the film.

Since the film is clamped by the substrate, the induced strain causes stress X in the film. Fig. 2.7 shows the effect of stress in a film that is deposited on a 4 inch silicon wafer. The curvature of the wafer is generated by the differential thermal expansion coefficients of the substrate α_s and the film α_f. The Stoney equation describes the linear relationship between wafer bending and film stress X [14]

$$X = \frac{E_s t_s}{6(1 - \upsilon_s) t_f} R \tag{2.9}$$

where E_s is Young's modulus of the substrate, υ_s Poisson ratio of substrate, t_s and t_f are the substrate and film thickness respectively and R is the film curvature.

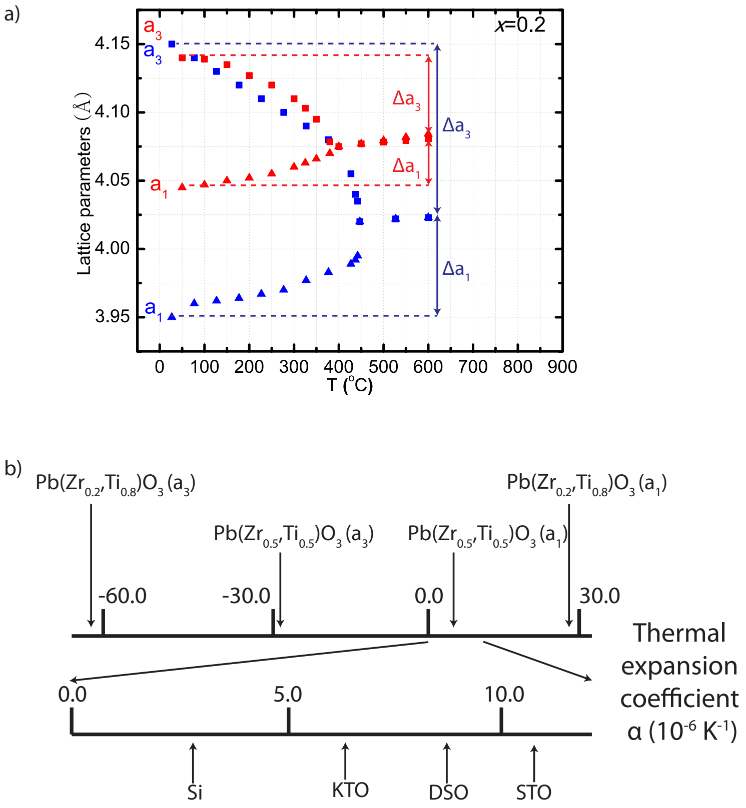

Figure 2.6: a) The lattice parameters evolution of bulk PZT of $x = 0.2$ (blue) and $x = 0.52$ (red), and b) the thermal expansion coefficients of the tetragonal long axis a_3 and short axis a_1, and several substrates

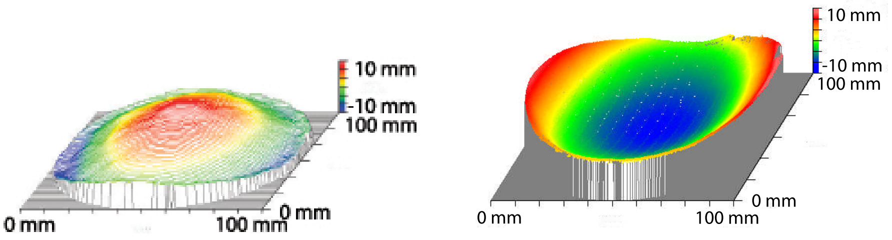

(a) (b)

Figure 2.7: Wafer curvature measured by white-light interferometry a) bare wafer, b) a 500 nm thick PZT films with $x = 0.52$ was deposited on a 4-inch platinized silicon wafer (Pt/Ti/SiO_2/Si), using a large area pulsed laser deposition system (Solmates BV). The bare wafer is convex due polishing, the wafer with film is concave to tensile residual thermal strain.

Using radius R of 76.7 m, which is corrected for the initial convex curvature, results in a film stress of 196.2 MPa. Assuming the stress is not generated by grain boundaries or misfit dislocations [15], the generated stress is predicted using the thermal expansion difference in the film and temperature difference, using $X = E_f x_1 = E_f(\alpha_f - \alpha_s)\Delta T$ and strain of the PZT film is x_1 of $1.61{\cdot}10^{-3}$. The reported Young's moduli E_f range between 25 and 260 GPa. Here a value of 83 GPa was used [16]. The generated stress is tensile with a value of 134 MPa. It can be concluded that a significant stress arises that is most likely originates from the difference in thermal expansion coefficient of the the film and the substrate.

2.2.4 Phenomenology

The Landau-Devonshire (LD) phenomenological theory is a powerful theory to describe the properties of ferroelectric materials [17] [18] [19] [20]. It incorporates non-linear effects and cross-coupling between the electrical, mechanical and electromechanical domain. This model uses the symmetrical Gibbs free energy as a power expansion with respect to the polarization P as order parameter. For PZT, the Gibbs potential is expressed in a power series up to the sixth. For simplicity a (one dimensional) analysis is considered for a tetragonal crystal

$$G = aP^2 + bP^4 + cP^6 - EP \tag{2.10}$$

Here a, b, c are constants. The first three terms represent the crystal polarization energy. It is a double-well with minima for $P = \pm P_s$, the spontaneous polarization. The EP term represents the electric field energy in case of an applied field. This term described the tilting of the ferroelectric double-well causing switching of the polarization to the opposite potential well. If $b > 0$, a second-order phase transition occurs at $T = T_c$, and free energy will evolve continuously as a function of decreasing temperature. If $b < 0$, a first-order phase transition occurs. Here, no depolarization energy is included in the free energy, since the films have conducting electrodes.

Strain can be described by the change of crystallographic dimensions. Typically, misfit strain S_m values for a (001) oriented single crystalline film can be calculated following

$$S_m = \frac{a - a_0}{a_0} \tag{2.11}$$

where a is the in-plane lattice constant and a_0 the cubic reference lattice constant. This cubic reference lattice constant is calculated by a volume conservation argument through $a_0 = (a^2 \cdot c)^{\frac{1}{3}}$, where a is the in-plane lattice parameter and c the out-of-plane lattice parameter, assuming in-plane equal lattice parameters [2].

The influence that the substrate has on the properties of ferroelectric materials should be added to the model. The polarization is coupled to the strain (eq. 2.2). The Gibbs potential is to be determined as function of stress X_{ij} and strain x_{ij} in a Cartesian coordinate system and using the Voigt matrix notation. The stresses X_3=X_4=X_5=0, and strains x_1=x_2=S_m and x_6=0. The Gibbs energy for a clamped film is the obtained as

$$G_f = \frac{S_m^2}{s_{11}+s_{12}} + a^*P^2 + b^*P^4 + cP^6 - EP \tag{2.12}$$

where

$$a^* = a - \frac{2S_mQ_{12}}{s_{11}+s_{12}} \tag{2.13}$$

$$b^* = b + \frac{Q_{12}^2}{s_{11}+s_{12}} \tag{2.14}$$

so that the quadratic and quartic terms in the Gibbs free energy are changed. Here s_{ij} is the elastic constants and Q_{ij} are the electrostrictive constants. Note that even for an unstrained film $G \neq G_f$, since $b \neq b^*$.

Figure 2.8 shows the ferroelectric double-well potential for bulk and thin-films at several misfit-strain values of PZT $x = 0.52$. The spontaneous polarization P_s is easily obtained from the minimization of $g(P)$. Remanent polarization is related to the position of the minimum of the well ($\partial G/\partial P = 0$), whereas the dielectric constant is equal to the slope of the well at the minimum ($\partial^2 G/\partial^2 P$). The shape of the polarization loop can be derived from the potential graph. The remanent polarization is typically lower in the film than in the bulk. Also it can be seen that the remanent polarization and the dielectric constant decrease as function of S_m. The coercive field is related to the height of the potential barrier at P=0. A peculiar result is that the measured coercive field in ferroelectric is 1 order or magnitude lower than the coercive field that follows from the phenomenology. In literature this Landau paradox has been unresolved [21] [22].

In many ferroelectrics, the strain-driven effects can be large. Next to the equilibrium value of the order parameters, all dielectric, elastic and piezoelectric coefficients follow from eq. 2.12. For tetragonal (001) oriented clamped thin films [18] [23], the dielectric constant is

$$\epsilon_r = 1/2\epsilon_0^2(a^* + 6b^*P^2 + 15cP^4) \tag{2.15}$$

and the piezoelectric constant is

$$d_{33} = Q_{11}P/(a^* + 6b^*P^2 + 15cP^4) \tag{2.16}$$

The change of the thermodynamic constants, as showed in eq. (2.13) and (2.14), has major implications for the properties of the thin film. Fig. 2.9 shows the (a) P-E, (b) ϵ_r-E and (c) d_{33}-E loops calculated from the single domain LD model for strained PZT with $x = 0.5$ and for bulk. The spontaneous polarization, permittivity, coercive fields depend significantly on the misfit strain S_m. For example, the transition temperature may be shifted by tens of degrees from the bulk value (T_0)

$$T^* = T_0 + \frac{4S_mQ_{12}}{a(s_{11}+s_{12})} \tag{2.17}$$

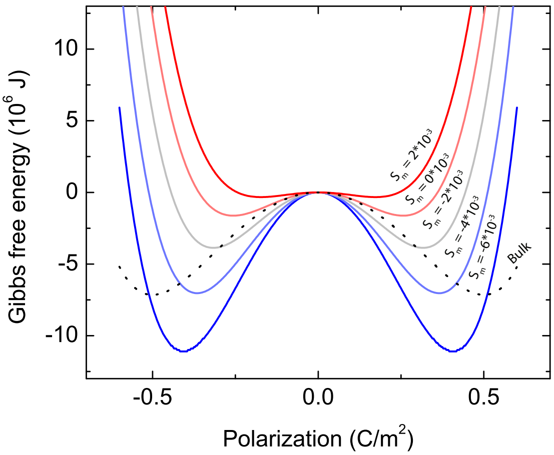

Figure 2.8: Ferroelectric double-well potential for bulk and thin-films at several misfit-strain values of Pb(Zr$_x$,Ti$_{1-x}$)O$_3$ with $x = 0.5$.

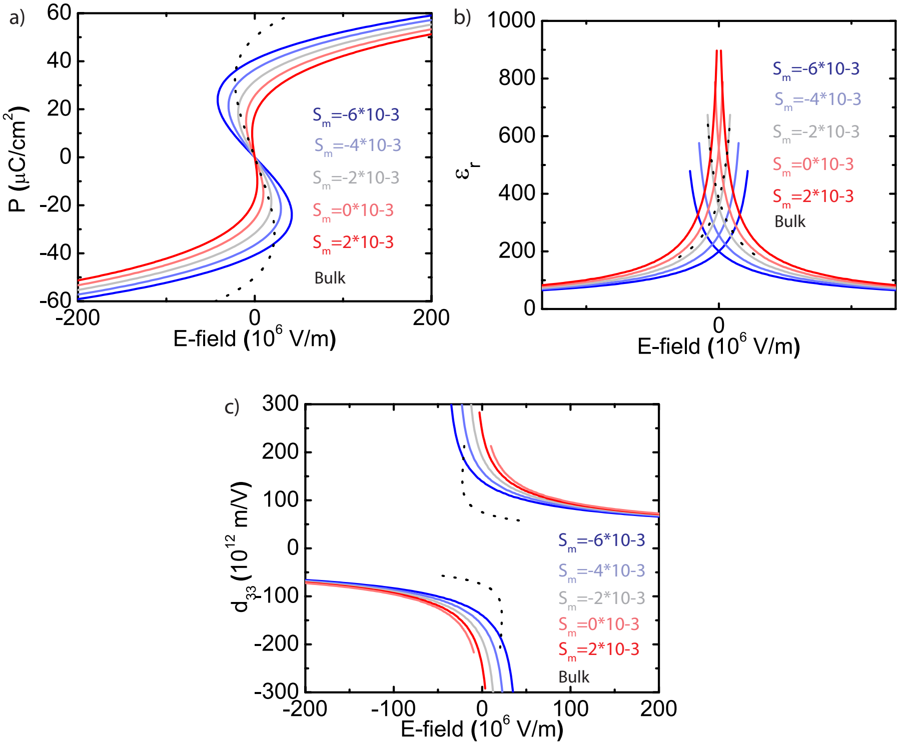

Figure 2.9: a) P-E, b) ϵ_r-E and c) d_{33}-E loops calculated from the single domain LD model for Pb(Zr$_x$,Ti$_{1-x}$)O$_3$ with $x = 0.5$.

Note that such misfit epitaxial strain can change the nature of the transition from first to second order (if $b < 0$ and $b^* > 0$). Hereafter, it will be shown that the LD theory needs to be applied in 3 dimensions to describe the application of a biaxial in-plane strain and a polarization that can have components in the in-plane and out-of-plane directions.

2.2.5 Models for thin films

The Landau-Ginsburg (LD) phenomenological theory, as presented in 2.2.4, can be used to describe the crystallographic phase and properties of $\mathrm{Pb(Zr}_x\mathrm{,Ti}_{1-x}\mathrm{)O}_3$ as a function of composition, misfit strain and temperature. The model was developed in three-dimensions, for single-domain films by Pertsev [18]. PZT films with a thickness larger than 100 nm, typically are polydomain as a consequence of stress relaxation. This introduces a complication to the model, which is described by Kukhar *et al.* [24]. Alternative approaches to modelling of ferroelectric films, are phase-field modeling [25] or density-funcional theory [26], however phenomenological theory is superior in simplicity.

Single domain model

An important concept in the LD-theory is the *misfit strain - composition diagram* as shown in fig. 2.10(a). All crystallographic phases and boundaries between the phases are schematically presented. The temperature dependence of the phase boundaries are shown in fig. 2.10(b) for Zr-content $x = 0.4$. The single domain model consists of the tetragonal c-phase ($P_1 = P_2 = 0, P_3 \neq 0$), the orthorhombic aa-phase ($P_1 = P_2 \neq 0, P_3 = 0$) and the monoclinic r-phase ($P_1 = P_2 \neq P_3$). The polarization components depend on the misfit strain, as can be seen in fig. 2.10(c). The most interesting result is the observation of the r-phase, for compositions from PbTiO_3 to $\mathrm{Pb(Zr}_x\mathrm{,Ti}_{1-x}\mathrm{)O}_3$ with $x = 0.6$. This r-phase is characterized by a polarization vector that is not directed along either the (001), (100) or (010) direction but can have any intermediate direction in the (110)-plane as function of misfit strain. Large piezoelectric coefficients in bulk PZT near the morphotropic phase boundary are related to such a rotation of the polarization vector [27] and therefore similar properties in thin films might be obtained. The predicted anomalies in the dielectric and piezoelectric properties at the boundary between the r-phase and aa-phase, are interesting for possible strain engineering of the properties, see fig. 2.10(d) and (e).

Polydomain model

The polydomain model [24] analyzes the overall free energy according to domain fraction and microscopic boundary conditions of strain and electric field at the domain-walls. This model studies the rotational instabilities of the polarization and predicts movement of the boundaries between tetragonal, monoclinic, rhombohedral, orthorhombic crystalline phases. Fig. 2.11 shows the constructed room

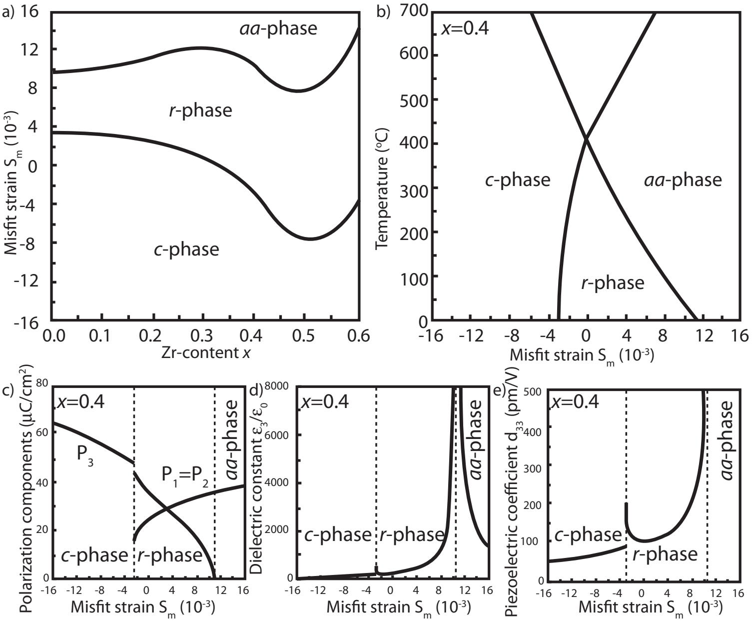

Figure 2.10: The single domain LD model at room temperature for PZT with $x = 0.4$, with the a) misfit strain - composition phase diagram, b) misfit strain - temperature diagram, c) polarization components P_1, P_2 and P_3 as function of misfit strain, d) dielectric constant ϵ_r as function of misfit strain and e) piezoelectric constant $d_{33,f}$as function of misfit strain

temperature misfit strain - composition diagram for polydomain PZT thin films, using data of ref. [24]. Here the r-phase that exists over a wide compositional range in the single domain model has disappeared and is replaced by the tetragonal c/a and rhombohedral r/r polydomain phases. The polydomain phases consist of the tetragonal c/a-phase, monoclinic r_1/r_2-phase, the tetragonal a_1/a_2-phase and the single domain tetragonal c-phase. These phases consists of combinations the domains r_1 ($P_1 \neq P_2 \neq P_3 \neq 0$), r_2 ($P_1 \neq P_2 \neq P_3 \neq 0$), c ($P_1 = P_2 = 0, P_3 \neq 0$), a_1 ($P_2 = P_3 = 0, P_1 \neq 0$) and a_2 ($P_1 = P_3 = 0, P_2 \neq 0$). The gray planed in 2.11 are the domain-wall, that are in the (101)-plane for the c/a-phsae, the (110)-plane for the a_1/a_2-phase and the (010)-plane for the r_1/r_2-phase.

New polarization states that are not possible in bulk are predicted, and anomalies for certain strain values may boost the properties. It results in several heterophases $ca^*/aa^*/ca^*/aa^*$, $aa_1/aa_2/aa_1/aa_2$ in which the polarization is not along the tetragonal easy axis [24]. The model shows that next to intrinsic properties, domain-wall displacement determines an important part of the predicted properties. Especially in the r_1/r_2-phase, this domain-wall contribution to the properties is high. The phase boundary between c/a-phase and r_1/r_2-phase is associated with a low domain-wall energy and the single domain r-phase is suited to describe the properties in this region, as will be shown in ch. 6. Therefore, this phase is added to the misfit strain - composition phase diagram in fig. 2.11.

In order to test the validity of the phenomenological models, these should be verified experimentally. In literature, a small number of reports can be linked to effects that are predicted by these models. For example, indications of the rotational r-phase phase were observed in BTO under large epitaxial tensile strain [28] and the single domain c-phase was observed in ultra-thin PZT films [29]. The biaxially substrate-induced strain induces a shift of the tetragonal and rhombohedral phase [30]. The polydomain tetragonal c/a-phase has been extensively studied [31–33], but mainly on very thin films ($<$ 100 nm). In this work, a systematic experimental analysis of the crystallography and functional properties is presented. The agreement of experiments and the model are evaluated. The existence of the r-phase is studied. The tensile strain of the silicon is used to study the properties near the anomaly of dielectric coefficient at the phase boundary between the aa-phase (single domain) or a_1/a_2 boundary (polydomain) and adjacent phases. The properties near the phase boundary between the tetragonal phase (c and c/a-phase) and the rhombohedral or monoclinic phase (r-phase or r/r-phase) is studied.

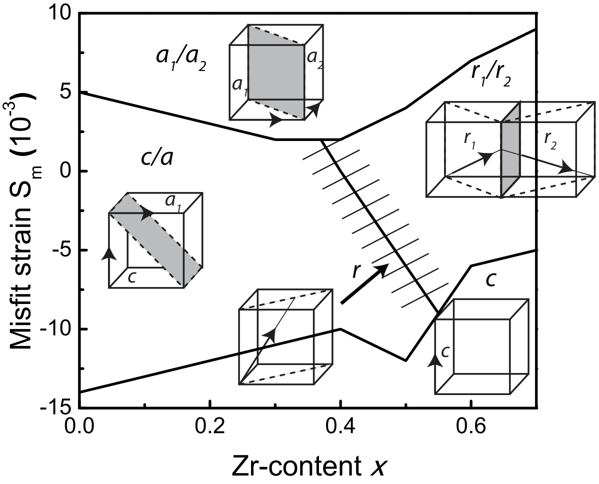

Figure 2.11: Misfit strain - composition phase diagram with polydomain polarization states at room temperature, for (001) thick (> 100 nm) PZT films.

2.3 References

[1] K. Lubitz W. Wersing, W. Heywang. *Piezoelectricity.* Springer, 2008.

[2] P. Chandra. *Physics of Ferroelectrics*, chapter 4: A Landau Primer, pages 1–47. Springer, Jul 2007.

[3] L.E. Cross. Ferroelectric materials for electromechanical transducer applications. *Mat. Chem. Phys.*, 43(2):108–115, 1996.

[4] A.J. Bell. Factors influencing the piezoelectric behaviour of PZT and other morphotropic phase boundary ferroelectrics. *J. Mater. Sci.*, 41(1):13–25, 2006.

[5] R.E. Newnham, V. Sundar, R. Yimnirun, J. Su, and Q.M. Zhang. Electrostriction: nonlinear electromechanical coupling in solid dielectrics. *J. Phys. Chem. B.*, 101(48):10141–10150, 1997.

[6] D. Viehland. Effect of uniaxial stress upon the electromechanical properties of various piezoelectric ceramics and single crystals. *J. Am. Ceram. Soc.*, 89(3):775–785, 2006.

[7] B. Jaffe, W. Cook, and H. Jaffe. *Piezoelectric Ceramics.* Academic Press, London, ferroelectric behaviours dominated by mobile and randomly quenched impurities in modified quenched lead zirconate titante ceramics edition, 1971.

[8] S.E. Park and T.R. Shrout. Ultrahigh strain and piezoelectric behavior in relaxor based ferroelectric single crystals. *J. Appl. Phys.*, 82:1804, 1997.

[9] B. Jaffe, R.S. Roth, and S. Marzullo. Piezoelectric properties of lead zirconate–lead titanate solid–solution ceramics. *J. Appl. Phys.*, 25:809, 1954.

[10] P. Gerber, U. Böttger, and R. Waser. Composition influences on the electrical and electromechanical properties of lead zirconate titanate thin films. *J. Appl. Phys.*, 100:124105, 2006.

[11] K. Lefki and G.J.M. Dormans. Measurement of piezoelectric coefficients of ferroelectric thin films. *J. Appl. Phys.*, 76:1764, 1994.

[12] K. Prume, P. Muralt, T. Schmitz-Kempen, and S. Tiedke. Tensile and compressive stress dependency of the transverse $e_{31,f}$ piezoelectric coefficient of pzt thin films for mems devices. *Proceedings of SPIE*, 2007.

[13] B. Noheda, D.E. Cox, G. Shirane, J.A. Gonzalo, L.E. Cross, and S.E. Park. A monoclinic ferroelectric phase in the $Pb(Zr, Ti)O_3$ solid solution. *Appl. Phys. Lett.*, 74:2059, 1999.

[14] M. Ohring. *Materials science of thin films.* Academic Press, London, 2 edition, 2002.

[15] D. Balzar, P.A. Ramakrishnan, and A.M. Hermann. Defect–related lattice strain and the transition temperature in ferroelectric thin films. *Phys. Rev. B.*, 70(9):092103, 2004.

[16] H. Nazeer, L. Abelmann, N.R. Tas, J.W. van Honschoten, M.H. Siekman, and M.C. Elwenspoek. Determination of young's modulus of pzt and $Co_{80}Ni_{20}$ thin films by means of micromachined cantilevers. 2009.

[17] M.J. Haun, E. Furman, S.J. Jang, and L.E. Cross. Thermodynamic theory of the lead zirconate–titanate solid solution system – part 1: Phenomenology. *Ferroelectrics*, 99:13–25, 1989.

[18] N.A. Pertsev, V.G. Kukhar, H. Kohlstedt, and R. Waser. Phase diagrams and physical properties of single-domain epitaxial $Pb(Zr_{1-x}, Ti_x)O_3$ thin films. *Phys. Rev. B.*, 67(5):054107, 2003.

[19] A.F. Devonshire. Theory of barium titanate – part 1. *Philos. mag.*, pages 1–25, Dec 2010.

[20] A.F. Devonshire. Theory of barium titanate – part 2. *Philos. mag.*, pages 1–16, Dec 2010.

[21] R Landauer. Electrostatic considerations in batio3 domain formation during polarization reversal. *Journal of Applied Physics*, 28(2):227–234, 1957.

[22] S Ducharme, V.M Fridkin, A.V Bune, S.P Palto, and L.M Blinov. Intrinsic ferroelectric coercive field. *Phys. Rev. Lett.*, 84(1):175—178, 2000.

[23] M.J. Haun, E. Furman, S.J. Jang, and L.E. Cross. Modeling of the electrostrictive, dielectric, and piezoelectric properties of ceramic $PbTiO_3$. *IEEE Trans. Ultrasonics, Ferroelectrics and Frequency Control*, 36(4):393–401, 2002.

[24] V.G. Kukhar, N.A. Pertsev, H. Kohlstedt, and R. Waser. Polarization states of polydomain epitaxial $Pb(Zr_{1-x}, Ti_x)O_3$ thin films and their dielectric properties. *Phys. Rev. B.*, 73(21):214103, 2006.

[25] Q.Y. Qiu, R. Mahjoub, S.P. Alpay, and B.K. Nagarajan. Misfit strain–film thickness phase diagrams and related electromechanical properties of epitaxial ultra–thin lead zirconate titanate films. *Acta Mater.*, 58(3):823–835, 2010.

[26] H.J. Lee, S.M. Nakhmanson, M.F. Chisholm, H.M. Christen, K.M. Rabe, and D. Vanderbilt. Suppressed dependence of polarization on epitaxial strain in highly polar ferroelectrics. *Phys. Rev. Lett.*, 98(21):217602, 2007.

[27] D. Damjanovic. A morphotropic phase boundary system based on polarization rotation and polarization extension. *Appl. Phys. Lett.*, 97:062906, 2010.

[28] I.B. Misirlioglu, S.P. Alpay, F. He, and B.O. Wells. Stress induced monoclinic phase in epitaxial $BaTiO_3$ on MgO. *J. Appl. Phys.*, 99(10):104103, Jan 2006.

[29] N.A. Pertsev and H. Kohlstedt. Elastic stabilization of a single–domain ferroelectric state in nanoscale capacitors and tunnel junctions. *Phys. Rev. Lett.*, 98(25):257603, 2007.

[30] K. Lee and S. Baik. Morphotropic phase boundary in epitaxial $Pb(Zr, Ti)O_3$ thin films: Two-dimensional planar size effect. *Appl. Phys. Lett*, 86:202901, 2005.

[31] B.S. Kwak, A. Erbil, B.J. Wilkens, J.D. Budai, M.F. Chisholm, and L.A. Boatner. Strain relaxation by domain formation in epitaxial ferroelectric thin films. *Phys. Rev. Lett.*, 68(25):3733–3736, 1992.

[32] A.H.G. Vlooswijk, B. Noheda, G. Catalan, A. Janssens, B. Barcones, G.J.H.M. Rijnders, D.H.A. Blank, S. Venkatesan, B. Kooi, and J.T.M. De Hosson. Smallest 90 domains in epitaxial ferroelectric films. *Appl. Phys. Lett.*, 91:112901, 2007.

[33] S. Venkatesan, B.J. Kooi, J.T.M. De Hosson, A.H.G. Vlooswijk, and B. Noheda. Substrate influence on the shape of domains in epitaxial $PbTiO_3$ thin films. *J. Appl. Phys.*, 102:104105, 2007.

Chapter 3

Fabrication and characterization of epitaxial PZT heterostructures

Abstract

This chapter presents the fabrication and properties of epitaxial PZT heterostructures on silicon substrates. First the general methods for fabrication and characterization are described. Special attention is directed at x-ray diffraction and reciprocal space mapping. An explanation of the growth of the epitaxial buffer layers using CeO_2 and YSZ on silicon is provided. A procedure to switch the crystal orientation on these buffer layers from (110) to (001) by a single process step is described and the effect on the ferroelectric properties. Finally, the crystal quality of (001)-oriented PZT films on four PZT heterostructure geometries is compared and the STO buffered silicon is found to be the preferred template for the study of the intrinsic properties of PZT on silicon.

3.1 Introduction

The promising applications of PiezoMEMS such as inkjet printheads, piezoelectric micromachined ultrasound transducers and energy harvesters have raised interest in the integration of PZT thin films on silicon substrates. Progress on the development of large area pulsed laser deposition is diminishing the cost per device and at the same time providing excellent functional properties. The use of silicon as substrate in comparison to the single crystal substrate may change the structural symmetry, polarization, dielectric constant and piezoelectric coefficients. Better understanding of the effect of the substrate on the crystallographic and functional properties of PZT thin films fabricated on silicon is needed for the design of functional devices.

High-quality epitaxial heterostructures are necessary to draw conclusions about the intrinsic properties without mixed orientations or high defect densities. A PZT heterostructure is a multilayer of PZT that is sandwiched between electrodes. The PZT heterostructures are typically grown on single-crystal substrates strontium titanate ($SrTiO_3$, STO), dysprosium scandate ($DyScO_3$, DSO) or potassium tantalate ($KTaO_3$, KTO). The electrodes are made of oxide materials, such as strontium ruthenate ($SrRuO_3$), lanthanum nickelate ($LaNiO_3$), lanthanum strontium manganate ($La(Sr,Mn)O_3$) or indium tin oxide ($(In,Sn)O_3$) [1]. Next to the epitaxial growth of the electrodes, these oxide electrodes have shown an improvement of the long term stability of these functional piezoelectric heterostructures, owing to a diminished charge accumulation at the electrode-film interface.

In recent years, efforts to obtain similar PZT heterostructures on silicon have resulted in several buffer layer systems on silicon. This is needed since many films are chemically incompatible with silicon. A buffer layer of yttria-stabilized-zirconia ($(Y_2O_3)_{0.08},(ZrO_2)_{0.92}$), YSZ) on silicon is able to transfer the crystallographic properties of silicon to subsequently deposited layers [2]. This buffer layer has a significant mismatch with silicon. The integration of STO directly on silicon has been triggered by the observation of a low mismatch with silicon, promising a low amount of misfit dislocation. This STO buffer layer has been achieved with a quality that is comparable to that of single-crystal STO, using deposition by Molecular Beam Epitaxy [3]. It is interesting to explore the advantages and disadvantages of use of these epitaxial buffer layers for the functional PZT devices in terms of fabrication and properties. It is desirable to gain knowledge whether films on silicon match the crystal quality of the single-crystal substrates, in that way allowing fundamental studies.

The aim of this chapter is to describe several aspects of fabrication and properties of epitaxial PZT heterostructures on silicon. The first part of the chapter is dedicated to the general thin-film fabrication and characterization. The heteroepitaxy of used materials will be described in sec. 3.2, followed by the fabrication by Pulsed Laser Deposition (PLD) and patterning in sec. 3.3. The characterization of crystal structure by X-ray Diffraction is described in sec. 3.4.1. Microstructural properties and surface morphology are presented in sec. 3.4.2 and the ferroelectric, dielectric and piezoelectric properties are given in sec. 3.4.3. In the second part, the focus is on the properties of PZT films on CeO_2-YSZ-buffered silicon substrates. In sec. 3.5, the growth of buffer layers on silicon using YSZ and STO is presented. Subsequently, the control of the crystal orientation on this template by a single process step is described in sec. 3.6. Finally, the different available substrate - buffer layer systems and the properties are studied and compared to the fiber-textured films on platinized silicon wafers that are used in typical applications, and the single-crystal perovskite substrates such as $SrTiO_3$ (STO), in sec. 3.7.

Table 3.1: Table of lattice parameters a and length of the face-diagonal a_{fd}=$a/\sqrt{2}$

Material	a (Å)	a_{fd} (Å)
Si	5.43	3.84
YSZ	5.14	3.63
CeO_2	5.41	3.83
$SrRuO_3$	3.93	
$KTaO_3$	3.99	
$DyScO_3$	3.95	
$SrTiO_3$	3.905	
$Pb(Zr_{0.2},Ti_{0.8})O_3$	3.94	
$Pb(Zr_{0.4},Ti_{0.6})O_3$	3.98	
$Pb(Zr_{0.52},Ti_{0.48})O_3$	4.00	

3.2 Epitaxial PZT heterostructures

This section describes the epitaxial buffer layers on silicon and the PZT heterostructures used in this thesis. The phenomenon of a single-crystal film that is coherently oriented on a single crystal substrate is known as epitaxy. In order to fabricate epitaxial films, a good lattice match of the film with the underlying film or substrate is required [4]. Materials with a perovskite structure are well suited for epitaxial growth, owing to their similar crystal structure and unit cell dimensions. The bulk lattice parameters are in the range of 3.85 Å- 4.2 Å, as shown in table 3.1. PZT and SRO can be grown cube-on-cube with respect to the substrates KTO, DSO and STO. The in-plane lattice parameter of PZT depends on the composition and ranges from 3.94 Åfor $Pb(Zr_{0.2},Ti_{0.8})O_3$ to 4.00 Åfor $Pb(Zr_{0.52},Ti_{0.48})O_3$ [5, 6].

If oxide materials are grown on silicon, the match of the lattice parameter and the chemical reactivity is not suitable to obtain an epitaxial film. Buffer layers are used that are chemically stable and have a lattice parameter with a sufficiently low mismatch with silicon and the oxide materials. STO and YSZ are suitable as epitaxial buffer layers. In order to obtain a (001) oriented perovskite ($a \sim 4$ Å) on silicon ($a = 5.41$ Å, the half face-diagonal a_{fd}=$a/\sqrt{2}$=3.83 Å) the crystal needs to be 45 ° rotated in-plane. In this way, the length of the in-plane face-diagonal $a/\sqrt{2}$ fits to the unit-cell length of the perovskite. The growth of a buffer layer system, such as YSZ/Si, results in an epitaxial (110) oriented film. A detailed explanation of the epitaxial buffer layers in contact with silicon will be given in sec. 3.5. A procedure to switch the crystal orientation of the epitaxial layers on the YSZ buffered silicon is described in sec. 3.6. The STO-buffer layer is fabricated by Molecular Beam Epitaxy [7]. A comparison of the crystallographic properties of the different heterostructures is presented in sec. 3.7.

3.3 Thin film fabrication

3.3.1 Pulsed Laser Deposition

Pulsed Laser Deposition (PLD) is a thin film growth technique in which a target material is heated up locally by a short focused laser pulse. A plasma plume forms and expands until it reaches the substrate. This technique is particularly well-equipped for the growth of complex oxides [8]. The ability to control deposition pressure, substrate temperature and flux rate of the deposited species independently, allows the tuning of the growth conditions to obtain high-quality films. The ratio of elements may be tuned accurately in the source material sintered pellet of oxide powders, in view of the desired composition. The ratio of elements in the target is maintained during the deposition process in most cases.

A pulsed KrF excimer laser with a wavelength of 248 nm is used, with a typical pulse duration of 20-30 ns. A lens is used to focus the laser pulse on the target material. The laser beam is shaped using a rectangular mask of 4 mm by 2 mm. Before deposition, the target is grinded to remove coarse roughness of the target surface, and pre-ablated for 1 minute to remove contaminants on the surface. The substrate is attached to a heater and placed inside a vacuum system. The target is placed in front of the substrate, and the laser pulse is coming in at an angle of 45° with the target. Typically, a laser intensity at the target (fluence) of 2.5 J/m^2 and a spot size of 3 mm^2 is used. Attenuation of the laser at the window is 8-20 %. At these deposition parameters, the deposition rate is approximately 0.028 nm per pulse and about 1 μm per hour at a laser pulse repetition rate of 10 Hz. For all experiments described in this thesis the following materials and settings are used. The 100 nm $SrRuO_3$ (SRO) is deposited on the substrate or buffer layer in 0.13 mbar O_2. The target - substrate distance is 51 mm. The 1 μm PZT film is deposited in 0.1 mbar O_2 at a target - substrate distance of 54 mm. After deposition, cooling was done at a rate of 10°C/minute, in O_2 at 1 atmosphere. The growth temperature for both materials is 600°C. The deposition of the YSZ and CeO_2 buffer layers on silicon use a fluence of 2.5 J/m^2, a spot size of 3 mm^2, a repetition rate of 7 Hz and a background gas pressure of 0.02 mbar O_2. The first 30 seconds of YSZ on Si are deposited in Ar instead of O_2, which will be described in detail in sec. 3.5. Platinum top electrodes are deposited at room temperature in a 0.01 mbar Argon gas pressure. In that case the laser fluency is 5.0 J/cm^2 and the spot size is 1.5 mm^2.

3.3.2 Patterning

In order to fabricate device structures with electrodes in a parallel plate geometry, the films can be patterned using three processes: 1) wet and dry-etching, 2) lift-off or 3) shadow-mask deposition.

In the first two cases, standard photolithography is used to define a photoresist layer. Typically, the definition of the photoresist edges limits the resolution of the used photolithography to 5 - 10 μm. To reduce the influence of edgeinhomogeneities, the used device geometries are larger than 50 x 50 μm^2. To diminish the chance of accidental electrical shortcuts between the electrodes due to contamination, the device area is limited to 250 x 250 μm^2, although larger device structures are possible. Dry etching is done by argon-ion-beam milling in a 5 x 10^{-3} argon environment. Wet-etching is done using a BHF or HF solution in low concentrations. Lift-off is used to define the Pt-layer. A photoresist layer is consecutively applied, patterned and covered by a film. Subsequently, the photoresist is removed using acetone. Polymeric photoresist cannot be used over 100°C,but lift-off compatible with high temperature deposition is possible using for example SrO and Al_2O_3 as mask, using shadow-mask deposition or wet or dry-etching of the photoresist layer defining the oxide lift off mask layer [9]. Shadow-masking is used to quickly fabricate device structures in-situ. A shadow-mask consisting of a SiN membrane is placed in close proximity to the substrate. Contact between the membrane and the substrate is avoided because of the possibility of buckling or cracking of the membrane. Device area cannot be controlled accurately due to broadening effects [10]. For all reported data, standard photolithography with wet and dry etching was used to define the oxide layers and a lift-of process to define the 200x200 μm^2 platinum top-electrodes.

3.4 Thin film characterization

3.4.1 Crystal structure

In this section, an overview of the characterization of the crystal structure by x-ray diffraction. First, a general explanation of theoretical explanation of x-ray diffraction is given, followed by a description of several scan types and the information that can be obtained from each scan type.

The crystal structures are determined by x-ray diffraction, based on the interference of x-rays scattered by lattice planes, present in any crystalline material. Fig. 3.1(a) depicts reciprocal space in the (h0l)-plane, in which each spot corresponds to a set of parallel crystal planes perpendicular to the (010) plane. Reciprocal space is described by momentum axes Q_h, Q_k and Q_l, corresponding to x, y and z cartesian axes, parallel to the a, b and c axes of the crystal. Intensity is observed if the diffraction vector G coincides with a reciprocal lattice spot. Momentum space is related to real space lattice parameters, using in-plane $a_1=2\pi/Q_{in}$ and out-of-plane $a_3=2\pi/Q_{out}$. The diffraction vector is related to the incoming beam with wave vector $\vec{k_i}$ and diffracted beam with wave vector $\vec{k_t}$, as $\vec{G} = \vec{k_t} - \vec{k_i}$. Since the length of both wave-vectors is determined by the wavelength, according to $\vec{k} = 2\pi/\lambda$, only the angles ω and 2Θ can be used to maneuver $\vec{G}$ in reciprocal space. Here ω is the angle between the sample surface and the incident beam and 2θ is the angle between incident beam and diffracted beam [11].

Different crystal structures of the film can be determined using x-ray diffraction, as shown in fig. 3.1(b). The first type shows epitaxial films which are perfectly single-crystal without defects. Ideal point-like peaks are obtained in re-

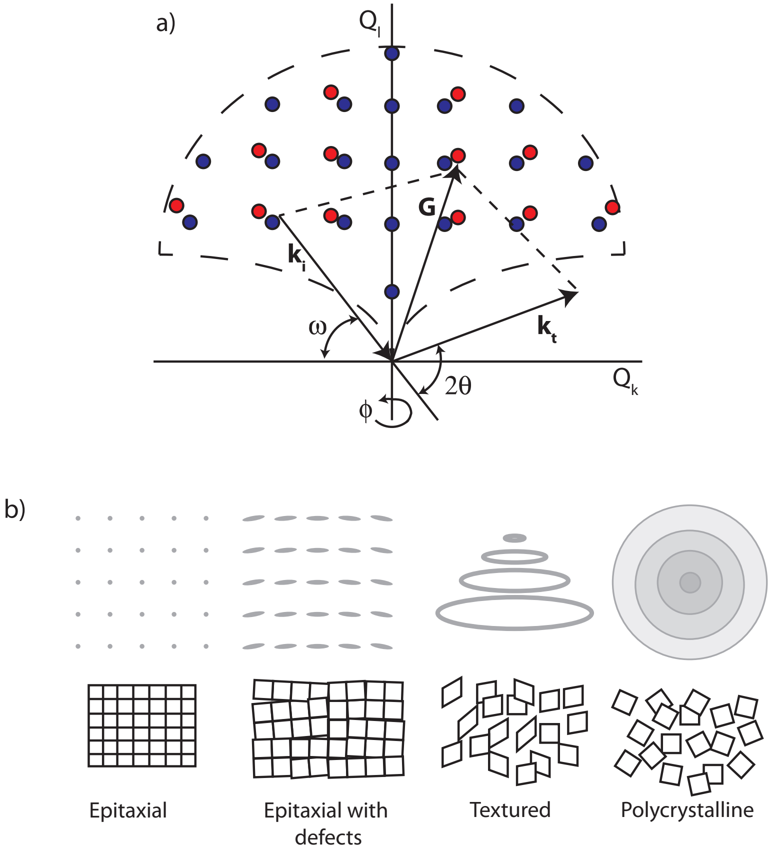

Figure 3.1: a) Reciprocal space and the relation between the diffraction vector G and incident beam vector k_i and diffracted beam vector k_t, and b) schematic crystallographic types in thin films with corresponding intensity configurations in reciprocal space.

ciprocal space. In the second type, mosaic spread is added to the epitaxial film, typically through the introduction of defects. In this case, peaks are elongated in the ω-direction. The third type shows a textured film, which is characterized by out-of-plane coherence but lacking in-plane coherency. The film will yield intensity-circles in reciprocal space. The fourth type is a polycrystalline film, with randomly orientated crystallites and thus a lack of in-plane and out-of-plane coherency. These films will generate spheres of intensity in reciprocal space. These spheres show up as spots in the (h0l)-plane.

Several x-ray diffraction scans are possible, depending on the path of the diffraction vector in reciprocal space. The most used scan is the Θ-2Θ scan, in which the diffraction vector is scanned along the surface normal in the (00x) direction. Here, 2Θ scans twice as fast as ω, so that $\Theta = \omega$ during scanning. This scan measures the out-of-plane lattice parameter (the d-spacing), since no information of the in-plane dimensions is measured. The mosaicity of the crystal can be measured by a rocking curve or ω scan. In this scan, a fixed 2Θ value is used and the diffraction vector describes a circle around the origin. The in-plane distribution of diffraction intensities is captured. The wider the distribution, the larger the mosaic spread of the crystal. In order to measure the in-plane symmetry of an epitaxial film, the diffraction vector is put at fixed 2Θ and ω values and the sample is rotated around the surface normal. A typical ϕ-scan of 360° on a 4-fold symmetric perovskite single crystal will yield 4 peaks.

Finally, next to scanning lines in reciprocal space, it is possible to capture planes in reciprocal space, creating reciprocal space maps (RSMs). Multiple peaks of the film and the substrate are displayed in a single scan, even if they are tilted with respect to each other. In case a mix of orientations or polydomain films is imaged, this method captures all peaks in a single scan without the chance of missing certain peaks. Reciprocal space maps are captured by scanning the 2θ-ω planes in reciprocal space, due to the use of a Vantec line detector that covers an angle of 9° of 2Θ. Subsequently, a transformation to momentum space is performed, using axes in-plane momentum $Q_{in}=(\frac{4\pi}{\lambda})\sin(\omega)\cdot\sin(\omega\text{-}\theta)$ and out-of-plane momentum $Q_{out}=(\frac{4\pi}{\lambda})\sin(\omega)\cdot\cos(\omega\text{-}\theta)$, with goniometric angles ω and 2θ in radians and wavelength λ of 1.540562 Å. Important to note is that in order to measure the lattice parameters of a crystal, the peak should have an in-plane value $h + k \neq 0$, so that the diffraction vector has an in-plane component. For these peaks θ is not equal to ω. Analysis of the domain structure is done using the (004) peaks, since the peak morphology and multiple peak patterns are more symmetric and intuitive in this way, in contrast to the scanning of asymmetrical peaks. In this thesis, high-resolution XRD on a Bruker D8 Discover was used for all x-ray diffraction measurements. For the RSMs a Vantec line detector is used. The precision of the values of the lattice parameters determined from the RSM on a typical PZT peak is estimated to be 0.1% by Gaussian peak-fitting. Temperature-dependent measurements were done using an *in situ* Anton-Paar hot stage.

3.4.2 Microstructure, surface morphology and local ferroelectric and piezoelectric properties

In this section, the characterization of the microstructure and domain structure by scanning electron microscopy and transmission electron microscopy, the surface morphology by atomic force microscopy and the local ferroelectric and piezoelectric properties by piezo force microscopy is described.

The microstructure of the thin films is studied using a scanning electron microscope (SEM), on a Zeiss-1550 HRSEM, operating between 0.2 and 30kV. In this technique a high-energy electron beam is scanning the surface of a sample [4]. The beam has a diameter of roughly 10 Åand energies between a few kV to 50 keV. The incoming primary electrons transfer energy inelastically to the electrons and the lattice in the sample. Secondary electrons are emitted from the sample onto a detector. Next to the inelastically scattered electrons, elastically backscattered electrons may be generated simultaneously, which are used in electron-back scatter diffraction. Typical use of the technique is to image the general topography, for example the sample uniformity, thickness uniformity, columnar structure and grain boundaries that may be present in the film.

Transmission electron microscopy (TEM) is a technique for which a beam of electrons is transmitted through a thin slice of material and interacts with the crystal lattice. A set of lenses creates a diffraction pattern or an image on a screen at the back of the sample. The technique is capable of higher resolution imaging than optical microscopes, since electrons exhibit a small de Broglie wavelength, smaller than for example photons. Contrast is formed due to a complex combination of absorption and scattering of electrons. Charged electrons interact with the periodic potential field of the lattice. A structure factor describes the diffraction in a similar way to x-ray diffraction. Since diffraction depends on the electronic properties, TEM is also sensitive to the ferroelectric polarization of the sample. TEM is capable of imaging in several modes, selected area electron diffraction (SAED), high-resolution transmission electron microscopy (HRTEM), bright-field (BF) and dark-field (DF). BF uses the bright central diffraction spot to image, DF uses an off-centre spots. Therefore BF is more sensitive to absorption, while DF is more sensitive to scattering and the orientation changes of crystallites. In this work, cross-sectional samples were prepared using dimple-grinding followed by ion-milling. TEM imaging was done on a FEI Titan. In all images, the horizontal direction is parallel to the film surface and the vertical direction is normal to the film surface. It should be noted that due to the wedge shaped grinding, a thickness profile is present in the images. Therefore the optimal imaging is obtained in the thin part of the film (1-30 nm), when the largest intensity and no overlapping domains are present.

The surface properties of the films can be imaged using scanning probe microscopy. In this class of techniques, a mechanical probe is scanned in contact or near a surface and local information on the topography, conductivity, dielectrity, ferroelectric polarization, elastic properties, thermal properties, magnetic properties or semiconducting properties are obtained. In this thesis, Atomic Force Microscopy (AFM) is used to image surface morphology of substrates and films [12]. A micromachined cantilever with a tip with a radius of approximately 20 nm is brought in contact with the sample. The deflection of the cantilever is changed along with the height of the sample that is underneath the tip. Using a laser reflection on the top of the cantilever this deflection is measured. An electronic feedback system coupled to a piezoelectric transducer makes sure the deflection is limited to an optimum set point. An advanced feature of the used atomic force microscope apparatus (Bruker Icon) is the ability to map the local conductivity of a surface, using conducing atomic force microscopy (CAFM). A conducting atomic force microscopy probe connected to a sensitive amplifier and detector can measure currents as small as 10^{-12} A between a biased tip and a conducting path in the film. In this thesis, a Bruker Icon system in contact mod is used, with tips of a force constant of 4 N/m and coated with platinum in case of CAFM. The typically scan area is 2x2 or 5x5 μm^2.

Local ferroelectric and piezoelectric properties can be imaged by piezo force microscopy [13] [14]. In this variant of atomic force microscopy, a high-frequency ac-bias is applied the conducting AFM tip generating an electric field between the tip and the bottom electrode of the thin films stack. A piezoelectric deformation of the surface is then analyzed using the tip deflection. The amplitude and phase of this signal gives information about the piezoelectric effect and ferroelectric polarization direction, respectively [15]. The polarization direction can be characterized in both the in-plane and the out-of-plane direction on a surface [16]. The in-plane signal is based on torsion of the cantilever, which is measured perpendicular to the cantilever direction. The sample needs to be rotated 90° to image the second in-plane direction. The polarization can be switched locally by applying an electric field larger than the local coercive field of the film [17], allowing indications of the local coercive field value and imaging of the domain-wall dynamics [18]. The technique is often used to proof ferroelectricity in films in the case that high leakage currents prevent macroscopic ferroelectric measurements. PFM is performed using similar tips and scan range as the CAFM measurement.

3.4.3 Functional properties

The out-of-plane polarization - electric field P-E hysteresis loops are recorded using a sawtooth wave function at a frequency of 10 - 1000 Hz and an amplitude of 200kV/cm, using a modified Sawyer-Tower circuit (aixACCT Analyzer TF2000). The charge that is flowing at the capacitor electrodes is measured, giving a current - field (I-E) curve. This curve consists mainly of the ferroelectric switching current, however space charges and leakage currents may influence the measurements [19]. The P-E loop is obtained by integration of the collected current.

The dielectric constant - electric field (ϵ_r-E) loop are measured using an ac-ripple voltage (V$_{ac}$=0.05V, f=1kHz-1MHz) superimposed onto a slow scanning DC-voltage, using a Keithley 4200 Semiconductor Characterization System (4200-SCS). The dielectric constant (relative permittivity ϵ_r) of a parallel plate capacitor is calculated as $\epsilon_r = \frac{Cd}{\epsilon_0 A}$, where ϵ_0 is the permittivity of free space, C the measured

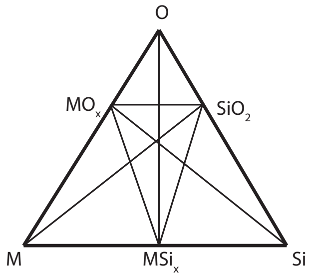

Figure 3.2: Ternary binary oxide silicon phase diagram at constant temperature and pressure, in case of single intermediate reaction phases on all three basic axes.

capacitance, d the thickness and A the area of the electrodes. Alternatively, the dielectric constant at E = 0 V/m can be derived from the slope of the P-E loops at E = 0 V/m. The latter method resembles the method that is usedto derive ϵ_r from the theoretically calculated PE-loops.

The piezoelectric properties have been measured using a Laser Doppler Vibrometer (LDV) on a Polytec MSA-400 system. The amplitude of a high-frequency deformation of a piezoelectric material is detected through the doppler shift of the laser interference. The system is based on a Michelson interferometer that measures shift of the interference fringes, that is induced by a change of length of the measurement laser beam with respect to the reference laser beam [20]. Provided good vibration filtering is applied and the frequency is larger than roughly 500 Hz, deformations can be detected with a resolution of roughly 5 pm [21]. A lock-in amplifier (Stanford Research Systems SR830) is used to detect the high frequency deformation. Typical operation is done using a small ac-signal of 200 mV at 8 kHz, on top of a slow scanning DC-bias voltage.

3.5 Growth of epitaxial buffer layers on silicon

The epitaxial growth of perovskites on silicon is challenging. The chemical reactivity of silicon with most materials is high, yielding silicates and silicides, which are prone to destroy the epitaxial relation. Furthermore, lattice parameter match is required in order to obtain a epitaxial relation between the silicon and the film and to limit the formation of misfit dislocations. In this section, both these requirements are used to identify zirconium and strontium as suitable candidates and for the growth of an epitaxial buffer layer directly on silicon.

If a binary oxide of the form MO_x is brought in contact with silicon, the possible reactions between the supplied elements M, Si and O are described by the M-Si-O ternary system, as illustrated in fig. 3.2. All intermediate reaction products, MO_x, SiO_2 and MSi_x are shown as well, connected by lines between the compounds. The Gibbs energy is used to determine the thermodynamic stability of the two compounds in contact. A metal-oxide oriented system is found if this compound has lower Gibbs free energy than the metal silicides. The thermodynamics of a wide range of binary oxides in contact with silicon has been studied previously [22]. It was found that all studied binary oxides are unstable, except beryllium (Be), magnesium (Mg) and zirconium (Zr). Furthermore ambiguous results still exist on a range of materials, such as strontium (Sr), yttrium Y and calcium (Ca). In practice, not only chemical reactivity is important, also the supply of materials can limit undesirable reactions. In pulsed laser deposition, the oxygen supply can be regulated by the background gas. Furthermore, the presence of a native oxide (SiO_2) of 1-2 Åon the silicons substrate is changing the supply of elements in the reactions. The deposited materials can react with the native oxide, a phenomenon that is called oxygen scavenging [2, 23] and is needed to obtain epitaxial growth of the material on silicon. By reducing the oxygen supply in the background gas one can compensate for the oxide in the form of native oxide.

Based on the described requirements, yttria-stabilized zirconia (YSZ, $8\%Y_2O_3$, $92\%ZrO_2$) is chosen as material for the growth of a buffer layer on silicon. This material consists of zirconia with 8% yttria to stabilize the rhombohedral ZrO_2 into a cubic lattice with fluorite structure and has a lattice parameter of 5.14 Å. The deposition parameters were described in sec. 3.3.1. By regulating the oxygen pressure during the initial growth of YSZ, the ratio of oxygen with respect to the other elements in the Zr-O-Si ternary system can be controlled. By limiting the supply of oxygen the deposited material is forced to react with the native oxide on the surface of the silicon. The amount and time of oxygen exposure during the first pulses needs to be accurately tuned to obtain a coherent (001) oriented epitaxial layer.

In order to check the optimum period of growth in Ar background pressure during the first pulses, Θ-2Θ x-ray diffraction is used. First, a YSZ buffer layer is grown, with time of the Ar step of 20, 30, 40 and 50 seconds. Then the YSZ layer is finished in normal deposition conditions, followed by PZT heterostructure consisting of a (110)-oriented SRO and a (110)-oriented PZT. The intensity of the PZT (110) peak was measured, and compared to the (001) peak. Fig. 3.3(a) shows the ratio of the intensities as a function of time of the YSZ growth in Ar. There is a clear optimum in (110)-oriented PZT at an Ar-step of 30 seconds. Fig. 3.3(b) shows the Si-YSZ interface after cooling [24], with the transmission electron microscopy image in selected area electron diffraction image (SAED) mode of the YSZ layer. An epitaxial relation is seen between the top YSZ and the Si. In between a region of amorphous material is found, which is likely regrown after cooling by oxygen permeation through the YSZ to the interface. It is noted that an alternative method for the removal of the native oxide is described by many reports, using dipping of the silicon substrate in an HF solution. In this work, epitaxial YSZ layer on HF-dipped silicon [25] and non-dipped silicon have been obtained. The non-dipped substrates resulted in films with a higher degree of crystallographic coherency and a lower surface roughness, than the HF-dipped substrates. Therefore, the non-dipped substrates were used for the fabrication of YSZ buffer layers.

Another candidate material that is stable on silicon is strontium. The forma-

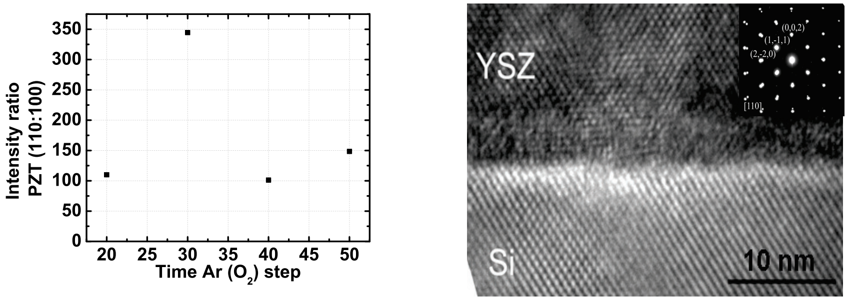

(a) (b)

Figure 3.3: a) (110):(100)-PZT peak intensity ratio as a function of Argon deposition time of the intitial growth of YSZ on silicon, and b) TEM image of the resulting epitaxial interface between YSZ and silicon

tion of SrO is characterized by a lower Gibbs energy than Zr, and therefore is less capable of oxygen-scavenging. This implies that the oxygen should be controlled even more accurately, in comparison to the case of YSZ. Epitaxial growth of SrO and $SrTiO_3$ on silicon has been reported in an UHV-system using Molecular Beam Epitaxy, by accurate control of the deposition parameters for each atomic layer [26]. These stringent conditions have up till now been obstacles for the fabrication of an epitaxial SrO film by pulsed laser deposition. Indications are present that the ultra-high vacuum background ($P<10^{-9}$ mbar) is needed to prevent the spontaneous growth of an native silicon oxide layer. Another effect that might become important for pulsed laser deposition on silicon is the relatively high kinetic energy of particles, that might damage the substrate surface, and soft-landing deposition parameters need to be developed [27]. Recent experiments have shown that the chemical properties of the deposited films are prevalent over the kinetic properties after growth of the first layer [28], and therefore a pathway to obtain high-quality buffer layers of strontium titanate on silicon by pulsed laser deposition is open to be explored.

In conclusion, the growth of a stable epitaxial buffer layer of YSZ on silicon substrates is obtained by pulsed laser deposition, using accurate control of the oxygen background gas pressure and an additional buffer layer of CeO_2.

3.6 Procedure to switch the crystallographic orientation from (110) to (001) on YSZ-buffered silicon

The growth of epitaxial complex oxide heterostructures on silicon using a YSZ buffer layer yields (110) oriented SRO and $Pb(Zr_x,Ti_{1-x})O_3$ (PZT) films. This section will show a procedure to switch the out-of-plane crystal orientation of SRO and PZT films on a this template from (110) to (001). This procedure consists of a change of the deposition parameters of the initial pulses of SRO and the addition of a layer of CeO_2 in order to improve epitaxial matching. The effect of the crystallographic orientation on the ferroelectric properties is analyzed. This work is published as [29].

The growth of SRO, followed by PZT with composition $x = 0.52$, on YSZ/Si template at normal conditions (600°C, 0.1 mbar) results in (110) oriented layers. X-ray diffraction (XRD) is used to determine crystal orientation for in-plane and out-of-plane directions. A description of the x-ray diffraction method can be found in sec. 3.4.1. Fig. 3.4(a) shows the Θ-2Θ-scan, containing the PZT (110) and SRO (110) peaks, together with YSZ (002) and Si (004) peaks. The out-of-plane epitaxial relationship is PZT(110)$\|$ SRO (110) $\|$ CeO_2(001) $\|$ YSZ(001) $\|$ Si(001). In-plane analysis is done by a ϕ-scan, on the (002) PZT and the (202) Si, see fig 3.4(b). Four sets of PZT peaks are obtained, consisting of two peaks in-plane rotated by +10° and -10° with respect to the silicon peak. For each peak, the (111)-direction of SRO is aligned to the (110)-direction of YSZ (SRO(111) $\|$ CeO_2(110)), as illustrated in fig. 3.4(c). Concluding, four crystallographic twin variants are present and each twin variant is 2-fold symmetric under 180° rotation of ϕ.

By depositing the first pulses at a high temperature (T_d=800°C) and lower oxygen pressure ($p(O_2) < 10^{-5}$), the orientation of the SRO film on the buffer layer can be switched from (110) to (001). This mechanism stems from the fact that the volatile ruthenium is evaporated at a high temperature of the substrate. In this way, SrO deposition from a SRO ablated species can be obtained. The initial pulses of a film (~ 4 $\AA$) are important to determine the growth orientation. By increasing the temperature and decreasing the oxygen background gas pressure in the first pulses, a Sr-rich starting layer is obtained, as was determined by x-ray photoelectron spectroscopy (not shown). Continued growth of stoichiometric SRO at normal deposition conditions results in (001) growth. It should be noted that on top of the YSZ a CeO_2 (a=5.41 Å, a_{fd}=3.83 Å) film should be used, to overcome the large epitaxial mismatch between YSZ (a=5.14 Å, a_{fd}= 3.63 Å) and SRO (a=3.93 Å). Fig. 3.4(d) gives the Θ-2Θ-scans showing the (001) PZT and (002) PZT and SRO reflection, together with the CeO_2 (002) and YSZ (002) peaks. The out-of-plane epitaxial relationship is PZT(001)$\|$ SRO (001)$\|$$CeO_2(001)\|$YSZ(001)$\|$Si(001). It should be noted that the intensity of the PZT peaks of the (110) oriented film is much lower than of the (001) oriented film, due to the lower coherence of the film. Fig. 3.4(e) shows the ϕ-scan with a 45° shift of the SRO (101) compared to the Si (202) fourfold symmetry related peaks. This proves that SRO and PZT are in-plane rotated, as schematically drawn in 3.4(f). For the (001) oriented SRO film, to the (110) axis of the (001) oriented CeO_2 perovskite block is aligned to the (100) axis of the CeO_2 block (see fig. 3.4). The ϕ-scan indicates that no twinning is present in the (001) oriented films, as it is in the (110) films.

The P-E hysteresis loops, I-V switching currents and remanent polarization P_r as function of the number of cycles for of the (110) oriented PZT films are shown in fig. 3.5(a), (b) and (c), respectively, and for (001) oriented films in fig. 3.5(d),

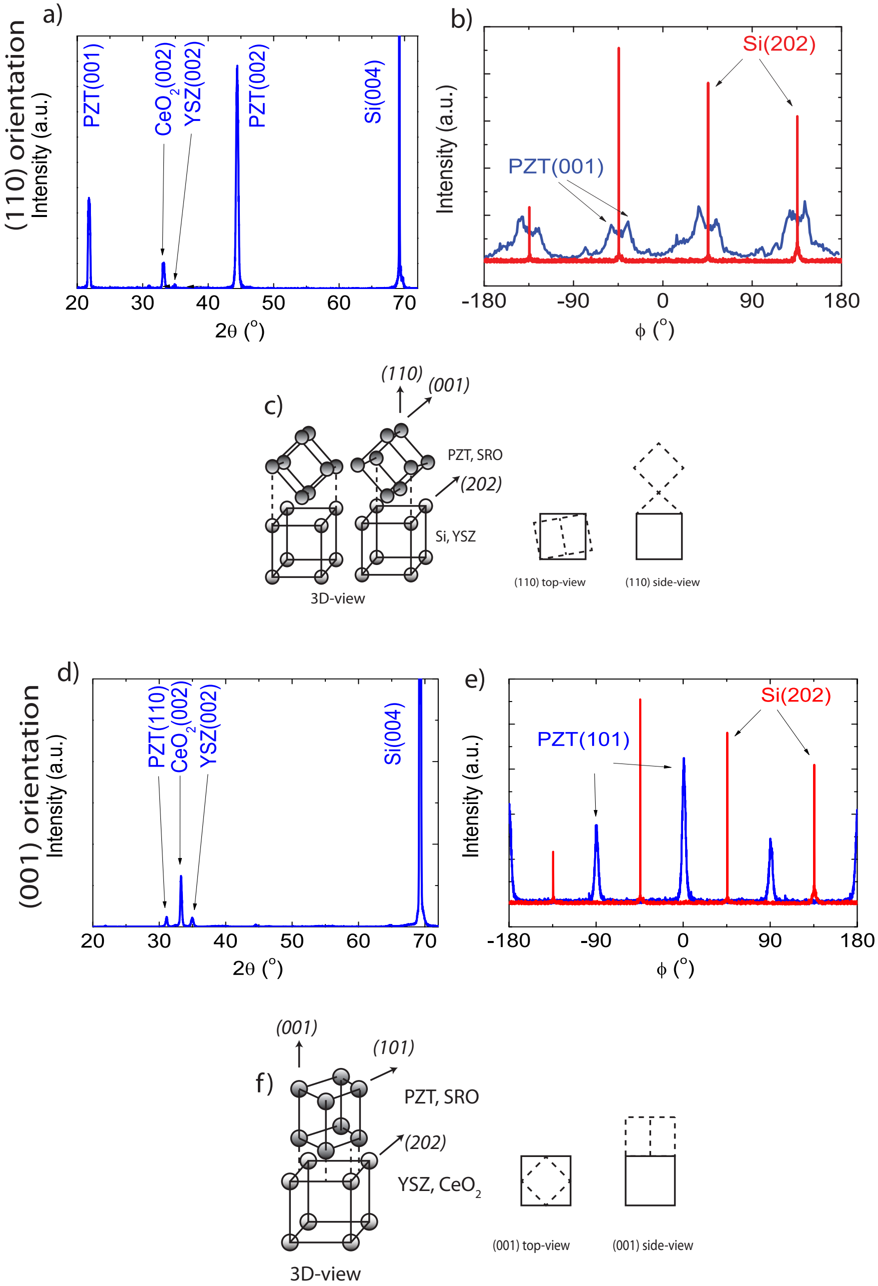

Figure 3.4: Θ-2Θ scan of the a) (110)-oriented PZT film, b) ϕ-scans of the (001) PZT and the (202) Si peak, and c) schematical thee dimensional view, top view and side view of the epitaxial relation of the (110) PZT film and the silicon substrate. d) shows the Θ-2Θ scan of the a) (001)-oriented PZT film, b) ϕ-scans of the (101) PZT and the (202) Si peak, and c) schematical thee dimensional view, top view and side view of the epitaxial relation of the (001) PZT film and the silicon substrate.

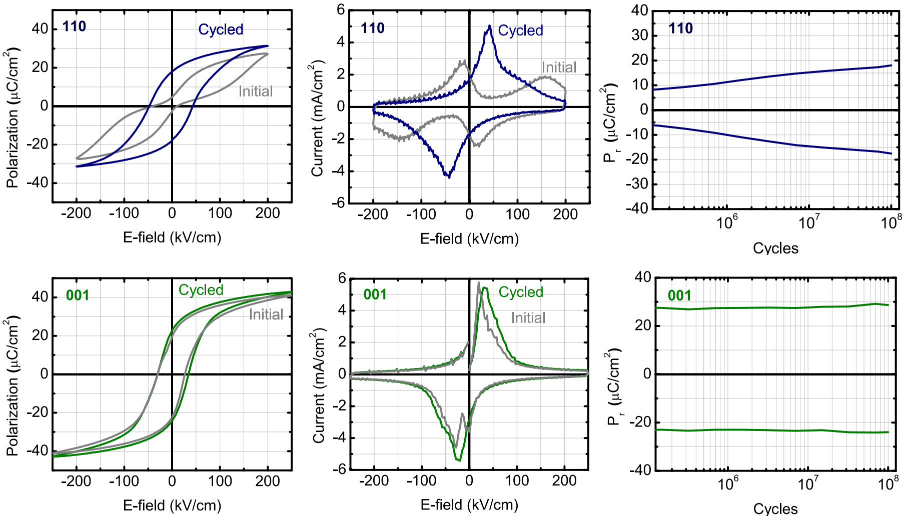

Figure 3.5: P-E loops, I-V loops and fatigue graphs of (110) and (001) oriented films

(e) and (f). The initial loops for the (110) oriented films show an unusual shape of the hysteresis loop, with low P_r and two loops for positive and negative E-field. The current - electric field (I-E) loops show two switching peaks, at coercive field $E_c \approx 0$ kV/cm and E = ± 150 kV/cm. After cycling the P-E loop 10^8 times, the loop shape changes drastically. A classical ferroelectric P-E loop is obtained and a single switching peak in the I-E curve at E_c=40 kV/cm, which is significantly lower than for the (110) film. The fatigue behavior shows an increase of P_r (from P_r=5 μC/cm^2 to P_r is 18 μC/cm^2). The (001) oriented films show different behavior, a classical ferroelectric loop is observed for the initial and cycled case. The I-E loop does not change significantly either and a stable P_r is observed.

The difference in behavior may originate from the multiple twin domains in the (110) which are not present in the (001) film, observed in fig. 3.4. Defective crystal planes between the crystallographic domains exist. The ferroelectric domain-walls are pinned at space charges, which are collected at these defects. Subsequent cycling removes the space charge and changes the domain-wall mobility, as seen from a change of the E_c. A second possible explanation is related to the crystal orientation directly and the associated direction of the polarization vector. For PZT with $x = 0.52$, either a tetragonal phase is present with a polarization in the (001) or (100) direction, or a monoclinic phase is present with the polarization in the (111) direction. None of these polarization direction is parallel to the poling direction, which is normal to the surface. During cycling an effective poling process changes the polarization direction towards the out-of-plane (110) direction and leads to a changing switching mechanism.

In conclusion, a procedure to switch the crystal orientation from (110) to

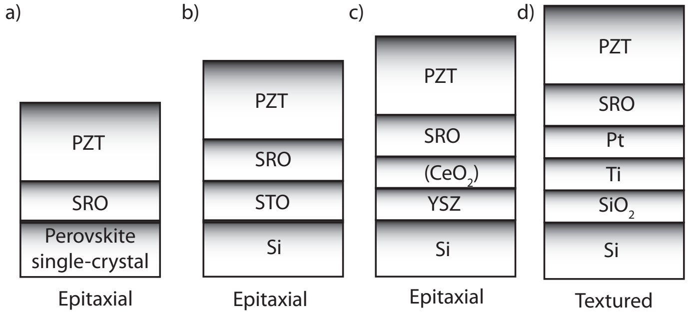

Figure 3.6: Templates for growth of PZT heterostructures with the types of crystallographic properties of the SRO and PZT, epitaxial or textured.

(001) is developed and the associate switching properties are related to in-plane structural domains. The structure of different crystallographic oriented PZT thin films on silicon substrates and ferroelectric properties has been studied.

3.7 Effect of growth template on crystal quality

The fundamental study of properties of the PZT heterostructures require high-quality films. Domain-wall pinning on defects and impurities prevent the study of the intrinsic properties. The mosaic spread of the film determines the peak width in x-ray diffraction and the error margins on measurement of the lattice parameters. Therefore epitaxial films are needed. Since any stacking fault or grain boundary will be transferred to an overgrown layer, the quality of the buffer layer is important. In this section, the mosaic spread and microstructure of films on the different buffer layers on silicon is compared to films on single-crystal substrates and on platinized silicon, the template that is used for PZT films based applications, see ch. 7.

Fig. 3.6 shows a schematic drawing of an epitaxial stack on a (a) single-crystal substrate, on (b) STO- buffered Si, on a (c) (CeO_2/)YSZ/Si stack and on a (d) platinized wafer. The epitaxial growth of PZT on single-crystal substrates is routinely achieved, as described by sec. 3.2. Epitaxial PZT heterostructures on silicon are achieved by pulsed laser deposition of a YSZ buffer layer, as is described in section 3.5. The (CeO_2/)YSZ/Si stack uses CeO_2 to obtain (001) orientation. An STO buffer layer on silicon by Molecular Beam Epitaxy has been demonstrated. This layer exhibits a mosaic spread of 0.23° at full-width-half-maximum (FWHM). Pulsed laser deposition of epitaxial STO buffer layer on silicon has not been demonstrated. As section 3.5 explains, it is related to technical obstacles such as the vacuum of the growth environment. The platinized wafer no epitaxial growth is possible. It results in a fiber-textured PZT film, in which the crystal shows out-of-plane coherency but no in-plane coherency, as was described in sec. 3.4.1. The platinized silicon consist from the top of subsequently Platinum(Pt),

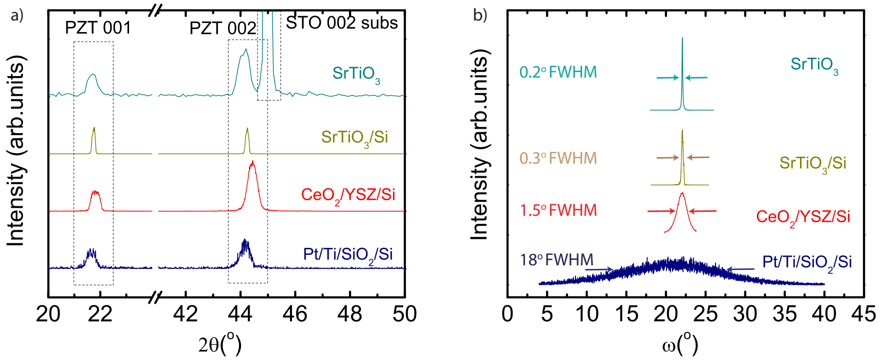

Figure 3.7: a) Θ-2Θ of all used heterostructures, b) Rocking curves of the (002) of all used heterostructures

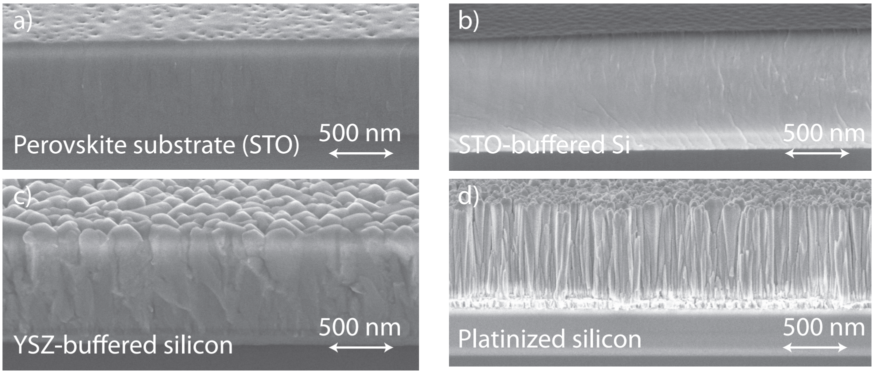

Figure 3.8: Scanning Electron Microscopy images of used sample geometries a) single-crystal substrate, b) STO buffered template, c) YSZ buffered template and d) Platinized silicon (Pt/Ti/SiO2/Si) template

Titanium(Ti) adhesion layer, silicon oxide (SiO_2) and the substrate silicon (Si). The Pt top electrode is similar for all templates (not shown).

X-ray diffraction is used to analyzed the quality of the films. The Θ-2Θ scans in fig. 3.7(a) show that a (001) orientation is obtained on all templates. Subsequently, the out-of-plane coherence of the film is quantified by the mosaic spread of the rocking curve (ω scan) in FWHM angles. Fig. 3.7(b) shows the rocking curves of the (004) peak for all templates. The obtained FWHM values for the mosaic spread at FWHM of the single-crystal substrate, CeO_2/YSZ/Si stack, STO/Si and platinized wafer (Pt/Ti/SiO_2/Si) are respectively 0.2°, 0.3°, 1.5° and 18°.

Figure 3.8 shows scanning electron microscopy images of all used sample geometries. The PZT film on single-crystal substrates and the STO-buffered silicon shown no large grain boundaries. The PZT on the CeO_2/YSZ/Si template shows a typical vertically oriented columnar structure. The film on platinized wafer has the most disordered columnar structure, followed by the CeO_2/YSZ/Si template. The STO/Si and single-crystal STO show the least disorder. In conclusion, in order to study intrinsic properties the high crystal quality of single-crystal substrates and the STO buffered silicon is preferred over the CeO_2/YSZ/Si and platinized silicon templates.

3.8 Conclusions

In this chapter, several aspects of epitaxial PZT heterostructures on silicon have been described. The fabrication and characterization are explained, followed by a discussion of the growth of epitaxial buffer layers on silicon, the control of crystal orientation on these buffer layers and the resulting quality of the epitaxial PZT heterostructures on silicon.

3.9 References

[1] C.B. Eom, R.B. Van Dover, J.M. Phillips, D.J. Werder, J.H. Marshall, C.H. Chen, R.J. Cava, R.M. Fleming, and D.K. Fork. Fabrication and properties of epitaxial ferroelectric heterostructures with $SrRuO_3$ isotropic metallic oxide electrodes. *Appl. Phys. Lett.*, 63(18):2570–2572, 1993.

[2] D.K. Fork, D.B. Fenner, A. Barrera, J.M. Phillips, T.H. Geballe, G.A.N. Connell, and J.B. Boyce. Buffer layers for high-quality epitaxial $YBCO$ films on Si. *IEEE Transact. Appl. Supercond.*, 1(1):67–73, 1991.

[3] Z. Yu, Y. Liang, C.D. Overgaard, X. Hu, J.A. Curless, H. Li, Y. Wei, B. Craigo, D.C. Jordan, and R. Droopad. Advances in heteroepitaxy of oxides on silicon. *Thin Solid Films*, 462:51–56, 2004.

[4] M. Ohring. *Materials science of thin films.* Academic Press, London, 2 edition, 2002.

[5] G. Shirane, K. Suzuki, and A. Takeda. Phase transitions in solid solutions of $PbZrO_3$ and $PbTiO_3$ (ii) x-ray study. *J. Phys. Soc. Japan*, 7:12, 1952.

[6] G. Shirane and K. Suzuki. Crystal structure of $Pb(Zr,Ti)O_3$. *J. Phys. Soc. of Japan*, 333:1–1, Sep 1952.

[7] M.P. Warusawithana, C. Cen, C.R. Sleasman, J.C. Woicik, Y. Li, L.F. Kourkoutis, J.A. Klug, H. Li, M.P. Ryan, L.P. Wang, M. Bedzyk, D.A. Muller, L.Q. Chen, J. Levy, and D.G. Schlom. A ferroelectric oxide made directly on silicon. *Science*, 324(5925):367–370, Apr 2009.

[8] R. Eason. *Pulsed laser deposition of thin films - Applications-led growth of functional materials.* Wiley, 2006.

[9] N. Banerjee, M. Huijben, G. Koster, and G. Rijnders. Direct patterning of functional interfaces in oxide heterostructures. *Appl. Phys. Lett.*, 100(041601), 2012.

[10] P. te Riele, G. Rijnders, and D. Blank. Ferroelectric devices created by pressure modulated stencil deposition. *Appl. Phys. Lett.*, 93(23), 2008.

[11] K. Saito. *Polar Oxides.* Number ISBN 3-527-40532-1. Wiley-VCH Verlag GmbH Co KGaA, 2005.

[12] J. Broekmaat. *In–situ growth monitoring with scanning force microscopy during pulsed laser deposition.* PhD thesis, University of Twente, 2008.

[13] S.V. Kalinin, A.N. Morozovska, L.Q. Chen, and B.J. Rodriguez. Local polarization dynamics in ferroelectric materials. *Rep. Progr. Phys.*, 73:056502, 2010.

[14] C. Harnagea. Local piezoelectric response and domain structures in ferroelectric thin films investigated by voltage-modulated force microscopy. *PhD Thesis, Martin-Luther-Universität Halle Wittenberg*, pages 1–97, 2001.

[15] B.K. Nagarajan, A.L. Roytburd, A. Stanishevsky, S. Prasertchoung, T. Zhao, L. Chen, J. Melngailis, O. Auciello, and R. Ramesh. Dynamics of ferroelastic domains in ferroelectric thin films. *Nat Mater*, 2(1):43–47, 2002.

[16] A.L. Kholkin, S.V. Kalinin, A. Roelofs, and A. Gruverman. *Review of Ferroelectric Domain Imaging by Piezoresponse Force Microscopy*, volume 1. Springer Science+Business Media, 2007.

[17] T. Tybell, P. Paruch, T. Giamarchi, and J.M. Triscone. Domain wall creep in epitaxial ferroelectric $Pb(Zr_{0.2}, Ti_{0.8})O_3$ thin films. *Phys. Rev. Lett.*, 89(9):97601, 2002.

[18] V.V. Shvartsman and A.L. Kholkin. Domain structure of $0.8Pb(Mg_{1/3}, Nb_{2/3})O_3 - 0.2PbTiO_3$ studied by piezoresponse force microscopy. *Phys. Rev. B.*, 69(1):14102, 2004.

[19] P. te Riele. *Direct patterning of oxides by pulsed laser deposition.* PhD thesis, University of Twente, September 2008.

[20] Z. Huang, G. Leighton, R. Wright, F. Duval, H.C. Chung, P. Kirby, and R.W. Whatmore. Determination of piezoelectric coefficients and elastic constant of thin films by laser scanning vibrometry techniques. *Sens. Act. A.*, 135(2):660–665, 2007.

[21] A.L. Kholkin, C. Wütchrich, D.V. Taylor, and N. Setter. Interferometric measurements of electric fieldinduced displacements in piezoelectric thin films. *Rev. Sci. Instr.*, 67:1935, 1996.

[22] K.J. Hubbard and D.G. Schlom. Thermodynamic stability of binary oxides in contact with silicon. *J. Mater. Res.*, 11(11):2757–2776, 1996.

[23] Q. Li, S.J. Wang, P.C. Lim, J.W. Chai, A.C.H. Huan, and C.K. Ong. The decomposition mechanism of SiO_2 with the deposition of oxygen–deficient $M(HforZr)O_x$ films. *Thin Solid Films*, 462:106–109, 2004.

[24] M.G. Maas. Integrating PZT in silicon technology by pulsed laser deposition. Master's thesis, University of Twente, 2007.

[25] M.D. Nguyen, R.J.A. Steenwelle, P.M. te Riele, J.M. Dekkers, D.H.A. Blank, and G. Rijnders. Growth and properties of functional oxide thin films for piezomems. In *Proc. EUROSENSORS 22nd (Dresden, Germany)*, pages 810–3. Proc. EUROSENSORS 22nd (Dresden, Germany), 2008.

[26] J. Reiner, A. Kolpak, Y. Segal, and K. Garrity. Crystalline oxides on silicon. *Advanced Materials*, XX:1–20, 2010.

[27] P. de Veen. *Interface Engineering for Organic Electronics.* PhD thesis, University of Twente, 2011.

[28] Y. Chen, N. Pryds, J. Kleibeuker, G. Koster, J. Sun, E. Stamate, B. Shen, G. Rijnders, and S. Linderoth. Metallic and insulating interfaces of amorphous srtio 3-based oxide heterostructures. *Nano Letters*, XXXX(XXX):000–000, 2011.

[29] M. Dekkers, M.D. Nguyen, R. Steenwelle, P.M. Te Riele, D.H.A. Blank, and G.J.H.M. Rijnders. Ferroelectric properties of epitaxial $Pb(Zr, Ti)O_3$ thin films on silicon by control of crystal orientation. *Appl. Phys. Lett.*, 95:012902, 2009.

Chapter 4

Substrate-induced strain on the domain structure in epitaxial Pb(Zr,Ti)O_3 films with tetragonal compositions

Abstract

The relation between the domain fraction, the domain tilting and the substrate-induced strain of epitaxial Pb(Zr_x,Ti_{1-x})O_3 (PZT) films is studied, in the tetragonal phase towards the morphotropic phase boundary ($x = 0.2$, 0.4, 0.45). The substrate-induced strain is controlled through thermal expansion coefficient mismatch between film and the silicon, $KTaO_3$, $DyScO_3$ and $SrTiO_3$ substrates. A c/a domain structure is found, for which the domain fraction depends strongly on strain, while the lattice strain remains constant. A new geometrical model is derived for the temperature dependent domain-fraction. The tilting of the a and c domains is closely related to the domain fraction. For large c domain fraction, tilting of the a-domain is much larger than of the c-domain, while for an intermediate c-domain fraction, the tilting values are equal. The angle between the domains is invariant with strain, and the domain tilting is described by a new geometrical model.

4.1 Introduction

The deposition of perovskite films on silicon (Si) wafers is attracting great interest, since it promises the possibility of mass-production of thin-film devices with functional mechanisms such as piezoelectricity, ferroelectricity, superconductivity, magnetism, and dielectricity [1]. PiezoMEMS using $Pb(Zr_x,Ti_{1-x})O_3$ (PZT) films on Si are often viewed as forerunner in this trend [2] and the understanding of the effects of the substrate on the crystal structure is of high interest. The recently achieved high-quality epitaxial PZT films on Si substrates by Pulsed Laser Deposition (PLD) offer the opportunity to study the fundamental study of the relation between ferroelectric and crystallographic properties [3, 4]. In these film the extrinsic effects, such as grain boundaries, mixed orientations, space charge or misfit dislocations, are minimized.

Epitaxial (001) PZT thin films are grown at a temperature of typically 600°C in the cubic phase. During cooling, film passes the phase transition and a large spontaneous strain emerges [5]. The substrate restricts the free in-plane shrinkage of the film and domains are formed in order to relax the generated stress [6]. For compositions with a low Zr-content, out-of-plane c-domains and in-plane a-domains are generated, forming the tetragonal c/a-phase. By using the epitaxial strain of different substrates, the c-domain fraction can be controlled [7], and a theory that is based on strain energy can be used to describe this mechanism [8]. It was shown that the in-plane component of the polarization is increased as function of tensile strain. [9]. For large tensile strains, the c/a phase transforms in a orthorhombic a_1/a_2 phase where all the polarization is in-plane [10]. On the boundary of both phases, a diffuse anomaly in the dielectric constant and piezoelectric coefficient is expected [11]. The domain formation in the c/a-phase is accompanied by tilting of the ferroelectric domains, to ensure crystallographic matching of adjacent domains. The tilt is often found to be proportional to the arctan of the tetragonality strain [12, 13]. However, a detailed analysis of the tilting of the individual domain as function of composition and substrate induced strain can reveal many detailed information of the described mechanisms.

PZT films that are used in applications are often thicker than 100 nm. For these thicknesses the epitaxial strain is relaxed by the creation of misfit dislocations. However, the difference in thermal expansion coefficients of the film α_f, $\approx 6{\cdot}10_6$/K for PZT, and substrate α_s leads to a significant strain that affects on the unit-cell parameters and domain formation. The large tensile thermal strain of the PZT film on Si, with α_s of $2.8{\cdot}10^{-6}$ K^{-1}, may be compared to the compressive thermal strain in the film on the single-crystalline oxide substrates, with α_s in the range of $6\text{-}11{\cdot}10^{-6}$ K^{-1}. The lattice parameters of film and substrate can be analyzed as a function of temperature, to gain insight in the thermal strain and strain relaxation processes.

In this chapter, an experimental study is presented on the relations between domain structure, lattice parameters, domain tilting, domain fraction and substrate-induced strain for 1 μm thick epitaxial (001)-oriented PZT films in the tetragonal phase towards the morphotropic phase boundary (Zr-content x = 0.2; 0.4 and

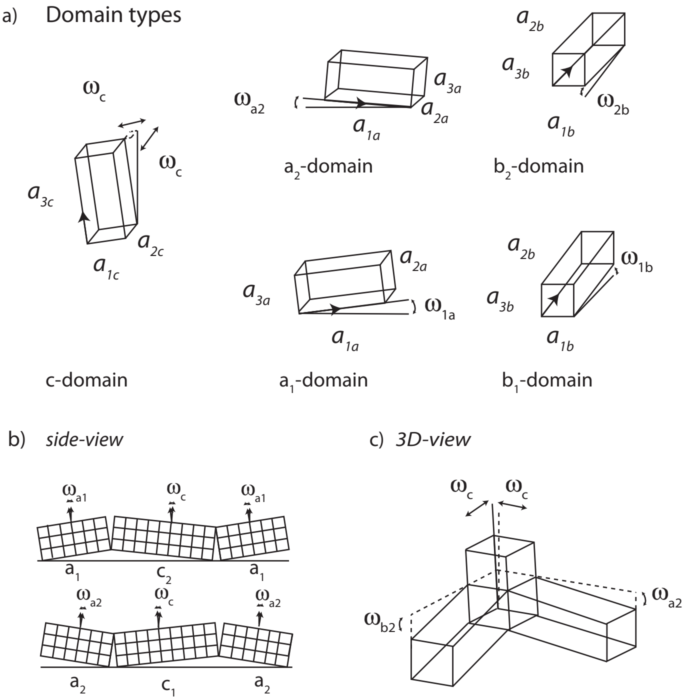

Figure 4.1: a) Schematical representation of domain types of c/a-phase with lattice parameters a_1,a_2 and a_3 and domain tilt angle ω, b) domain structure in cross-section in the (h0l)-plane and c) the 3-dimensional view of the c/a-domain structure.

0.45). First, x-ray diffraction in reciprocal space mapping mode is used to analyze the domain structure in terms of lattice parameters, domain fraction and domain tilting. A model for the relation between substrate induced strain and domain fraction is developed. The tilting of c and a domains are related to a new geometrical model as function of temperature and substrate-induced strain. The analysis of surface facets using atomic force microscopy is used to verify the domain tilting.

4.2 Description of the domain structure

4.2.1 Tetragonal c/a-phase

The domain structure in the tetragonal c/a-phase consists of a-domains, b-domains, and c-domains, with the respective polarization values in a cartesian coordinate system (x,y,z≡1,2,3) being $P_1 \neq P_2 = P_3 = 0$, $P_2 \neq P_1 = P_3 = 0$, and $P_3 \neq P_1 = P_2 = 0$. The domain structures are schematically shown in fig. 4.1(a). In the terminology of Kukhar *et al* [10], the lattice parameters of the a-domain are a_{1a}, a_{2a}, a_{3a}, of the b-domain are a_{1b}, a_{2b}, a_{3b} and of the c-domain are a_{1c}, a_{2c}, a_{3c}. The c/a

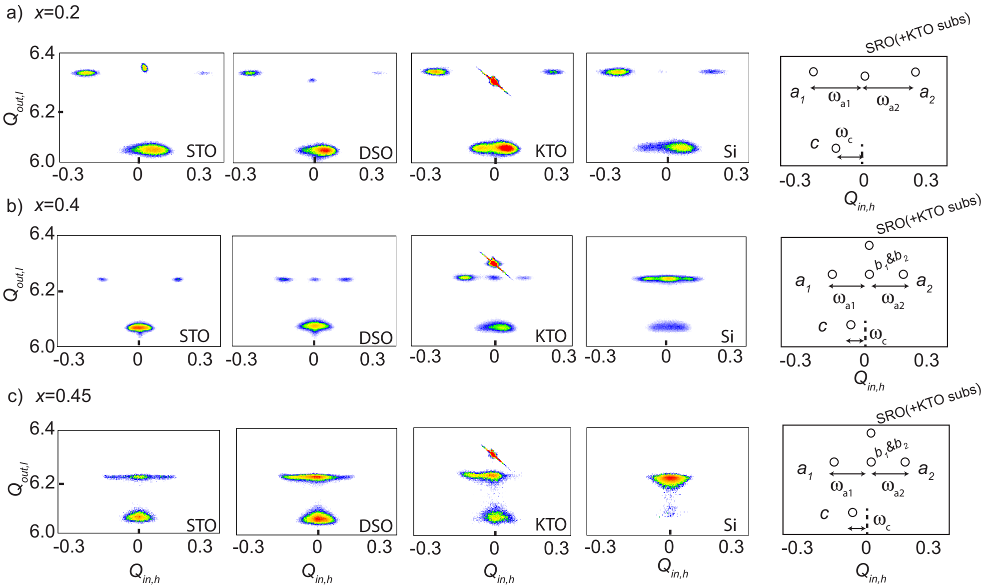

Figure 4.2: a) Typical (h0l)-Reciprocal Space Maps around (004)-peaks on all substrates and schematically drawn the expected peaks assigned to the domain types, for a) $x = 0.2$, b) $x = 0.4$ and c) $x = 0.45$. Intensity on log-scale in arbitrary units.

domain population is described using the domain (volume) fraction of c-domains ϕ_c [1]. Domains are slightly tilted with respect to each other and the film plane, to obtain a crystallographic match at the 90° domain walls.

At the border of two domains, a ferroelectric domain-wall connects the polarization and crystal. The domain-wall was studied in a paper by Kittel [12]. A maximum angle between the c and a-domains $\Delta\omega_{max}$ is related to the short and long tilted cell length a_1 and a_3 through

$$\Delta\omega_{max} = 2\arctan(a_3/a_1) - \pi/2 \tag{4.1}$$

The domain tilting is denoted by the angles ω_{a1}, ω_{a2} for the a_1 and a_2 domains, ω_{b1}, ω_{b2} for the b_1 and b_2 domains, with respect to the principal x-axis and y-axis. As we will see the c-domains are tilted with respect to the principal z-axis over the angle ω_c, equally in both the x-z and the y-z plane. Similarly, it is found that ω_{a1}=ω_{a2}=ω_{b1}=ω_{b2} $\equiv \omega_a$, as one would expect from the in-plane four-fold symmetry. If looked in cross-section in the (h0l)-plane, either a $a_1/c_2/a_1$ or $a_2/c_1/a_2$ domain structure is possible, see fig. 4.1(b). The three dimensional view of the resulting domain structure is shown in fig. 4.1(c). The angle between the a-domains and c-domains is experimentally determined as

$$\Delta\omega = \omega_a + \omega_c \tag{4.2}$$

ω_c is similar in both in-plane directions, as is ω_a and $\Delta\omega$. ω_a and ω_c have opposite sign.

4.3 Results

4.3.1 Domain structure

In order to study the domain structure, reciprocal space maps in the cross-sectional (h0l)-plane have been measured around the (004)-substrate peak for all substrates, as shown in fig. 4.2(a)-(c). Multiple diffraction spots are obtained, indicating a polydomain film. Each diffraction spot can be assigned to a single domain type. Schematical representations of the reciprocal space maps are shown, with all peaks assigned to domains. Note that domains with smaller lattice parameters are located at higher Q-values. For all studied compositions, a typical c/a-phase is observed: a mix of a-domains, b-domains and c-domains is present [14, 15].

The figures 4.2(d)-(f) show the plan-view (hk0)-scans of the films on Si. These scans are in close agreement with the (h0l)-scans. All films are scanned at the a-domains and c-domains. The a-domain scans show patterns with four lobes corresponding to a_1, a_2, b_1 and b_2 domains. The peaks having higher intensity indicating that the domain fractions of these domain are larger.

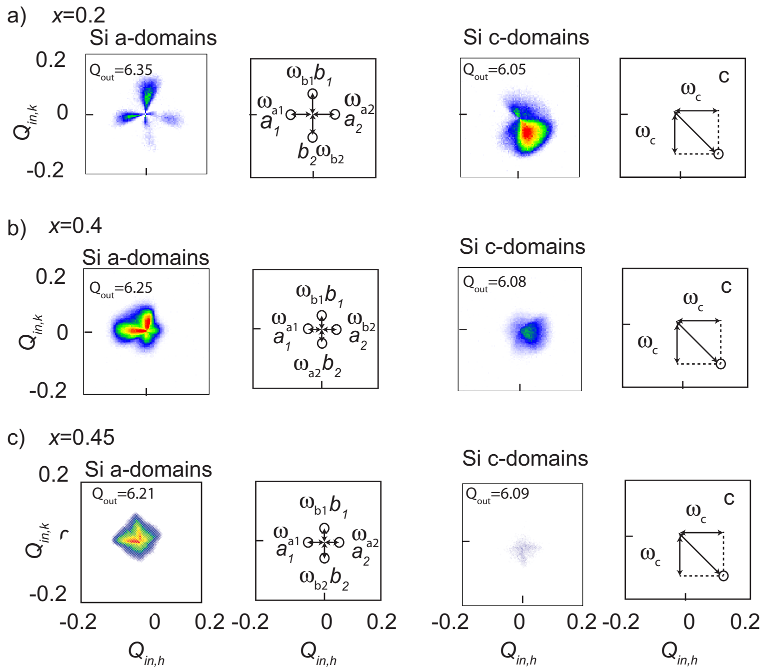

Figure 4.3: a) Typical (hk0)-Reciprocal Space Maps around (004)-peaks on Si substrate using constant l-value. Schematically drawn the expected peaks assigned to the domain types , for a) $x = 0.2$, b) $x = 0.4$ and c) $x = 0.45$. Intensity on log-scale in arbitrary units.

4.3.2 Lattice strain

In order to determine the lattice strain, the lattice parameters are derived from the peak positions of the reciprocal space maps and are plotted in fig. 4.4. The unit-cell dimensions are independent of thermal expansion coefficient of the substrate α_s. For $x = 0.2$, the lattice parameters can be classified in two regimes, a long-axis $a_3 \equiv a_{1a} \approx a_{2b} \approx a_{3c} \approx 4.150$ Åand a short axis $a_1 \equiv a_{2a} \approx a_{3a} \approx a_{1b} \approx a_{3b} \approx a_{1c} \approx a_{2c} \approx 3.970$ Å. For $x = 0.4$, similar behavior is observed, with $a_3 \approx 4.14$ Åand $a_1 \approx 4.035$ Å. For $x = 0.45$, $a_3 \approx 4.14$ Åand $a_1 \approx 4.04$ Å. The lattice parameters as function of composition are plotted in fig. 4.4(d). These values resemble data by other deposition methods [16]. The SRO bottom electrode layer is epitaxially strained on the substrate, since the peaks of the film and the substrate are located at similar Q_{in} values in a scan of the (103) peak (not shown). Next to the film parameters, α_s of the substrates are measured by temperature dependent reciprocal space mapping and found to be $2.8{\cdot}10^{-6}$ K^{-1},$6.7{\cdot}10^{-6}$ K^{-1}, $8.4{\cdot}10^{-6}$ K^{-1} and $11.0{\cdot}10^{-6}$ K^{-1} for Si, KTO, DSO and STO, respectively, agreeing well to literature values.

4.3.3 Domain fraction

The c-domain fraction ϕ_c(V) is calculated from the integrated peak-intensities [17] of all domains in 3 dimensional reciprocal space [1]. Values are plotted in fig. 4.5 for $x = 0.2$, 0.4 and 0.45 as function of α_s. The error bars on $\phi_c(V)$ are estimated to be ± 0.1. We find that ϕ_c increases from the tensile strained film on Si to the compressively strained film on STO. This observation is in agreement with trends observed in previous studies [8]. Furthermore ϕ_c depends more on α_s for higher Zr-content than for lower Zr-content. Therefore ϕ_c is equal for high α_s of STO and diverges for lower α_s. The ϕ_c values of Si, KTO and DSO show that ϕ_c depends on composition and is negatively correlated with the Zr-content and vice versa. A model for the domain fraction is developed in sec. 4.3.4, and is shown in fig. 4.5.

4.3.4 Model for the domain fraction

The effect of strain on the domain formation is studied. A qualitative analysis of the strain can be made using the domain stability maps and coherency strain introduced by Speck and Pompe [8]. Here, we introduce a more simple quantitative model, using the relative magnitude of a_1, a_3 and a_s^* to determine the c/a-domain

---

[1] The c-domain fraction ϕ_c(V) is calculated from integrated peak-intensities. The peak volume V of each domain is calculated and inserted into ϕ_c(V)=V$_c$/(V$_c$+V$_a$), in-line with previous reports. It is assumed that the peaks are Gaussian and symmetric in all reciprocal space directions so that V is related to the peak-intensity I and peak-width $FWHM_{h,k,l}$ in h, k or l-direction through $V_{a,c} = I\sqrt{8}\pi^{3/2}\sigma_h\sigma_k\sigma_l$ and $\sigma_{h,k,l} = FWHM_{h,k,l}/2\sqrt{2ln2}$. Reciprocal space maps give more accurate values of ϕ_c than θ-2θ-scanning, since all tilted domains can be measured, in contrast to scanning the Q$_{in,h}$=Q$_{in,k}$=0 line (the θ-2θ-line)

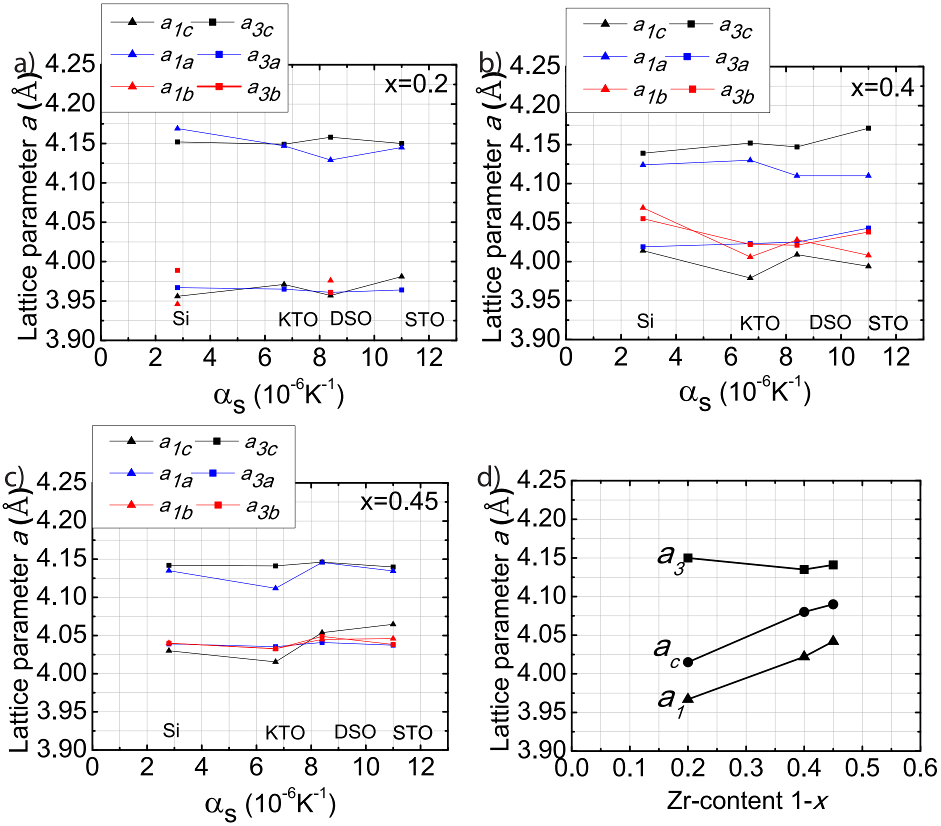

Figure 4.4: Lattice parameters a_1 and a_3 as function of substrate for all domains derived from (103) reciprocal space peak, for a) $x = 0.2$, b) $x = 0.4$, and c) $x = 0.45$. d) shows the average of lattice parameters a_1 and a_3 and the lattice parameter of the cubic phase at deposition temperature a_c, for each composition. Lines are guides to the eye.

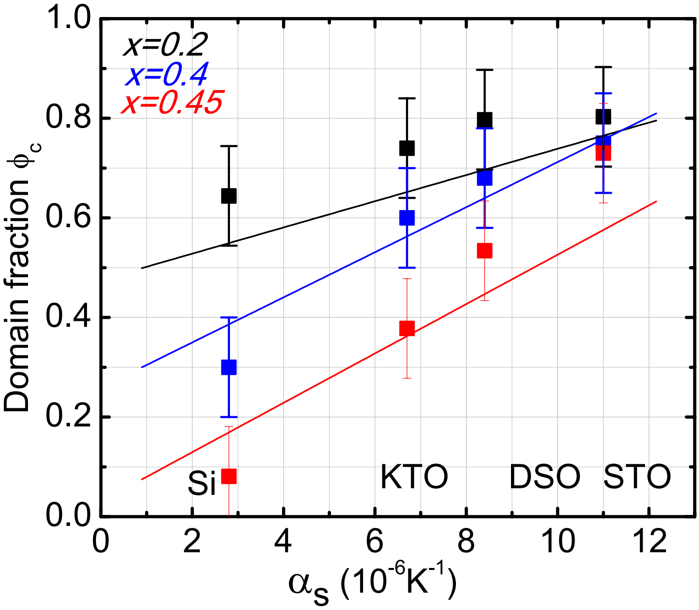

Figure 4.5: Domain fraction ϕ_c for $x = 0.2$, $x = 0.4$ and $x = 0.45$ as function of substrate and the model expectation

population. The temperature is used as a parameter to vary the strain. Temperature dependent reciprocal space maps on Si and STO have been measured and lattice parameters are determined for $x = 0.4$, as shown in fig. 4.6(a). As described in sec. 4.3.2, the lattice parameters a_1 and a_3 are sufficient to describe all domains. For clarity, the domain types and corresponding lattice parameters are illustrated again in fig. 4.6(c). The temperature evolution of the strain is analyzed with the aid of the concept of effective substrate, as proposed by Speck [8] and adapted by Janolin [18]. The effective lattice parameter a_s^* describes the evolution of the substrate after relaxation of the epitaxial strain. The curve is characterized by an equal thermal expansion coefficient of the effective substrate α_s^* and the real substrate α_s, and an equal in-plane lattice parameter at deposition temperature $a_s^*(\mathrm{T}_d)$ of the film and the effective substrate parameter [19]. The curve follows $a_s^* = a_c(1-\alpha_s(T-T_d))$, with a$_c$ is the in-plane lattice constant at deposition temperature. The lattice parameter at deposition temperature is needed for determination of the effective substrate lattice parameter. It is measured using temperature-dependent XRD and we obtain a_c=4.015Åfor $x = 0.2$, a_c=4.08Åfor $x = 0.4$ and a_c=4.09Åfor $x = 0.45$, as shown in fig. 4.6(d).

The temperature-dependent lattice parameters are compared to a$_s^*$. For $x = 0.4$, a_s^* lies in between a_1 and a_3 in the ferroelectric phase. The weighed average of the in-plane lattice parameters of all three domain types must be equal to the

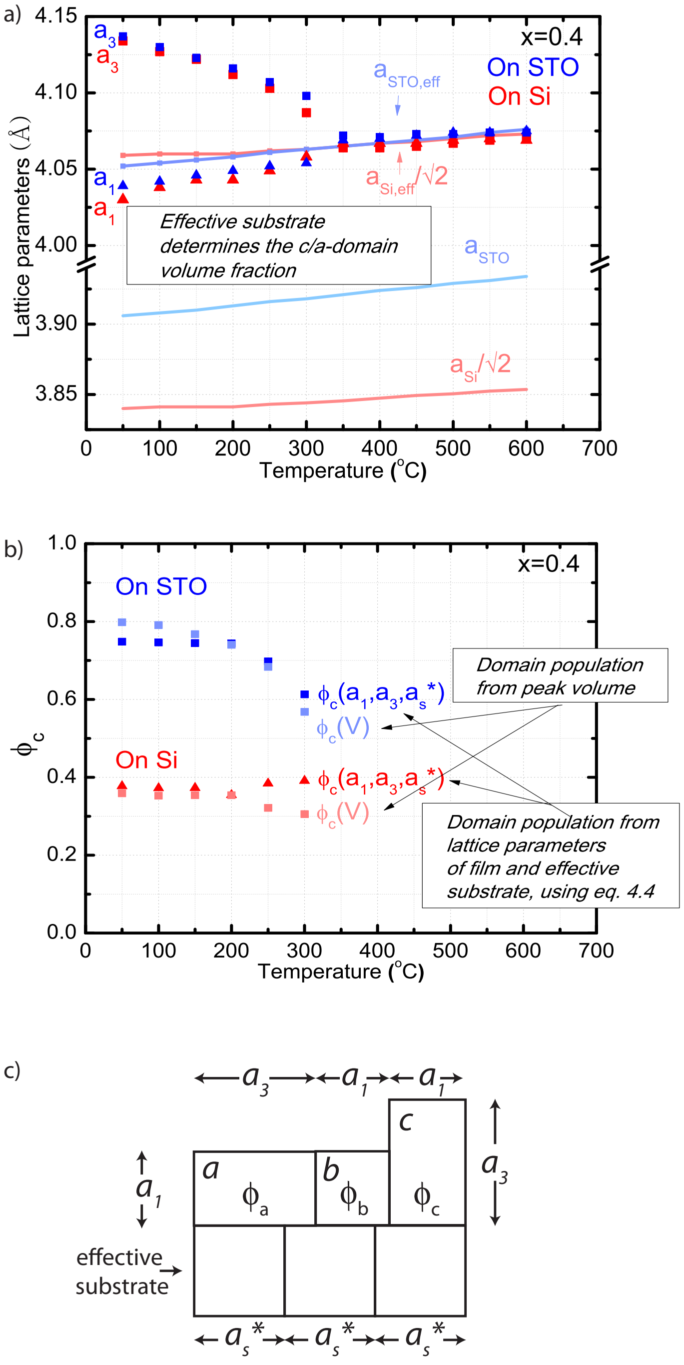

Figure 4.6: a) Temperature evolution of lattice parameters a_1 and a_3 on STO and Si for $x = 0.4$, measured from the PZT (203) reciprocal peak, b) Temperature evolution of the domain fraction ϕ_c, determined from lattice parameters (using eq. (4.4)), and the volume argument (see sec. 4.3.3), and c) Illustration of relation between the in-plane lattice parameters of all domains and the effective substrate a_s^*, as described by eq. (4.3) in sec. 4.3.4.

effective substrate lattice parameter a_s^*, as

$$a_s^* = \phi_c a_1 + \phi_b a_1 + \phi_a a_3 \tag{4.3}$$

Assuming ϕ_a=ϕ_b=$\frac{1-\phi_c}{2}$, the temperature dependence of the domain fraction ϕ_c can be calculated from the measured lattice parameters (see fig. 4.6(a)) and a_s^*

$$\phi_c(a_1, a_3, a_s^*, T) = \frac{a_3(T) + a_1(T) - 2a_s^*(T)}{a_3(T) - a_1(T)} \tag{4.4}$$

$\phi_c(a_1, a_3, a_s^*, T)$ is plotted in fig. 4.6(b). ϕ_c(V) [1] is plotted as well. The values obtained from these independent methods (XRD peak positions $\phi_c(a_1, a_3, a_s^*, T)$, and XRD intensity ϕ_c(V)), correspond very well. We find ϕ_c is larger on STO than on Si, for both ϕ_c(V) and ϕ_c(a$_1$, a$_3$, a$_s^*$). $\phi_c(\alpha_s)$ can be written as function of α_s, using $a_s^* = a_c(1 - \alpha_s \Delta T)$, with ΔT=T_d-T and a_c=4.075 Å, obtained from fig. 4.6. This expression is linear with α_s, which corresponds to the linear trend of ϕ_c on α_s in the experimental data at room temperature in fig. 4.5. The temperature dependent ϕ_c decreases toward ϕ_c=0.5 for STO, agreeing to previous studies [7].

4.3.5 Domain tilting

As explained in sec. 4.2.1, a tilting of tetragonal domains is expected, due to the crystallographic matching at the domain boundary. Fig. 4.2 shows the (h0l)-reciprocal space maps, in which several peaks are not centered on the line for which Q_{in} is 0. Since the tetragonal crystal is characterized by orthogonal crystal axes, this peak shift can be attributed to crystallographic tilting. Similar trends can be observed in the (hk0) scans in fig. 4.3.

The largest tilt is obtained for the *a* and *b*-domains. However, also the *c*-domains are tilted with a preferred orientation. The *c*-domain tilt is opposite to the tilt of *a*, and *b*-domains. A single preferred domain structure, throughout the sample is likely since discontinuities of the crystal coherency would need additional defect clusters. Therefore, either the domain structure $a_1/c_2/a_1$ or $a_2/c_1/a_2$ is present, as illustrated in fig. 4.1. Step edges on the surface of the substrate are likely to determine the direction of the tilt [20]. The obtained ω_c is largest for tensile strains on Si. Similarly, the *a* and *b* domains are tilted over ω_a and ω_b in two directions, to form the domains a_1, a_2, b_1, b_2.

The magnitude of the tilting angles ω_{a1} and ω_{a2} are derived from reciprocal space maps in fig. 4.2 and fig. 4.3 and shown in fig. 4.7(a). The values are in the range of 0-2°, in line with previous reported values. The ω values from the (hk0)-scans in fig. 4.3(a) correspond well to those obtained from the (h0l)-scans. Reciprocal space maps in the (hk0)-plane show that the *c*-domains are tilted in two in-plane directions simultaneously. The tilt angle of the *c*-domains ω_c is equal in both the *a* and *b* direction, as it should be in case of in-plane four-fold symmetry. The values are plotted in fig. 4.7(b). The tilt angles ω_{a1}=ω_{b2}=ω_{a2}=ω_{b1} is found, as expected. Figure 4.7(c) shows the measured value of $\Delta\omega$ for $x = 0.2$, 0.4 and 0.45, and $\Delta\omega_{max}$ as calculated from lattice parameters by eq. 4.1. A difference between $\Delta\omega$ and $\Delta\omega_{max}$ is found. The difference is larger for $x = 0.2$ to $x = 0.45$.

4.3.6 Model for the domain tilting

Next to the model for domain fraction, the domain tilting as function of substrate induced strain may be described by a model. Fig. 4.8(a) shows a schematical representation of the domain structure of the c/a-phase, where a-domains and c-domains participate in tilting and b-domains do not. The tilt of the b-domains is in the plane perpendicular to the considered (h0l)-plane. The height h of the tilted domain can be described in terms of the domain lengths L_c, L_a and the angles of the domains ω_c and ω_a as $h = L_c \tan\omega_c = L_a \tan\omega_a$. Since $\tan\omega \approx \omega$ for small ω, one has $\omega_c L_c = \omega_a L_a$. The relation between the domain fractions of all domains is ϕ_a=ϕ_b=$\frac{1-\phi_c}{2}$. Assuming that the ratio of the domain length is proportional to the ratio of domain fractions L_a/L_c=ϕ_a/ϕ_c, one obtains

$$\omega_a = \omega_c(\frac{2\phi_c}{1-\phi_c}) \tag{4.5}$$

$\Delta\omega$ is the tilt angle between the a and c-domain, and depends on the Zr-content only, as seen in fig. 4.7. Therefore one can write

$$\omega_c(\phi_c) = \Delta\omega(\frac{1+\phi_c}{1-\phi_c}) \tag{4.6}$$

$$\omega_a(\phi_c) = \Delta\omega(\frac{2\phi_c}{1+\phi_c}) \tag{4.7}$$

The results of the model described by eq. (4.6) and (4.7) is shown in fig. 4.8(b). Used values from fig. 4.7(c) are $\Delta\omega$=2.25° for $x = 0.4$, $\Delta\omega$=1.25° for $x = 0.4$ and $\Delta\omega$=0.9° for $x = 0.45$.

The measured magnitude of ϕ_c for $x = 0.2$, $x = 0.4$ and $x = 0.45$ on all substrates is shown in the top of fig. 4.8(a). Tilt angles are plotted as a function of ϕ_c in figure 4.8(b), for all studied compositions. ω_c shows a negative trend and ω_a shows a positive trend on ϕ_c. The fit of the model to the experimental data for the ω_c and ω_a is good, within the accuracy of measurement of ω and ϕ_c.

4.3.7 Domain structure by Scanning Probe Microscopy

In fig. 4.9, the atomic force microscope (AFM) is used to study the domain tilting through an analysis of the surface facets. The domain fractions are studied by piezo force microscopy (PFM). Here, the effect of composition is studied using exclusively STO substrates. Fig. 4.9(a)-(c) shows the gradient of the AFM surface topography in the direction of the topography. The white line indicates the location of the cross-section of the topography taken, shown in fig. 4.9(d)-(f).

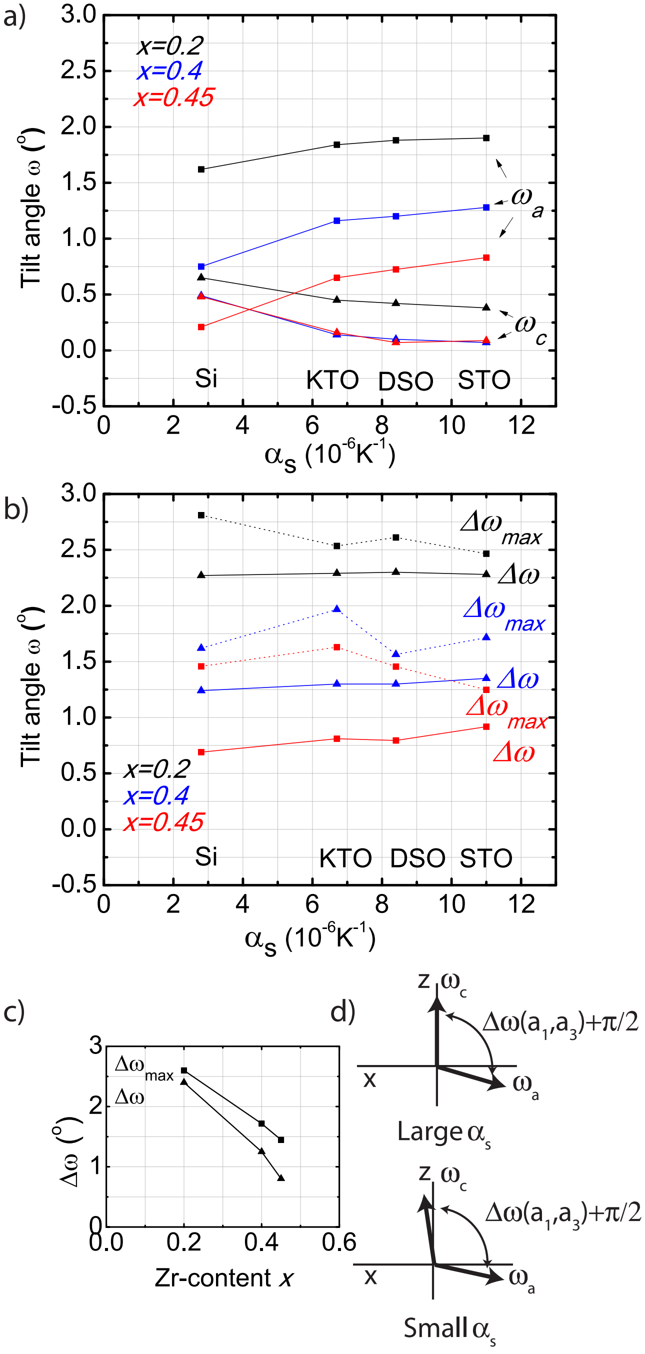

Figure 4.7: a) Tilt angle of c-domains ω_c and a-domains ω_a as function of substrate. b) Tilt angle between a and c-domains $\Delta\omega_{max}$ (eq. (4.1)) and sum of directly measured $\Delta\omega=\omega_a+\omega_c$ angles (eq. (4.2)). c) Averaged values of $\Delta\omega_{max}$ and $\Delta\omega$ as function of Zr-content. d) Schematical image of tilt angle ω_c of a c-domain and ω_a of an a-domain, and $\Delta\omega(a_1, a_3) + \pi/2$, for large and small α_s ($\pi/2$ added to simplify image). Lines are guides to the eye.

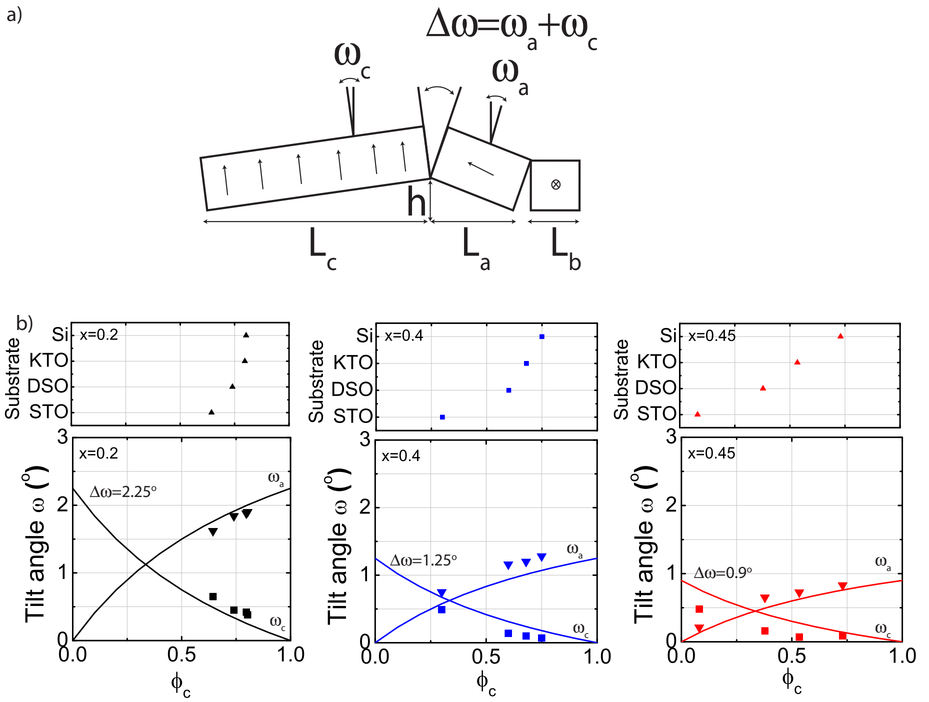

Figure 4.8: a) Schematical representation of the c/a-domain structure showing the domain tilting angles ω_a, ω_c, $\Delta\omega$, the relationships between tilt angles, tilt height h and length of the a, b and c-domains, respectively L_a, L_b and L_c b) Tilt angles ω_c and ω_a as function of used substrate and c domain fraction ϕ_c from experiments and theory

For $x = 0.2$ a sawtooth-like shape is found, whereas for $x = 0.4$ and $x = 0.45$ the curve is more disordered and has rounded peaks. Finally, (g)-(i) show the distributions of inclination angle in horizontal direction for the three compositions. Gaussian curves are fitted to the measured profile in order to improve the determination of the exact tilting angles. The blue curve corresponds to the a-domain, the red curve to the c-domain and the purple curve to the sum of both gaussians. For $x = 0.2$, clearly two inclination angles are found with opposite sign.The high peak is assigned to the c-domains and the low peak the a-domains, since ϕ_c=0.8, according to fig. 4.5(a). The peaks are separated by $\Delta\omega$=2.15°, which agrees well with $\Delta\omega$=2.25° from XRD.

For $x = 0.4$, the slope distributions of a and c domains become closer. A similar ratio of distribution between c and a-domains is present for this composition, which agrees to ϕ_c=0.8 for this film. $\Delta\omega$=1.4° is obtained by AFM, which corresponding to $\Delta\omega$=1.25° by XRD.

For $x = 0.45$, $\Delta\omega$=0.7° is found by AFM and $\Delta\omega$=0.9° by XRD. The surface facets are more rounded with respect to x =0.2 and 0.4, however on macroscopic scale the characteristic tilting is still correlated to the crystals principle axes. No relation to ϕ_c is discernible for this composition. Unfortunately it is not possible to find individual ω_a and ω_c values with respect to the substrate crystal. This would need the substrate surface to be measured. It should be noted that the tilt that is measured by AFM is the tilt of the surface, not measured throughout the film thickness. It is assumed that the tilting is constant for thickness larger than the critical thickness for epitaxial strain relaxation, as was also found by ref. [21].

Figure 4.9 (j)-(o) shows PFM data simultaneously obtained with the surface topography. In (j)-(l) the out-of-plane amplitude and in (m)-(o) the in-plane amplitude is shown. It can be seen that the domain-wall are correlated to the crystal for x =0.2 and 0.4. For x =0.45 the domain-walls are less determined by the crystal principal axes. This might indicate an increased effect of the depolarization energy on the domain dynamics. The domain fraction ϕ_c by PFM is found to be roughly 0.8 for all compositions. This value agrees to the earlier results by XRD.

4.4 Discussion

The results give rise to a number of interesting observations.

The temperature dependent study indicates that the films are largely relaxed of epitaxial strain, since the lattice parameters at deposition temperature are equal on all substrates at a certain composition. Due to the fabrication at high temperature by pulsed laser deposition, the films are subject to thermal strain. This strain is not relaxed by creation of misfit dislocations. In contrast to a number of alternative fabrication methods such as chemical solution deposition, the growth temperature is exact and therefore the thermal history of the sample at

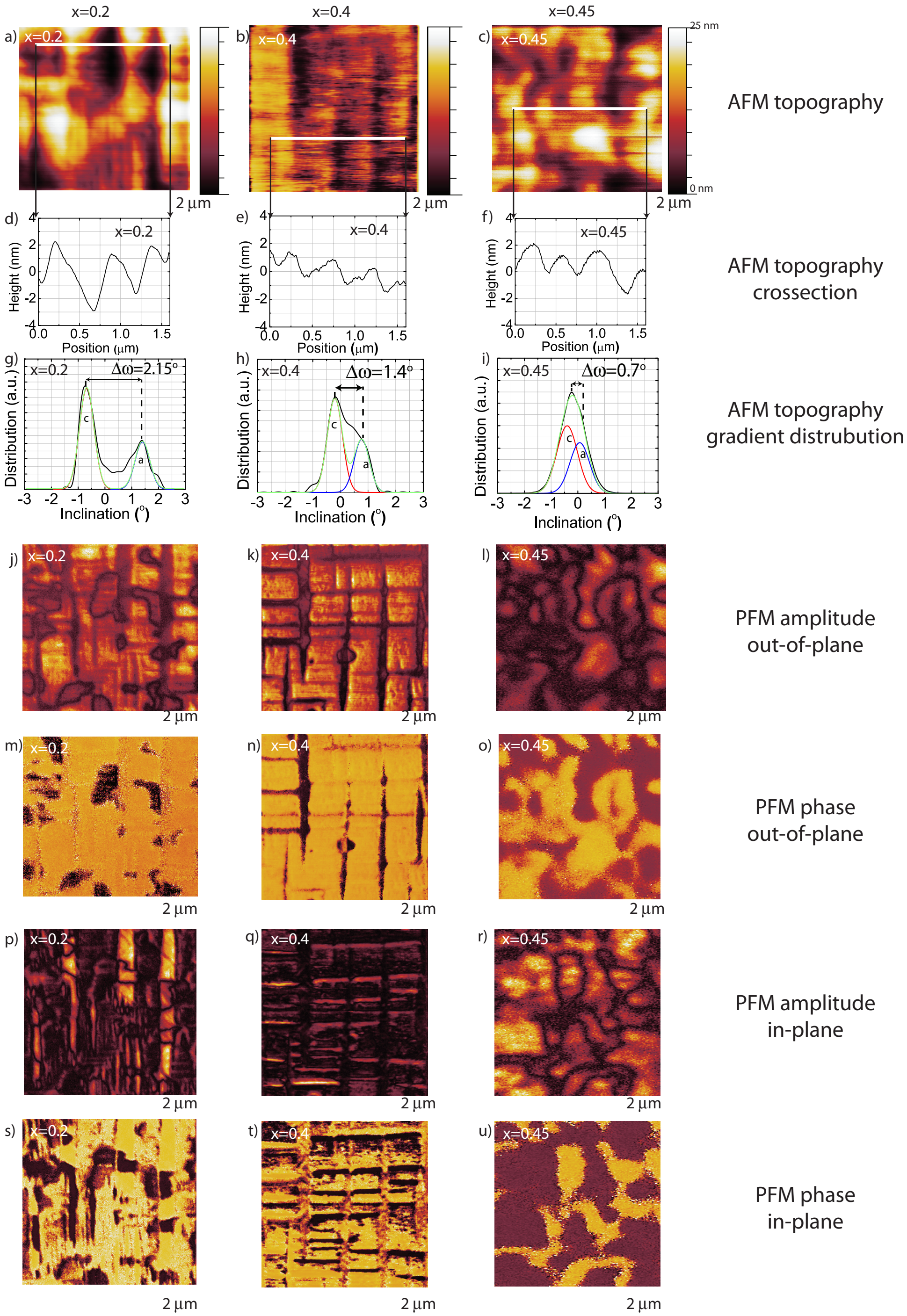

Figure 4.9: Domain tilting as function of composition by AFM (2x2 μm^2), for STO substrates. (a)-(c) inclination of AFM topography, in horizontal direction, (d)-(f) cross-section of the topography, at position indicated in (a)-(c), (g)-(i) distribution of inclination angles in x-direction (j)-(l) PFM out-of-plane amplitude signal and (m)-(o) PFM out-of-plane phase signal, (j)-(l) PFM in-plane amplitude signal and (m)-(o) PFM in-plane phase signal

room temperature is accurately known. The domain structure can be predicted directly from the thermal expansion coefficient of the substrate α_s. The domain fraction can be calculated from the lattice parameters and the effective substrate lattice parameter, using eq. (4.4). A linear relation between ϕ_c and α_s is expected theoretically. The experiments confirm this linear relation. An important ingredient for this simple model is the fact that the spontaneous lattice strain is independent of the magnitude of the substrate strain. This spontaneous strain is often interpreted as self-strain, since it is an intrinsic strain that is generated spontaneously by a chemical force when cooling through the ferroelectric phase transition. The unit-cell is strained according to the spontaneous strain, and the substrate-induced strain controls the domain fraction. Another principle that is used in the model is the full stress relaxation that is obtained by the formation of domains and adjustment of the domain fraction. This observation is supported by literature for these thick ferroelectric films [7, 15, 22].

The consideration of the domain structure in this study differs from previous studies, in that the b-domains are incorporated in the models. The addition of the b-domains requires the replacement by eq. 4.4 for $\phi_c = \frac{a_s^* - a_3}{a_1 - a_3}$, as presented by ref. [19] literature studies [23] [10]. The obtained c-domain fraction is typically lower than for the case where no b-domains are incorporated.

For higher Zr-content, ϕ_c is more dependent on the substrate induced strain. For a lower magnitude of the lattice strain, more domains switch over 90° at an equal amount of substrate induced strain. The polarization does not change, compared to the domain fraction, since the spontaneous polarization is coupled to the spontaneous strain (described by the electrostrictive coupling $x_3 = Q_{11} P_3$). Therefore the polarization dependence of the substrate induced strain does not depend on the composition, in comparison to the domain fraction, as will be described in chapter 6.

For x =0.45, ϕ_c approaches 0, meaning nearly all domains are oriented in-plane. In the framework of polydomain thermodynamic models, as discussed in sec. 2.2.5, the film is close to transformation into the a_1/a_2 phase. The tilt of the a-domains for x =0.45 on Si is small, another indication that the film is largely in the a_1/a_2 phase. Using the Si substrate is able introduce a large tensile thermal strain on the film. For increasing Zr-content, the effect on the domain fraction is becoming larger. It is expected that this trend continues for Zr-content larger than $x = 0.45$, toward the MPB. For such films under tensile strain near the anomaly of polydomain c/a to a_1/a_2 phase, an increase of dielectric and piezoelectric properties are predicted [24, 25]. Next to the intrinsic properties, domain-wall movement is a reason for the increased properties near a polarization instability [10, 23]. The functional properties will be studied in chapter 6.

The tilting of domains is a consequence of the crystallographic matching of adjacent c and a domains. $\Delta\omega$ is therefore proportional to the arctan of the spontaneous lattice strain (eq. 4.1) and independent of strain. However, the individual domain tilting depends on the strain. If the strain is compressive, the dominant part of the film is c-domain, the c-domains are parallel to the principal z-axis and the a-domains are tilted with respect to the substrate. If the strain is tensile, the situation is reversed, the a-domains are parallel to the substrate and the c-domains are tilted. It should be noted that tilting of the c-domains typically has not been taken into account, since most reports used compressively strained films with large c-domain fractions. This study shows that both domains should be considered in study the tilting mechanism, especially for tensile strained films.

The measured $\Delta\omega$ is actually lower than the theoretical $\Delta\omega_{max}$, see sec. 4.4. This difference is increasing with Zr-content. It can be explained by the observation that the theoretical value is derived for a material without stiffness [12]. For a crystal without stiffness (Young's modulus E=0, compliance $s \to \infty$), the DW-wall is infinitely small. The domain-wall has a finite width for bending of the crystal. The values of the elastic compliance are in-line with this arguments, since it shows a slight increase toward the MPB [26] [9]. Furthermore, the elastic shear modulus is thought to influence the mechanism of domain-wall. This value depends more on the composition than the linear elastic modulus and can be the reason for the difference between measured and theoretical values. Another possible explanation can be the fact that at certain locations in the film the b-domains border to the c-domains. In the used system, the b-domain is tilted in perpendicular direction to the tilting-plane of the a and c domains. Since the$a$ and c-domains need to be coherent with the b-domains, the tilting of the a and c-domains is limited by the b-domains. For x=0.45, more b-domains are present and the difference between $\Delta\omega$ and $\Delta\omega_{max}$ is larger. In order to judge whether the effect of the domain-wall width and the b-domains should be taken into account, advanced electron microscopy (STEM) could clarify the mechanism in detail [14, 27].

4.5 Conclusions

In conclusion, the relation between domain fraction, domain inclination and substrate-induced strain in epitaxial $Pb(Zr_x,Ti_{1-x})O_3$ (PZT) films is studied. Films $x = 0.2$, 0.4 and 0.45 are in the tetragonal c/a-phase, for which domain fraction depends strongly on strain while the lattice parameters remain constant. Next to the tilted a and b-domains, tilted c-domains are observed with tilt in the a and b-directions and strain dependent tilt angle. A model was derived for the domain tilting as function of domain fraction and strain and shows a good fit to the experiments. On silicon the c-domain fractions are low, therefore the film is approaching the a_1/a_2-phase for which high dielectric and piezoelectric properties are predicted.

4.6 References

[1] J. Reiner, A. Kolpak, Y. Segal, and K. Garrity. Crystalline oxides on silicon. *Adv. Mat.*, XX:1–20, 2010.

[2] P. Muralt. Recent progress in materials issues for piezoelectric mems. *J. Am. Ceram. Soc.*, 91(5):1385–1396, 2008.

[3] M. Dekkers, M. Nguyen, R. Steenwelle, P. Te Riele, D. Blank, and G. Rijnders. Ferroelectric properties of epitaxial $Pb(Zr, Ti)O_3$ thin films on silicon by control of crystal orientation. *Appl. Phys. Lett.*, 95:012902, 2009.

[4] M. Warusawithana, C. Cen, C. Sleasman, J. Woicik, Y. Li, L. Kourkoutis, J. Klug, H. Li, M. Ryan, L. Wang, M. Bedzyk, D. Muller, L. Chen, J. Levy, and D. Schlom. A ferroelectric oxide made directly on silicon. *Science*, 324(5925):367–370, Apr 2009.

[5] G. Shirane, K. Suzuki, and A. Takeda. Phase transitions in solid solutions of $PbZrO_3$ and $PbTiO_3$ (ii) x-ray study. *J. Phys. Soc. Japan*, 7:12, 1952.

[6] N. Pertsev and A. Zembilgotov. Domain populations in epitaxial ferroelectric thin films: Theoretical calculations and comparison with experiment. *J. Appl. Phys.*, 80(11):6401–6406, 1996.

[7] B. Kwak, A. Erbil, J. Budai, M. Chisholm, L. Boatner, and B. Wilkens. Domain formation and strain relaxation in epitaxial ferroelectric heterostructures. *Phys. Rev. B*, 49(21):14865, 1994.

[8] J. Speck and W. Pompe. Domain configurations due to multiple misfit relaxation mechanisms in epitaxial ferroelectric thin films. i. theory. *J. Appl. Phys.*, 76:466, 1994.

[9] N. Pertsev, V. Kukhar, H. Kohlstedt, and R. Waser. Phase diagrams and physical properties of single-domain epitaxial $Pb(Zr_{1-x}, Ti_x)O_3$ thin films. *Phys. Rev. B*, 67(5):054107, 2003.

[10] V. Kukhar, N. Pertsev, H. Kohlstedt, and R. Waser. Polarization states of polydomain epitaxial $Pb(Zr_{1-x}, Ti_x)O_3$ thin films and their dielectric properties. *Phys. Rev. B.*, 73(21):214103, 2006.

[11] A. Tagantsev, N. Pertsev, P. Muralt, and N. Setter. Strain–induced diffuse dielectric anomaly and critical point in perovskite ferroelectric thin films. *Phys. Rev. B.*, 65(1):012104, 2001.

[12] C. Kittel. Thickness of domain walls in ferroelectric and ferroelastic crystals. *Sol. State. Comm.*, 10(1):119–121, 1972.

[13] A. Vlooswijk, B. Noheda, G. Catalan, A. Janssens, B. Barcones, G. Rijnders, D. Blank, S. Venkatesan, B. Kooi, and J. De Hosson. Smallest 90 domains in epitaxial ferroelectric films. *Appl. Phys. Lett.*, 91:112901, 2007.

[14] G. Catalan, A. Lubk, A. Vlooswijk, E. Snoeck, C. Magen, A. Janssens, G. Rispens, G. Rijnders, D.H.A. Blank, and B. Noheda. Flexoelectric rotation of polarization in ferroelectric thin films. *Nat. Mater.*, 10:963–967, 2011.

[15] W. Pompe, X. Gong, Z. Suo, and J. Speck. Elastic energy release due to domain formation in the strained epitaxy of ferroelectric and ferroelastic films. *J Appl Phys*, 74:6012, 1993.

[16] C. Foster, G. Bai, R. Csencsits, and J. Vetrone. Single-crystal $Pb(Zr_x, Ti_{1-x})O_3$ thin films prepared by metal-organic chemical vapor deposition: Systematic compositional variation of electronic and optical properties. *J Appl Phys*, 81(5):2349–2357, 1997.

[17] K. Lee, J. Choi, J. Lee, and S. Baik. Domain formation in epitaxial $Pb(Zr, Ti)O_3$ thin films. *J Appl Phys*, 90(8):4095–4102, 2001.

[18] P. Janolin. Strain on ferroelectric thin films. *J Mater Sci*, 44:5025, 2009.

[19] C. Foster, W. Pompe, A. Daykin, and J. Speck. Relative coherency strain and phase transformation history in epitaxial ferroelectric thin films. *J Appl Phys*, 79:1405, 1996.

[20] J. Dekkers, G. Rijnders, S. Harkema, H. Smilde, H. Hilgenkamp, H. Rogalla, and D. Blank. Monocrystalline $YBaCuO$ thin films on vicinal $SrTiO_3$ (001) substrates. *Appl. Phys. Lett.*, 83:5199, 2003.

[21] H. Nakaki, Y. Kim, S. Yokoyama, R. Ikariyama, H. Funakubo, K. Nishida, K. Saito, H. Morioka, O. Sakata, H. Han, and S. Baik. Strain-relaxed structure in (001)/(100)-oriented epitaxial $Pb(Zr, Ti)O_3$ films grown on (100) $SrTiO_3$ substrates by metal organic chemical vapor deposition. *J. Appl. Phys.*, 105(1):014107, 2009.

[22] A. Roytburd. Thermodynamics of polydomain heterostructures. i. effect of macrostresses. *J. Appl. Phys.*, 83:228, 1998.

[23] V. Kukhar, N. Pertsev, and R. Waser. Thermodynamic theory of epitaxial ferroelectric thin films with dense domain structures. *Phys. Rev. B.*, 64(21):214103, 2001.

[24] G. Catalan, A. Janssens, G. Rispens, S. Csiszar, O. Seeck, G. Rijnders, D. Blank, and B. Noheda. Polar domains in lead titanate films under tensile strain. *Phys. Rev. Lett.*, 96(12):127602, 2006.

[25] H. Li, A. Roytburd, S. Alpay, T. Tran, L. Salamanca-Riba, and R. Ramesh. Dependence of dielectric properties on internal stresses in epitaxial barium strontium titanate thin films. *Appl. Phys. Lett*, 78:2354, 2001.

[26] J. Ouyang and A. Roytburd. Theoretical modeling of coexisting tetragonal and rhombohedral heterophase polydomain structures in lead zirconate titanate ferroelectric films near the morphotropic phase boundary. *Acta Mater.*, 54(20):5565–5572, 2006.

[27] W. Rao and Y. Wang. Domain wall broadening mechanism for domain size effect of enhanced piezoelectricity in crystallographically engineered ferroelectric single crystals. *Appl. Phys. Lett.*, 90(4):041915–041915–3, 2007.

Chapter 5

Crystallographic properties of Pb(Zr,Ti)O_3 thin films near the morphotropic phase boundary

Abstract

The domain structure and misfit strain dependence is investigated for Pb(Zr_x,Ti_{1-x})O_3 thin films near the morphotropic phase boundary between $x = 0.48$ and $x = 0.52$. The material is found to be tetragonal with nanoscale domains with low domain-wall energy density, while a homogeneous quasi-cubic phase is measured. The adaptive phase theory is adjusted for thin films with the addition of a typical a, b and c domain structure. The general invariance condition that follows from this theory, is fulfilled at all temperatures. The special invariance condition is not satisfied, due to the finite thermal substrate induced strain. The observed phase is equivalent to the monoclinic r-phase that is predicted by phenomenological models.

5.1 Introduction

The high piezoelectric properties in bulk Pb(Zr_x,Ti_{1-x})O_3 (PZT) are related to the presence of the morphotropic phase boundary (MPB), which at room temperature is located in a composition region of $x = 0.52$ - 0.54. In PZT thin films, the crystallographic and functional properties of this compositional region have remained underexposed, in comparison to the polydomain tetragonal phase. Reasons for this are that the crystallographic features are small and difficult to measure, and the properties are sensitive to temperature, strain, composition and electric field. For bulk, many attempts to explain the crystallography and properties near the morphotropic phase boundary have been presented, for example the coexistence of rhombohedral domains and tetragonal domains [1–4], presence of a monoclinic crystal phase [5] or the formation of nanoscale domains with low-domain wall energy [6, 7].

The presence of a nanoscale domain structure that forms an adaptive phase has been demonstrated in the relaxor materials PMN-PT and PZN-PT [6, 8–11]. This adaptive phase is characterized by a domain structure consisting of twin-domains that adjusts the domain fraction to relax the stress in the film. The domain fraction can easily adjust under externally applied strain or electric field due to a low domain-wall energy [12]. This is caused by the decrease of the spontaneous tetragonal strain toward the morphotropic phase boundary (see ch. 4), that diminishes the energy barrier for the transformation of a c-domain into an a-domain or vice versa [13]. For a 90° domain-wall, this domain-wall energy is estimated as $\gamma = \sqrt{8Ca^2\Delta G}$, with ΔG the phenomenological free energy potential, a the lattice parameter and C the elastic stiffness [14, 15]. The domain-wall energy decreases toward the morphotropic phase boundary according to $\gamma \sim \sqrt{x - x_{MPB}}$, where x is the composition parameter and x_{MPB} the composition at the morphotropic phase boundary [16]. Consequently, curved domain-walls arise [17] [18], polarization gradients and strain gradients extend outside the theoretical domain-wall region [19–21], and a spatially modulated domain structure, an incommensurate phase, may form [22, 23]. The ferroelectric r-phase that was predicted by phenomenological models [24] shows similarity to these observations. Another indication of domain-wall broadening [25] is the surface topography in the c/a-phase that follows a sawtooth shape for low Zr-content and is wavy for high Zr-content, as found in sec. 4.3.7.

The lack of reports of nanoscale domains in ferroelectric films creates an opportunity to explore this subject. In this case, the substrate induced strain can be used as a parameter to study the mechanism of self adjusting domain fraction [26, 27]. This mechanism is expected to show analogies to the effects of the substrate induced strain on the c/a-phase, as was studied in ch. 4. An additional advantage of clamping of the substrate is that it fixes a certain state of the domain structure, and therefore improves imaging reproducibility.

In this chapter, the crystallographic properties of PZT thin films near the morphotropic phase boundary (MPB) are studied. In order to compare these films to the c/a-phase, first PZT films with $x = 0.2$ and 0.5 are fabricated on STO. The domain structure is studied using x-ray diffraction with reciprocal space maps, piezo force microscopy (PFM) and transmission electron microscopy (TEM). The x-ray diffraction interference effect is explained using PZT films at the tetragonal side of the MPB, with $x = 0.2$, 0.45, 0.48 and 0.5. The misfit strain effect on PZT films with $x = 0.5$ is studied using substrates STO, DSO, KTO and Si substrates. The adaptive phase theory is adjusted for thin films, by adding a thermal strain

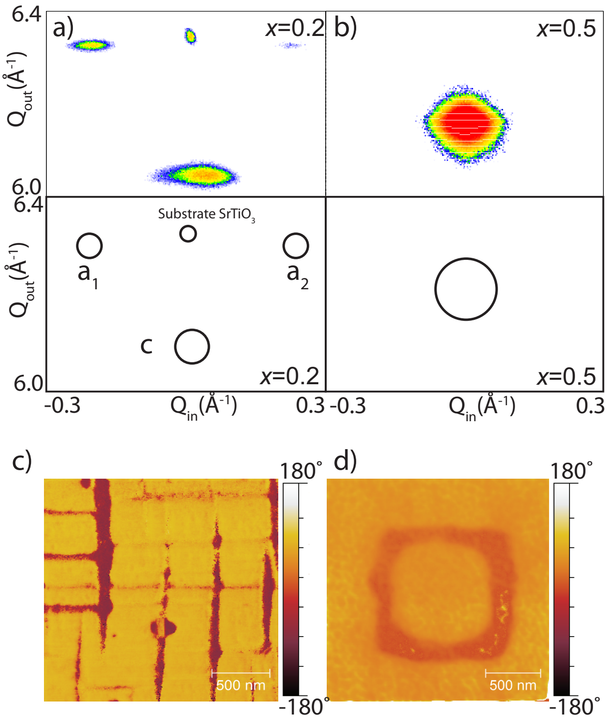

Figure 5.1: Reciprocal space maps as a function of PZT films with a) $x = 0.2$ and b) 0.5 on STO, accompanied by the schematic illustration of the RSM with domain types assigned to the peaks, and PFM-phase images of PZT films on STO with c) $x = 0.2$ and d) 0.5. The PFM image size is 2x2μm^2.

and using a a, b and c domain structure. The general invariance condition that is characteristic for the adaptive phase is tested for the films.

5.2 Domain structure of MPB compositions

In this section, the domain structure of a PZT film in the tetragonal phase with $x = 0.2$ is compared to PZT film near the MPB with $x = 0.5$. In fig. 5.1, the domain structure is shown using reciprocal space mapping ((a) and (b)) and piezo force microscopy ((c) and (d)). Differences in domain structure between the tetragonal film at $x = 0.2$ and the film near the MPB at $x = 0.5$ are visible. For $x = 0.2$, both RSM and PFM show a typical c/a-domain structure with separate a,b and c-domains. The domain size is estimated to be between 50 nm and 500 nm. For $x = 0.5$ no clear a,b or c-domains can be seen. The RSM shows a single peak with broader than typical peaks of PZT. In the PFM image, no domains could be observed. It should be noted that to create contrast, the material was locally polarized in a square of 1 μm with a positive voltage of 10 V and a square

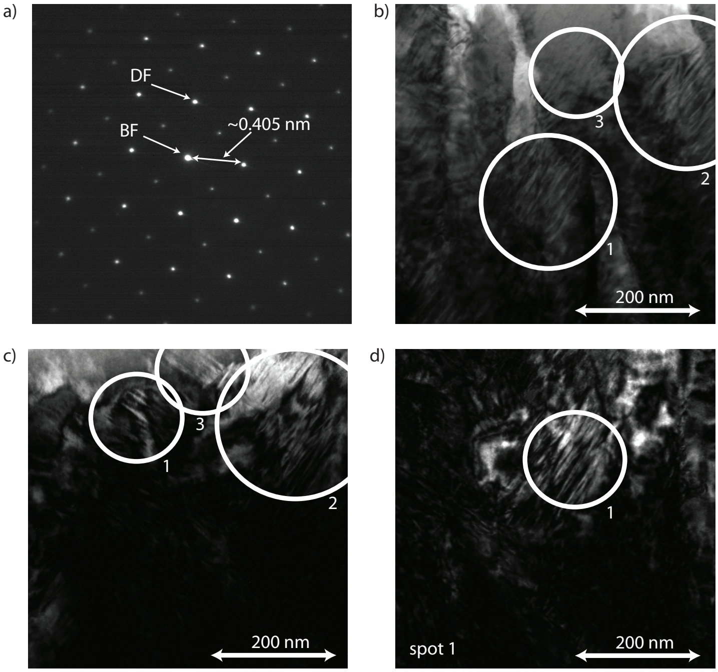

Figure 5.2: a) Typical selected area electron diffraction (SAED) image, b) HRTEM image, c) BF-TEM image and d) DF-TEM image of PZT with $x = 0.5$. The substrate - film interface is parallel to the horizontal direction in the image and is located outside the image area.

of 500 nm with a negative voltage of -10 V. The domain boundaries are curved and in case a tetragonal material is assumed for which the domain-walls need to be oriented parallel to the principal crystallographic directions, the domain size needs to be smaller than the PFM tip-size, which is 20 nm for $x = 0.5$.

Figure 5.2(a) shows the selected area electron diffractogram (SAED) of a PZT film with $x = 0.5$. A cubic lattice is present from the four-fold symmetry of the pattern. The lattice parameter is determined to be approximately 4.05 Å, from the distance of reciprocal spots. The accuracy of determining structural parameters using this method is low [8, 17]. The spots which are used in the BF-TEM and DF-TEM images are indicated. BF imaging uses the central diffraction spot, the DF imaging uses the spot directly above the bright central spot. Fig. 5.2(b) shows a cross-sectional HRTEM image. Several regions are highlighted using circles 1, 2 and 3. Long contrast stripes are present in circle 1 and 2. A darker region of the image faintly shows similar stripes in circle 3. The width of the stripes ranges from approximately 5 nm to 20 nm. In comparison, HRTEM images on the c/a-phase, as shown in for example ref. [28], show domains of a typical size larger than 50 nanometer with long straight domain-walls under 45° with respect to the substrate surface. Fig. 5.2(c) shows a obtained BF-TEM image. In circle 1 and 3, stripe domains under 45° with the substrate surface are observed. The length of the stripe domains varies from 5 nm to 50 nm. In circle 2 a large area with stripe domains with an 90° angle with the stripe domains of circle 1 and 3 can be seen. The length of the stripe domains can be 200 nm. Fig. 5.2(d) shows a DF-TEM image using reciprocal spot 1, see fig. 5.2(a). The contrast is improved with respect to fig. 5.2(a) and (b), and the intensity is more homogeneous. Again, stripe domains are oriented 45° with the film surface normal.

In general, domains with length between 5 nm and 200 nm and width between 5 nm and 20 nm are found. The domains-walls are curved. These domains are found in substantial amounts throughout the film. These domains show a preferred orientation of 45° degrees with respect to the principal lattice axes, the (101) direction. The morphology agrees to TEM studies on bulk PZT and PMN-PT. These observations fit to the prediction of nanoscale domains in an adaptive phase. No conclusions on the domain-wall width can be made, the use of higher resolution imaging is suggested to obtain improved information.

5.2.1 X-ray diffraction interference effect on nanoscale domains

In this section, the homogeneous single domain phase with nanoscale domain structure, that was observed in the previous section, is explained by an x-ray diffraction interference effect of the nanoscale domains. If domains are smaller than the coherence length of the diffraction radiation, interference between the different crystal variants in the lattice will occur. In that case, the relative phase angles of the scattered waves must be considered [29]. The Bragg peaks at the position of the individual crystal variants will disappear and a new reflection occurs, at the position where constructive interference of the scattered waves of the individual domains takes place. The effect is explained through analysis of the structure factor of the twin-related crystal variants, described by Wang [30]. The mechanism can occur in tetragonal nanotwin superlattices and rhombohedral nanotwin superlattices [29].

Figure 5.3 shows the diffraction vectors for large and nanoscale domains. For large domains, two separate diffraction spots are obtained. For nanoscale domains, interference between the diffracted beams of both domain variants generates a single beam $\vec{k}^{(s)}$ in between the disappeared spots. The location of the $\vec{k}^{(s)}$ depends on the domain fraction ϕ_c. The Bragg splitting vectors due to twinning deformation is

$$\Delta\vec{K} = \vec{K}_1 - \vec{K}_2 = -(2\epsilon\vec{s}\cdot\vec{K}^{(1)})\vec{\tau}, \tag{5.1}$$

where $\vec{\tau}$ and $\vec{s}$ are unit vectors normal to the twin plane and along the twinning shear direction, respectively, $\epsilon{=}(c_t - a_t)/a_t$ is the magnitude of twinning strain. The adaptive Bragg reflection is described by

$$k^{(s)} = \phi_c\Delta\vec{K} + \vec{K}^{(2)} \tag{5.2}$$

with $K^{(2)}$ is one of the fundamental Bragg reflections and ϕ_c the domain fraction.

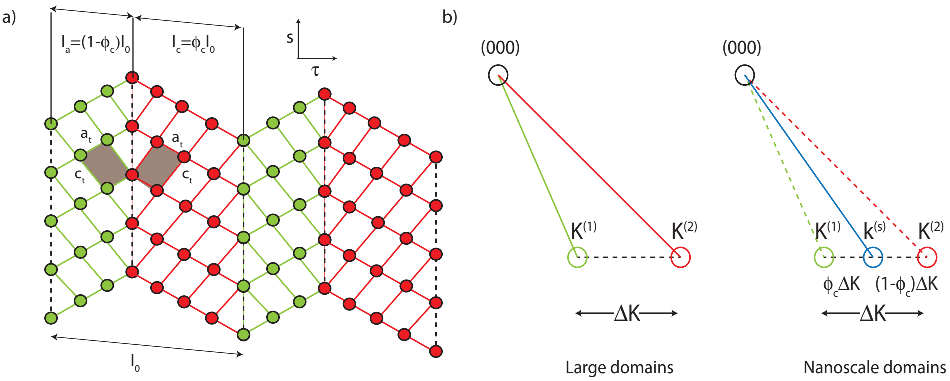

Figure 5.3: a) Schematical image of a nanoscale domain structure, b) Schematical image of the interference effect in diffraction on domains in PZT the situation with coarse domains with diffraction vectors $\vec{K}$ and $\vec{K}$ for each twin variants, and c) interference effect for nanoscale domains with diffraction vector k^s for the constructively interfered beam, where this Bragg reflection moves between vanished fundamental peaks $\vec{K}^{(1)}$ and $\vec{K}^{(2)}$ of the two domain variants in response to a change in ϕ_c.

The condition for appearance of the adaptive phase interference effect is derived. $l_0 = l_1 + l_2$ is the thickness of the twinned bilayer, l_1 is the thickness of domain plate 1 and l_2 the thickness of domain plate 2, the peak-half width of both domains being $2\pi/l_1$ and $2\pi/l_2$ using Scherrers formula [31], and the distance between the peaks is $\Delta K = 2\epsilon|\vec{s}\cdot\vec{K}|$, is

$$2\epsilon|\vec{s}\cdot\vec{K}| < 2\pi\left(\frac{1}{l_1}+\frac{1}{l_2}\right) = \frac{2\pi}{l_0}\left(\frac{1}{\phi_c}+\frac{1}{1-\phi_c}\right), \tag{5.3}$$

with l_0 is the domain layer thickness. The threshold domain size (in case of $\epsilon << 1$ and $\phi_c = 0.5$) is

$$l_0 < \sqrt{2}a_t/(2\epsilon(h+l)) \tag{5.4}$$

where a_t is the lattice parameter, the lattice strain $\epsilon \sim 10^{-2}$, $(h+k) \sim 4$ if using the (004) reciprocal spot. The domains will be resolvable by x-ray diffraction if $l_0 >> 25a_t$, roughly 10 nm.

Figure 5.4 shows schematically the RSMs of materials with large domains, nanoscale domains or a mix of both. It can be seen that for large domains, individual domains can be imaged directly, such as the *a* and *b*-domains (green) and the *c*-domains (red). The peak for the adaptive phase with nanoscale domains (blue) will be detected in between the disappeared peaks of the coarse domains. The colors relate to fig. 5.3(b). A single peak is observed in fig. 5.4(b) and (e) for $x = 0.48$ and in fig. 5.4(c) and (f) for $x = 0.5$, which is explained by the interference mechanism. The RSM indicate a polydomain tetragonal *c*/*a*-phase for $x = 0.45$, and the homogeneous single domain phase for $x = 0.48$ and 0.5. It is concluded that the observation of a single peak in the PZT films is consistent with a miniaturization of domains to the nanoscale.

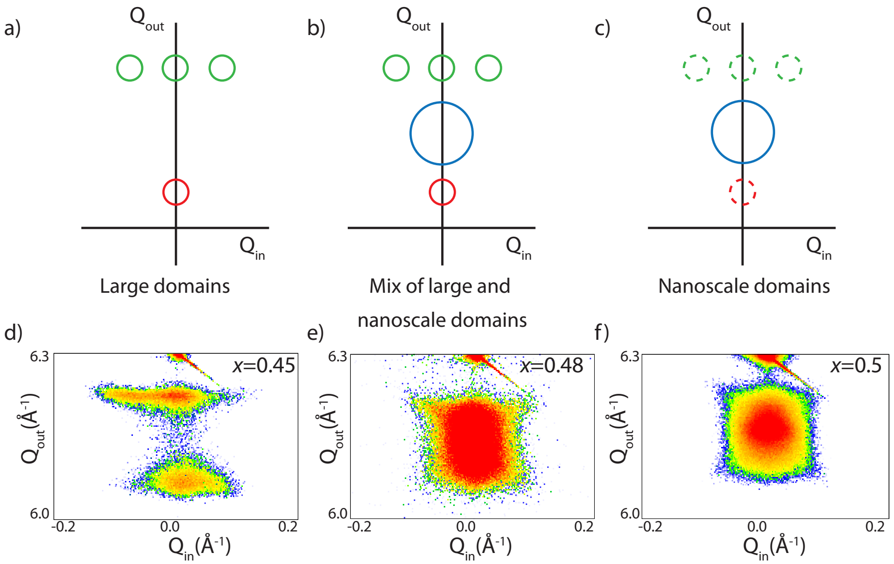

Figure 5.4: a) Schematical image of a (h0l)-RSMs of large domains bigger than the x-ray coherence length, b) large domains and nanoscale domains smaller than the x-ray coherence length and c) only nanoscale domains smaller than the x-ray coherence length, RSM of (004) peak of PZT d) $x = 0.45$, e) $x = 0.48$ and f) $x = 0.5$. The substrate peaks are shown on top of the images.

Another signature of the adaptive phase, in the x-ray diffraction measurement, according to the above model, is the shape of the peak in reciprocal space mapping. The peak width in horizontal direction ΔQ is proportional to the length of $\vec{K}$ [30]. This is significantly different from normal diffraction on large domains. Fig. 5.5(a) shows the peak width as function of order of the imaged peak, extracted from the RSMs on a PZT film with $x = 0.48$ on a KTO substrate for peaks (b) (001), (c) (002) and (d) (004). The peak width in the $(h0l)$-plane increases as function of the peak order l. It should be noted that these patterns with spherical envelopes with characteristic bulges in the diagonal directions are similar to the patterns observed in diffuse scattering experiments in relaxors [32], and are though to be originating from similar mechanisms.

5.3 Diffraction effect in nanoscale domains

Since lattice parameters are typically derived from the peak positions, the presence of an adaptive phase influences the values of the lattice parameters. First, the lattice parameters are studied for the complete range from $x = 0.0$ to 1.0. Subsequently, the lattice parameters in the region near the MPB are studied, in order to demonstrate the presence of the adaptive nanoscale domains and the substrate induced strain effect on the adaptive phase.

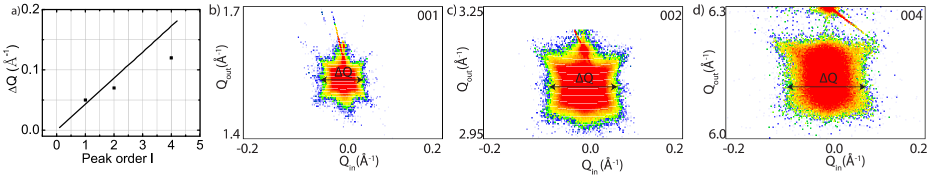

Figure 5.5: a) Effect of reciprocal peak order on peak morphology of a PZT with $x = 0.48$ film on KTO substrate. Peaks showing an increase of the peak width ΔQ for increasing peak order from b) (001), c) (002) and d) to (004), and the predicted values using eq. 5.1.

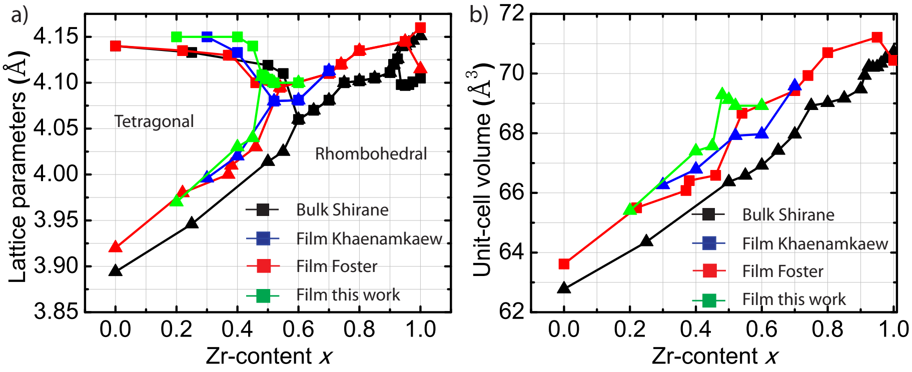

Figure 5.6: a) Lattice parameters and b) unit-cell volume as function of composition for bulk and film. Bulk data extracted from [33] (black), film data extracted from [34] (blue), [35] (red) and this work (green)

5.3.1 Compositional dependence of lattice parameters

The lattice parameters across the complete composition range of PZT films between $x = 0.2$ and 0.6 are shown in fig. 5.6(a), for bulk ceramics and films on STO substrates. The volume of the thin film unit-cell is larger than of the bulk, as shown in fig. 5.6(b). The data is taken from several references ([33] (black), [34] (blue), [35]) and this work (green). The behavior near the MPB is interesting, as the a and c lattice parameters appear equal. In bulk this occurs at compositions between $x = 0.6$ and 0.9. However for films, this region is extended to $x = 0.48$. We think the described nano domain formation in the film and the interference effect is the reason for this.

The a lattice parameter is larger in the films than for bulk, while the c parameter is close to the bulk data. The unit-cell volume is larger for thin-films than for bulk, for the complete composition range. The change of the a_1 lattice parameter in films with respect to bulk can be explained by a number of effects. Firstly, the oxygen content in bulk and films may be significantly different. An oxygen-

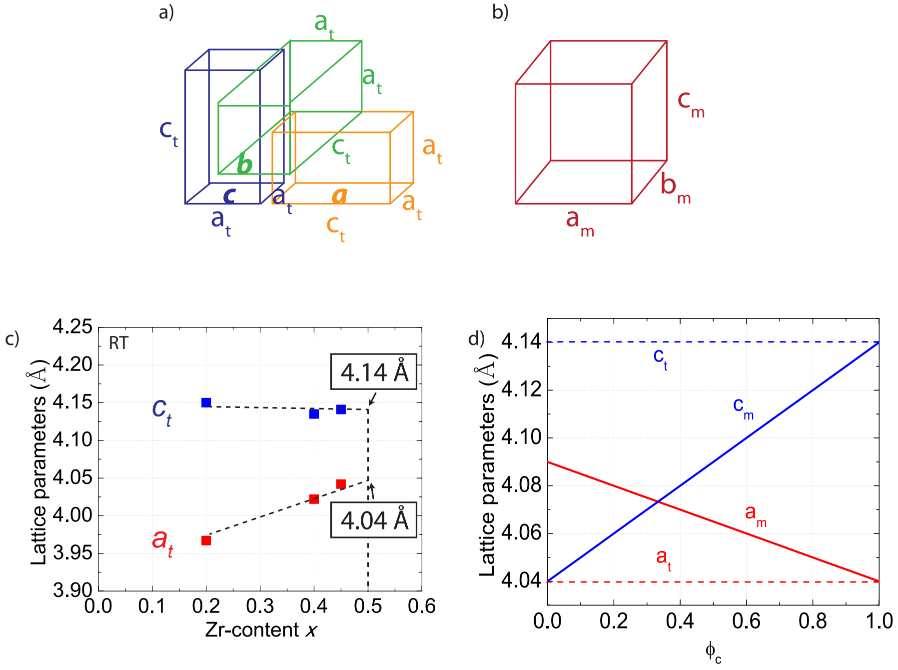

Figure 5.7: a) Schematic of the domain structure with nanoscale tetragonal a, b and c-domains, b) domain structure of the adaptive phase, c) the compositional dependence of the lattice parameters a_t and c_t, with the extrapolation of the trend towards $x = 0.5$, and d) lattice parameter of the homogeneous phase as function of ϕ_c for fixed $a_t = 4.04\mathring{A}$ and $c_t = 4.14\mathring{A}$.

deficient film is expected to have a lower volume of the unit-cell. The fabrication process of bulk ceramics is more likely to create oxygen deficiency, since it is based on mixing powder and sintering. Secondly, the bulk ceramics are polycrystalline, and the large number of grain boundaries in the film increases the volume fraction of defective region with a lower unit-cell volume. Thirdly, the Zr content could be different. However, Electron Diffraction (EDX) analysis indicated that the Zr content for our films was within 2% range of the intended composition.

5.3.2 General invariance condition

In this section, the adaptive phase theory is adjusted to the PZT domain structure. The lattice parameters are analyzed and an intrinsic relationship between the tetragonal building blocks and the observed single domain phase is explained. This intrinsic relationship is shown to apply to the PZT films independently of composition and temperature.

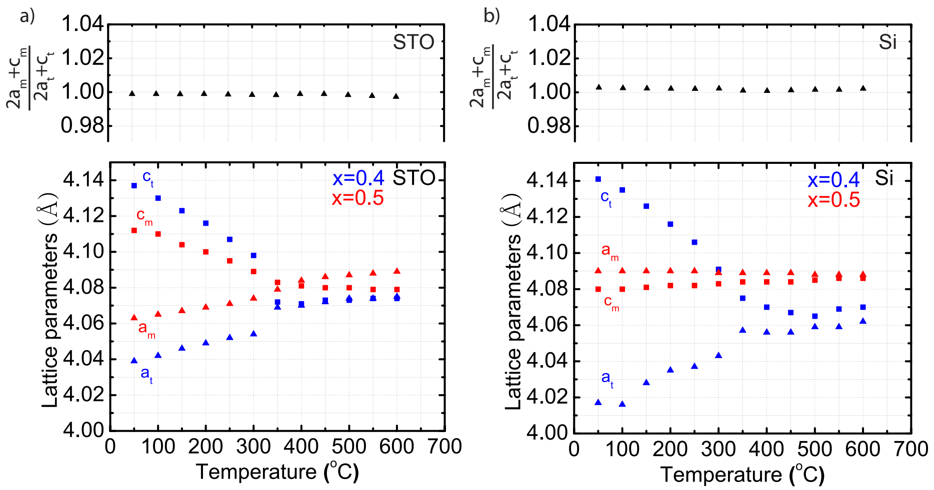

Figure 5.8: Temperature evolution of the lattice parameters a_t, c_t for $x = 0.4$ and $a_m = b_m$ and c_m for $x = 0.5$ a) on STO and b) on Si. The value of $\frac{2a_m+c_m}{c+(2a_t+c_t)}$ is shown in order to verify the GIC on STO and on Si

Figure 5.7(a) shows the domain structure in the PZT adaptive phase, with nanoscale tetragonal a, b and c domains. This is in contrast with the original theory for the adaptive phase, which only considers a and c-domains [36]. Therefore, an adjustments to the adaptive phase theory have to be made. The tetragonal domains are characterized by a spontaneous self-strain, with lattice parameters a_t of the short axis and c_t of the long axis, see fig 5.7(a). This self-strain is independent of substrate induced strain, as is seen in ch. 4. The self-strain of a tetragonal unit-cell can be described with respect to the cubic reference cell with lattice parameter a_c, using $\epsilon_3 = (c_t - a_c)/a_c$ and $\epsilon_1 = (a_t - a_c)/a_c$, where c_t and a$_t$ are the tetragonal lattice parameters. The total crystal strain averaged in all three Cartesian directions x, y and z is described by adding the tetragonal transformation strain of the a, b and c domains in these directions, according to

$$\begin{bmatrix} <\epsilon_1> \\ <\epsilon_2> \\ <\epsilon_3> \end{bmatrix} = \phi_c \begin{bmatrix} \epsilon_3 & 0 & 0 \\ 0 & \epsilon_1 & 0 \\ 0 & 0 & \epsilon_1 \end{bmatrix} + (\frac{1-\phi_c}{2}) \begin{bmatrix} \epsilon_1 & 0 & 0 \\ 0 & \epsilon_3 & 0 \\ 0 & 0 & \epsilon_1 \end{bmatrix} + (\frac{1-\phi_c}{2}) \begin{bmatrix} \epsilon_1 & 0 & 0 \\ 0 & \epsilon_1 & 0 \\ 0 & 0 & \epsilon_3 \end{bmatrix},$$

Note that this corresponds to a stress free state within the nanodomain (ϵ_1, ϵ_3 are equal to the self strains).

This expression can describe the macroscopically measured lattice parameter a_m, b_m and c_m directly in terms of the nanoscale tetragonal lattice parameters a_t, c_t and the cubic lattice parameters a_c as

$$\begin{aligned} a_m &= a_c(1+<\epsilon_1>) \\ &= \frac{1}{2}(a_t + c_t) - \frac{\phi_c}{2}(c_t - a_t) \end{aligned} \tag{5.5}$$

$$b_m = a_c(1+ < \epsilon_2 >) = a_m \tag{5.6}$$

and

$$\begin{aligned} c_m =& a_c(1+ < \epsilon_3 >) \\ =& \phi_c(c_t - a_t) + a_t \end{aligned} \tag{5.7}$$

It turns out that by addition $2a_m{+}c_m$, one obtains an expression which couples the lattice parameters of the nanoscale tetragonal phase to the macroscopic single domain phase, which is independent of ϕ_c. This *general invariance condition* (GIC) for PZT thin films in the adaptive phase with a, b and c domains is

$$2a_m + c_m = 2a_t + c_t, \qquad\qquad a_m = b_m \tag{5.8}$$

The GIC of eq. (5.8) can be used to verify the presence of the adaptive phase with a, b and c-domains, independent of ϕ_c. Fig. 5.8 shows the temperature evolutions of the lattice parameters a_t and c_t of films of the c/a-phase ($x = 0.4$) and a_m, c_m of the homogeneous single domain phase ($x = 0.5$) for different strain values: (a) on STO and (b) on Si. The lattice parameters a_t and c_t cannot be measured for $x = 0.5$. Therefore the lattice parameters a_t and c_t of $x = 0.4$ are used. The experimental lattice parameters across the boundary between the polydomain c/a-phase at $x = 0.4$ and the homogeneous single domain phase at $x = 0.5$ are studied. For the tetragonal c/a-phase, the in-plane a_t and out-of-plane c_t are measured, for the adaptive phase the in-plane a_m and the out-of-plane b_m are measured. The GIC is rewritten in

$$\frac{2a_m + c_m}{c + (2a_t + c_t)} = 1 \tag{5.9}$$

where a correction factor c is used to correct for the difference of the spontaneous tetragonal lattice parameters between $x = 0.4$ and 0.5. The difference between a_t at $x = 0.4$ and the extrapolated value for $x = 0.5$ is 0.02 Å, as can be seen in fig 5.7(c). The used value for c is 2·0.2+0=0.4. Temperature-dependence of c is considered to be negligible, for simplicity.

In order to verify the GIC, (c) shows the calculated value of $\frac{2a_t+c_t}{c+(2a_m+c_m)}$ as function of temperature. Remarkably, the values of $\frac{2a_t+c_t}{c+(2a_m+c_m)}$ are very close to the predicted value of 1 at all temperatures on STO and Si. It can be concluded that the GIC is valid for the studied PZT films. Note that the GIC for the c and a domains of ref. [6], $\frac{a_t+c_t}{a_m+c_m} = 1$, gives curves that do not agree. It is required to include the b-domains in the adaptive phase theory that was developed for the martensites that consist of a and c domains. The GIC for a, b and c domains gives a much better result. Secondly, it is shown that the GIC holds irrespective of the value of ϕ_c, as is demonstrated for the film with the largest difference in lattice parameters, on STO and Si. The special invariance conditions, as discussed in ref. [6], is not valid for our films. This is a consequence of the used domain structure in which the two in-plane directions are equal strain and the thermal strain ϵ_{th} in the film.

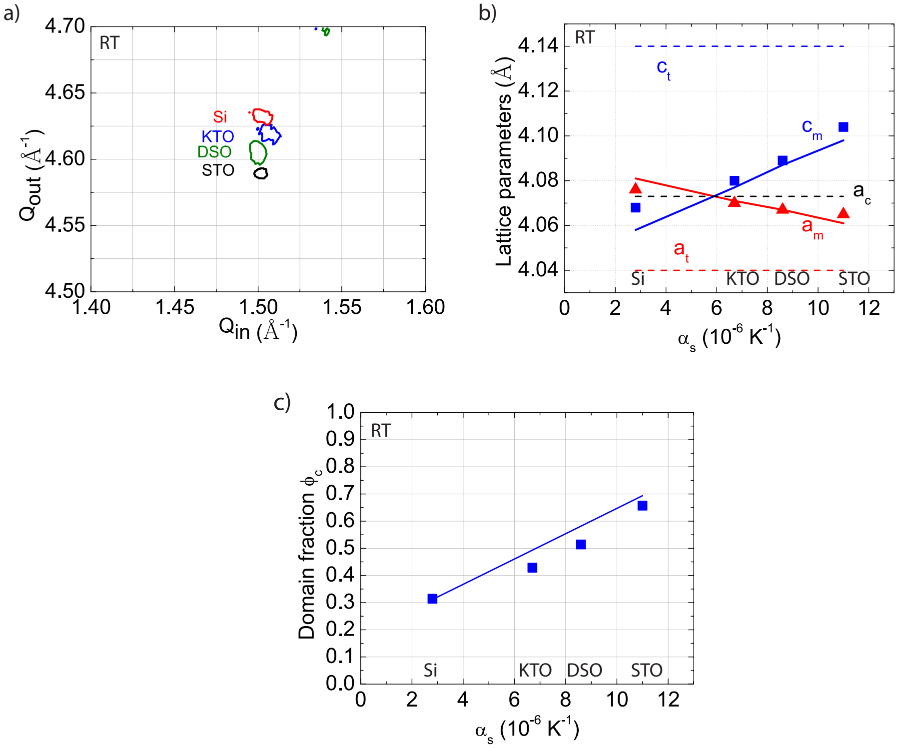

Figure 5.9: a) Reciprocal space maps of $x = 0.5$ on all substrates, b) Lattice parameters for $x = 0.5$ as function of α_s, and c) the domain fraction as function of α_s. All data is at room temperature (RT).

5.3.3 Strain effects on the adaptive phase

This section will show the substrate-induced strain dependence of the crystallographic and ferroelectric properties, following the adjusted adaptive phase theory. Another adjustment of the adaptive phase theory is made. The equations of sec. 5.3 are adjusted for a finite strain in the thin film. Subsequently, the experimental data are fit to this newly developed model.

The average strain in direction 1 is described in terms of lattice parameters, thermal expansion coefficient of the substrate and the domain fraction. Here the average residual strain is assumed to be $< \epsilon_1 >=< \epsilon_2 >= \epsilon_{th} = -\alpha_s(T_d - T_{RT})$, with α_s is the thermal expansion coefficient of the substrate, T_d is the deposition temperature and T_{RT} the room temperature. First the average strain is described by

$$< \epsilon_1 >= \epsilon_{th} = (\frac{\phi_c + 1}{2})\frac{a_t - a_c}{a_c} + (\frac{1 - \phi_c}{2})\frac{c_t - a_c}{a_c} \tag{5.10}$$

Based on eq. (5.11), the lattice parameters can be predicted as function of a_c and α_s. Note that this equation can be rewritten as the domain fraction of the c/a-phase in eq. (4.4) in ch. 4, since $2a_c\epsilon_{th}+2a_c = 2a_s^*$, with a_s^* being the effective substrate lattice parameter. The lattice parameters of the nanoscale tetragonal phase are related to the macroscopic single domain phase that is measured in XRD, for a certain strain value ϵ_{th},

$$a_m = b_m = (1+\epsilon_{th})a_c, \qquad c_m = 2a_t + c_t - 2a_c(1+\epsilon_{th}) \tag{5.11}$$

Figure 5.9(a) shows the peak position of the single domain film peaks on Si, KTO, DSO and STO. Fig. 5.9(b) shows the lattice parameters calculated according to eq. 5.11. and measured data as function of thermal expansion coefficient of the substrate α_s. Here, a_t=4.06 Å, c_t=4.14 Å, a_c= 4.075 Å, and α_s of $2.8\cdot 10^{-6}$ K^{-1},$6.7\cdot10^{-6}$ K^{-1}, $8.4\cdot10^{-6}$ K^{-1} and $11.0\cdot10^{-6}$ K^{-1} for Si, KTO, DSO and STO respectively. The model data is described by eq. (5.11). The measured a_m and c_m are derived from the peak position of the single domain film peaks on all substrates.

The domain fraction is obtained from eq. 5.10 as

$$\phi_c = \frac{2a_c\epsilon_{th} - (a_t + c_t - 2a_c)}{(a_t - c_t)} \tag{5.12}$$

The domain fraction in terms of a_m, c_m, a_t and c_t can be written as

$$\phi_c = \frac{c_m - a_t}{c_t - a_t} \qquad \phi_c = -\frac{2a_m - (a_t + c_t)}{c_t - a_t} \tag{5.13}$$

Fig. 5.9(c) shows ϕ_c of the model and data as function of thermal expansion coefficient of the substrate α_s. Agreement between the experimental and the theoretical values is obtained. A strong dependence of the domain fraction on substrate induced strain is found. It is noted (again) that by adapting the value of ϕ_c, the nano domains are stress-free. This is the condition for the applicability of the GIC. Hence, since the film at the MPB obeys the GIC, we conclude that the films are stress-free within the domains.

5.4 Discussion

The determination of the ϕ_c as function of the substrate induced strain, would not be possible without the adaptive phase theory. It should be noted that the results of the domain fraction, as shown in fig. 5.9, agrees to the trend that ϕ_c becomes more dependent on α_s for increasing Zr-content, as seen for the c/a-phase films studied in ch. 4. A point for future improvement of the adjusted adaptive theory is that it uses an extrapolation of a_t and c_t from the tetragonal composition toward the morphotropic phase boundary, as shown in fig. 5.7(c), leading to an uncertainty in the exact value of ϕ_c, that is corrected for by using the constant c.

The adaptive phase theory assumes infinitesimal small domain-wall width. If the domain width is of the order of ten nanometer, a domain-wall may occupy a significant amount of the crystal. The adaptive phase theory shows no possibility to incorporate such an effect. A similar observation was made in ref. [25], where this effect is shown to be important for the properties. In ref. [37], it is shown that for $BaTiO_3$ at RT from first-principles that the polarization switches 90° rather abruptly over about 5 nm, whereas the strain switches smoothly over a width of 21 nm. Many debates on the value of the domain-wall energy and width are present in literature. On the scale of domain sizes that are discussed here, even the smallest domain-wall width is expected to have significant effects on the properties of the PZT films. These ideas show overlap with the recent studies of fluctuations in the ionic positions at the atomic scale and spatially modulated phases [38].

5.5 Conclusions

Several indications of an adaptive phase are presented by study of the lattice parameter mechanisms and domain structure. A homogeneous single domain phase is observed by reciprocal space mapping. Piezo force microscopy and transmission electron microscopy images suggests the presence of domains sized smaller than 50 nm with characteristic (101)-domain boundaries. The adaptive phase theory from literature was adapted for PZT films with a, b and c domains. The experimental results are well described by the general invariance condition as function of composition and substrate-induced strain and temperature.

5.6 References

[1] W. Cao and E. Cross. Theoretical model for the morphotropic phase boundary in lead zirconate–lead titanate solid solution. *Phys. Rev. B.*, 47(9):4825, 1993.

[2] G. Rosetti, W. Zhang, and A. Khachaturyan. Phase coexistence near the morphotropic phase boundary in lead zirconate titanate (pbzro3-pbtio3) solid solutions. *Appl. Phys. Lett*, 88(7):072912–072912–3, 2006.

[3] J. Ouyang and A.L. Roytburd. Theoretical modeling of coexisting tetragonal and rhombohedral heterophase polydomain structures in lead zirconate titanate ferroelectric films near the morphotropic phase boundary. *Acta Mat.*, 54(20):5565–5572, 2006.

[4] P.G Lucuta. Ferroelectricdomain structure in piezoelectric ceramics. *Journal of the American Ceramic Society*, 72(6):933–937, 1989.

[5] B. Noheda, D.E. Cox, G. Shirane, J.A. Gonzalo, L.E. Cross, and S.E. Park. A monoclinic ferroelectric phase in the $Pb(Zr, Ti)O_3$ solid solution. *Appl. Phys. Lett.*, 74:2059, 1999.

[6] Y.M. Jin, Y.U. Wang, A.G. Khachaturyan, J. Li, and D. Viehland. Conformal miniaturization of domains with low domain-wall energy: Monoclinic ferroelectric states near the morphotropic phase boundaries. *Phys. Rev. Lett.*, 91(19):197601, 2003.

[7] M. Davis. Picturing the elephant: Giant piezoelectric activity and the monoclinic phases of relaxor-ferroelectric single crystals. *J. Electroceram.*, 19(1):25–47, 2007.

[8] L.A Schmitt, K.A Schonau, R Theissmann, H Fuess, H Kungl, and M.J Hoffmann. Composition dependence of the domain configuration and size in $Pb(Zr_{1-x}Ti_x)O_3$ ceramics. *J. Appl. Phys.*, 101(7):074107, 2007.

[9] S. Bhattacharyya, J.R. Jinschek, H. Cao, Y.U. Wang, J. Li, and D. Viehland. Direct high–resolution transmission electroc microscopy observation of tetragonal nanotwins within the monoclinic M_c phase of $Pb(Mg_{(1/3)}Nb_{(2/3)})O_3 - 0.35PbTiO_3$ crystals. *Appl. Phys. Lett.*, 92(14):14290, 2008.

[10] C. Ghica, L. Nistor, and G. Van Tendeloo. Revealing nanoscale structural ordering by $TEM/HRTEM$. application on $PMN - PT$ relaxor ferroelectric. *J. Optoelectr. Adv. Mat.*, 10(9), 2008.

[11] W. Chang, L. Lim, P. Yang, H. Miao, C. Tu, Q. Chen, and A. Soh. Tetragonal micro/nanotwins in $0.91Pb(Zn_{(1/3)}Nb_{(2/3)})O_3 - 0.09PbTiO_3$ revealed by reciprocal space mapping. *Appl. Phys. Lett*, 94(202907), Jan 2009.

[12] A.G. Khachaturyan, S.M. Shapiro, and S. Semenovskaya. Adaptive phase formation in martensitic transformation. *Phys. Rev. B.*, 43(13):10832, 1991.

[13] G.A. Rossetti and A.G. Khachaturyan. Inherent nanoscale structural instabilities near morphotropic boundaries in ferroelectric solid solutions. *Appl. Phys. Lett.*, 91(7):072909, 2007.

[14] C. Kittel. Thickness of domain walls in ferroelectric and ferroelastic crystals. *Solid State Comm.*, 10(1):119–121, 1972.

[15] M.J. Haun, E. Furman, H.A. Trolier-Mckinstry, and L.E. Cross. Thermodynamic theory of the lead zirconate–titanate solid solution system - part 2: Triclinic behavior. *Ferroelectrics*, 99:27–44, 1989.

[16] A.G. Khachaturyan. Ferroelectric solid solutions with morphotropic boundary: rotational instability of polarization, metastable coexistence of phases and nanodomain adaptive states. *Philos. mag.*, 90(1):37–60, 2010.

[17] K.A. Schönau, L.A. Schmitt, M. Knapp, H. Fuess, R.A. Eichel, H. Kungl, and M.J. Hoffmann. Nanodomain structure of $Pb(Zr_{1-x}, Ti_x)O_3$ at its morphotropic phase boundary: Investigations from local to average structure. *Phys. Rev. B.*, 75(18):184117, 2007.

[18] D.I. Woodward, J. Knudsen, and I.M. Reaney. Review of crystal and domain structures in the $Pb(Zr_{1-x}, Ti_x)O_3$ solid solution. *Phys. Rev. B.*, 72(10):104110, 2005.

[19] G. Catalan, A. Lubk, A. Vlooswijk, E. Snoeck, C. Magen, A. Janssens, G. Rispens, G. Rijnders, D. H. A. Blank, and B. Noheda. Flexoelectric rotation of polarization in ferroelectric thin films. *Nat. Mater.*, 10:963–967, Jan 2011.

[20] C.T. Nelson, B. Winchester, Y. Zhang, S.J. Kim, A. Melville, C. Adamo, C.M Folkman, S.H Baek, C.B Eom, and D.G Schlom. Spontaneous vortex nanodomain arrays at ferroelectric heterointerfaces. *Nano Lett.*, 2011.

[21] B. Meyer and D. Vanderbilt. Ab initio study of ferroelectric domain walls in $PbTiO_3$. *Phys. Rev. B.*, 65(10):104111, 2002.

[22] A. Morozovska. Phase diagram and domain splitting in thin ferroelectric films with incommensurate phase. *Phys. Rev. B.*, 81(195437):1–10, 2010.

[23] A. Levanyuk, S. Minyukov, and A. Cano. Universal mechanism of discontinuity of commensurate–incommensurate transitions in three–dimensional solids: Strain dependence of soliton self–energy. *Phys. Rev. B.*, 66(1):014111, Jul 2002.

[24] N.A. Pertsev, V.G. Kukhar, H. Kohlstedt, and R. Waser. Phase diagrams and physical properties of single-domain epitaxial $Pb(Zr_{1-x}, Ti_x)O_3$ thin films. *Phys. Rev. B.*, 67(5):054107, 2003.

[25] W. Rao and Y. Wang. Domain wall broadening mechanism for domain size effect of enhanced piezoelectricity in crystallographically engineered ferroelectric single crystals. *Appl. Phys. Lett*, 90(4):041915–041915–3, 2007.

[26] D. Damjanovic. A morphotropic phase boundary system based on polarization rotation and polarization extension. *Appl. Phys. Lett.*, 97:062906, 2010.

[27] V.G. Kukhar, N.A. Pertsev, H. Kohlstedt, and R. Waser. Polarization states of polydomain epitaxial $Pb(Zr_{1-x}, Ti_x)O_3$ thin films and their dielectric properties. *Phys. Rev. B.*, 73(21):214103, 2006.

[28] K.S. Lee, J.H. Choi, J.W. Lee, and S. Baik. Domain formation in epitaxial $Pb(Zr,Ti)O_3$ thin films. *J. Appl. Phys.*, 90:4095, 2001.

[29] Y.U Wang. Diffraction theory of nanotwin superlattices with low symmetry phase. *Phys. Rev. B*, 74(10):104109, 2006.

[30] Y.U. Wang. Diffraction theory of nanotwin superlattices with low symmetry phase: Application to rhombohedral nanotwins and monoclinic M_A and M_B phases. *Phys. Rev. B.*, 76(2):024108, 2007.

[31] J. Als-Nielsen and D. McMorrow. *Elements of Modern X-ray Physics.* Wiley, 2 edition, 2011.

[32] G Xu. Three-dimensional mapping of diffuse scattering in $Pb(Zn_{(1/3)}Nb_{(2/3)})O_3 - xPbTiO_3$. *Phys. Rev. B.*, 70(17):1744109, 2004.

[33] G. Shirane, K. Suzuki, and A. Takeda. Phase transitions in solid solutions of $PbZrO_3$ and $PbTiO_3$ (ii) x-ray study. *J. Phys. Soc. Japan*, 7:12, 1952.

[34] P. Khaenamkaew, S. Muensit, I.K. Bdikin, and A.L. Kholkin. Effect of Zr/Ti ratio on the microstructure and ferroelectric properties of lead zirconate titanate thin films. *Mat. Chem. Phys.*, 102:159–164, 2007.

[35] C. Foster, G.R Bai, R. Csencsits, and J. Vetrone. Single–crystal $Pb(Zr_xTi_{1-x})O_3$ thin films prepared by metal–organic chemical vapor deposition: Systematic compositional variation of electronic and optical properties. *J. Appl. Phys.*, 81(5):2349–2357, 1997.

[36] Y.M. Jin, Y.U. Wang, A.G. Khachaturyan, J.F. Li, and D. Viehland. Adaptive ferroelectric states in systems with low domain wall energy: Tetragonal microdomains. *J. Appl. Phys.*, 94(5):3629, 2003.

[37] Q. Zhang and W. Goddard. Charge and polarization distributions at the 90 domain wall in barium titanate ferroelectric. *Appl. Phys. Lett.*, 89(182903):1–3, 2006.

[38] A.Y. Borisevich, E.A. Eliseev, A.N. Morozovska, C.-J. Cheng, Y.H. Chu, D. Kan, I. Takeuchi, V Nagarajan, and S.V. Kalinin. Atomic-scale evolution of modulated phsaes at the ferroelectric-antiferroelectric morphotropic phase boundary controlled by flexoelectric interaction. *Nat. Comm.*, 3(775), 2012.

Chapter 6

Phase diagrams and functional properties of epitaxial $Pb(Zr,Ti)O_3$ thin films

Abstract

The misfit strain-dependence of ferroelectric properties for epitaxial polydomain $Pb(Zr_x,Ti_{1-x})O_3$ films of Zr-content $x = 0.2$, 0.4, 0.5 and 0.6 is presented. Misfit strain is controlled through thermal coefficient mismatch between film and the substrates silicon, $KaTaO_3$, $DyScO_3$ and $SrTiO_3$. The films are in the tetragonal c/a-phase for x= 0.2; 0.4, in the single domain r-phase for $x =$ 0.5 and in the monoclinic r/r-phase for $x = 0.6$. The lattice parameters are measured using x-ray diffraction with the reciprocal space mapping method and the strain is determined. Subsequently, *relative lattice parameters - misfit strain phase diagrams*, *temperature - misfit strain phase diagrams* and *misfit strain - composition phase diagrams* are constructed. For all studied phases, the out-of-plane remanent polarization shows an inverse non-monotonic relationship to the misfit strain. Moreover, the dielectric constant as function of the misfit strain shows a non-monotonic relationship and the piezoelectric coefficient is only weakly dependent on the misfit strain. Two phenomenological models are fitted to the data. The polydomain model gives accurate properties for $x = 0.2$ and $x = 0.4$, while for $x = 0.5$ and $x = 0.6$ the single domain model agrees.

6.1 Introduction

The deposition of perovskite films on silicon (Si) wafers is attracting great interest, since it promises the possibility of mass-production of thin-film devices using properties such as piezoelectricity, ferroelectricity, superconductivity, magnetism, and dielectricity. PiezoMEMS using Pb(Zr$_x$,Ti$_{1-x}$)O$_3$ (PZT) films on Si are often viewed as forerunner in this trend. The understanding of the effects of a Si substrate on the properties is therefore of major interest. It has been demonstrated in ch. 1 and 2 that there are large differences in properties between thin-films and bulk PZT. For example, clamping on the substrate may reduce the piezoelectric properties near the morphotropic phase boundary. The use of phenomenological model based on Landau-Devonshire-type (LD) theory has been proposed to describe the properties. However, no comprehensive verification of the models by experiments for several compositions and strain values is known in literature.

The recently achieved high-quality epitaxial growth of PZT films on Si opens up the possibility to study the effects of the biaxial in-plane strain [1]. This strain is the result of the mismatch in thermal expansion coefficient. It is tensile on Si, in contrast to the compressive strain on common single-crystalline substrates. By combining Si with conventional single-crystalline substrates, it is now possible to study the effect of a large range of misfit strain values on the crystalline and ferroelectric properties, without disturbance by defects.

Pertsev *et al.* developed a phenomenological model for single domain PZT films, which predicts a ferroelectric phase called the r-phase phase, which has polarization components in both the in-plane and out-of-plane direction for typically obtained strain values and compositions from $x = 0.0$ to 0.6 [2]. However, for films with thicknesses that are used for applications (> 100 nm), polydomain formation occurs. In the previous chapters, PZT films with the compositions $x =$ 0.2 and 0.4 are found to be in a polydomain tetragonal phase (ch. 4). Next to the tetragonal lattice strain of an individual domain, the fraction of the domains becomes an important ingredient in the LD-theory, as discussed in ch. 4. Chapter 5 studied PZT films near the morphotropic phase boundary, and concluded that PZT films with $x = 0.5$ appear to be single domain by x-ray diffraction, but can be modeled using an adaptive phase consisting of a nanoscale polydomain structure. An attempt to integrate these polydomain effects in the LD theory was presented by Kukhar *et al.* [3]. This resulted in a number of new polarization states and change of properties with respect to the single domain model. The comparison of experimental data with the theoretical models with respect to crystallographic and functional properties can verify whether application of the single domain or polydomain phenomenological model is preferred for certain composition and strain values. Certain interesting predictions of the LD models are tested, such as increased piezoelectric properties near crystallographic phase boundaries.

In this chapter, an experimental determination of the misfit strain and functional properties of epitaxial (001)-oriented Pb(Zr$_x$,Ti$_{1-x}$)O$_3$ thin films ($x = 0.2$; 0.4; 0.5 and 0.6) on different substrates and comparison to LD models is presented.

To vary the misfit strain, the differential thermal expansion coefficients of film and STO, DSO, KTO and Si substrates is used. The method to calculate the misfit strain for single domain films and polydomain films is discussed. The domain structure of the r/r monoclinic phase is discussed. The *relative lattice parameters / misfit strain phase diagrams* (sec. 6.3.4), *temperature / misfit strain phase diagrams* (sec. 6.3.5) and *misfit strain / composition phase diagrams*(sec. 6.3.6) are constructed. Furthermore, a dependence of the remanent polarization (sec. 6.4.1), dielectric constant (sec. 6.4.2) and piezoelectric coefficient (sec. 6.4.3) on strain and composition is obtained and compared to single domain and polydomain LD-models.

6.2 Crystallographic properties

Experimental results on the strain dependence of the domain structure and lattice parameters of the c/a-phase ($x = 0.2$; 0.4) were described in ch. 4, while the crystallographic properties near the morphotropic phase boundary ($x = 0.5$) were described in ch. 5. The crystallographic properties of the monoclinic $x = 0.6$ have not been presented yet in this thesis, and will be presented first. Subsequently, a method for the determination of the misfit strain values for all phases is described.

6.2.1 Crystallographic properties of x =0.6

Figures 6.1(c) shows the monoclinic domain structure, with the domain types r_1, r_2, r_3 and r_4. The two possible macroscopic domain structures of this phase are shown in fig. 6.1 (d). This phase is characterized by unequal a_1 and a_3, and a finite shearing tilt angle. Only if coincidentally a_1 and a_3 are equal, this phase can be defined as rhombohedral. Depending on the orientation of the rhombohedral domains with respect to the substrate, either the r_1/r_2 domain structure with (100) domain-walls or the r_1/r_4 domain structure with (110) domain-walls is present. In the first case, the monoclinic unit-cells are tilted toward the surface normal. In the second case, the monoclinic unit-cells are tilted toward the substrate surface and the crystals are parallel to the surface. Detailed information can be found in ref. [4]. In fig. 6.1, the reciprocal space maps around the (004) peak are shown, in the (a) (h0l)-plane and (b) (hk0)-plane. The peaks are attributed to domain types, as illustrated in the schematical representation of the reciprocal space maps. A clear peak splitting is obtained and therefore it is assumed that the film is polydomain r/r-phase. In order to determine the lattice parameter, the (103) peak is used, since it has an in-plane component (not shown). The average value of the two peaks is used. The peak positions depend on the substrate, out-of-plane lattice parameter a_3 decreases and the in-plane lattice parameter a_1 increases as function of thermal expansion coefficient of the substrates. The intensity of the different peaks corresponding to the domain types is not equal for all substrates. Therefore the domain fractions depend on the substrate. The (hk0)-scan indicates that on Si all four domain types have equal domain fraction, whereas on STO a single

Table 6.1: Table of crystallographic properties of PZT with $x = 0.6$. Short tetragonal axis a_1, long tetragonal axis a_3 and the tilt angle α.

subs	a_1	a_3	α
Si	4.118	4.088	0.31
KTO	4.112	4.100	0.31
DSO	4.105	4.129	0.33
STO	4.096	4.130	0.27

domain type is preferred and exhibits a domain fraction of 1. The tilt angle is independent of the substrate. The values are shown in table 6.1.

6.2.2 Temperature evolution of the lattice parameters

Figures 6.2 (a), (c), (e) and (f) show the temperature dependence pod the lattice parameters for PZT film with $x = 0.2$, 0.4, 0.5 and 0.6 on Si, KTO, DSO and STO substrates. The lattice parameters are extracted from the peak positions in reciprocal space maps, as described in ch. 3. For all compositions the high temperature phase is cubic and upon cooling a_3 increases and a_1 decreases. For $x = 0.5$, instead of a_1 and a_3, a_m and c_m are used, as described in ch. 5. The lattice parameters of the substrates are included in the graphs of fig. 6.2(a), (c), (e) and (f). The Si substrate lattice parameter is divided by $\sqrt{2}$, since it is in-plane rotated over 45° with respect to the PZT film. The measured thermal expansion coefficients of the substrates agree with literature values: Si $2.8{\cdot}10^{-6}$ K^{-1}, KaTaO$_3$ $6.7{\cdot}10^{-6}$ K^{-1}, DyScO$_3$ $8.4{\cdot}10^{-6}$ K^{-1} and SrTiO$_3$ $11.0{\cdot}10^{-6}$ K^{-1} [5].

For PZT films with $x = 0.2$ and 0.4 at room temperature, a_3 are nearly equal as function of Zr-content, while a_1 increases as function of Zr-content. The lattice parameters of the high temperature cubic phase increase as function of Zr-content. The domain fractions ϕ_c of PZT with $x = 0.2$ and 0.4 are determined from peak volume integration as discussed in ch. 4, and shown in fig. 6.2 (b) and (d). These values range between 0.82 and 0.3 at 50 °C. These observations agree with ϕ_c trends as function of temperature that were obtained in ch. 4.

The ferroelectric transition temperature T_C is found by extracting the intersection of the a_3 branch and the a_1 in the temperature evolution. The temperature was calibrated by a thermocouple on the sample and minimal difference between the value displayed by the XRD-apparatus and the sample temperature was found. T_C is shown in fig. 6.3. The T_C values of the phenomenological models are shown in fig. 6.3 as well, corresponding to the case of zero strain. The values are equal for the single domain [2] and the polydomain models [3] and bulk PZT. T_C decreases as function of Zr-content in both the phenomenological model and the measured data. Agreement is obtained between the experimental data and the models.

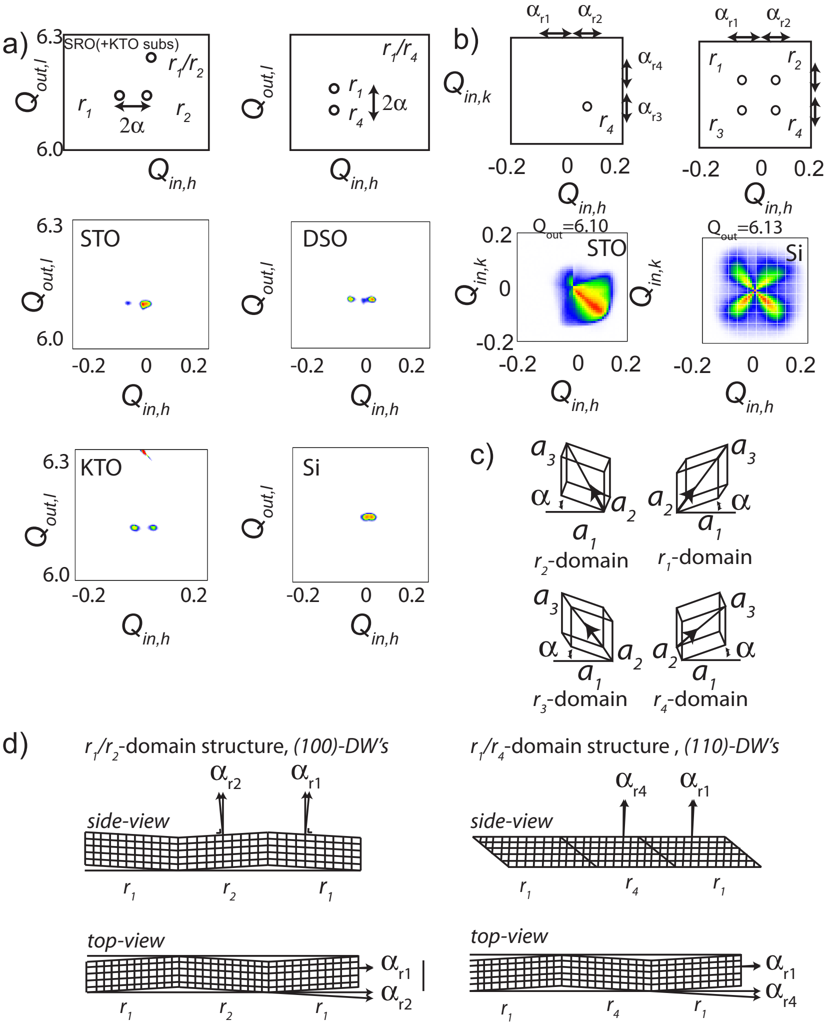

Figure 6.1: Reciprocal space maps for $x = 0.6$. (a) shows the (h0l)-scans on the (004) PZT peaks, showing either two or three peaks, indicating a mix of the r_1/r_2 and r_1/r_4 domain structure. (b) shows the (hk0)-scans for the (004) PZT peaks, (c) shows the different domain types and (d) shows the different domain structure types.

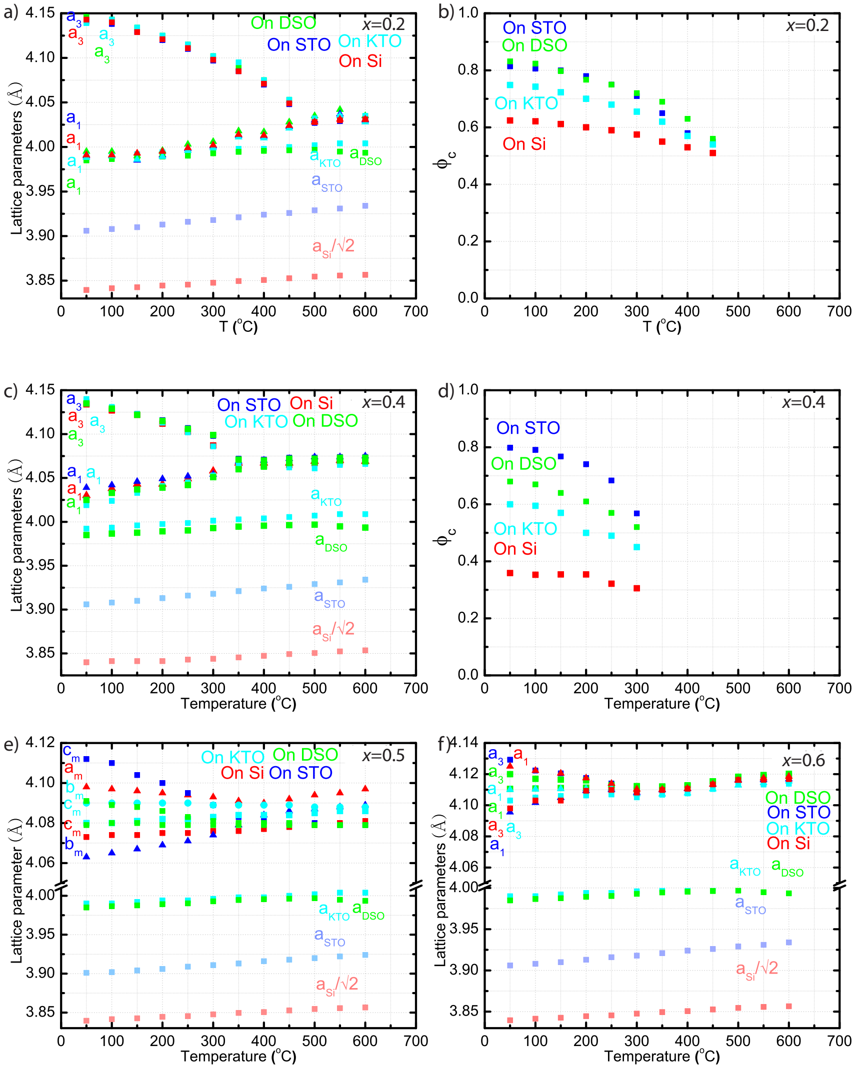

Figure 6.2: Temperature dependent lattice parameters of (a) x=0.2, (c) 0.4, (e) 0.5 and (f) 0.6, and domain fractions of (b) $x = 0.2$ and (d) 0.4.

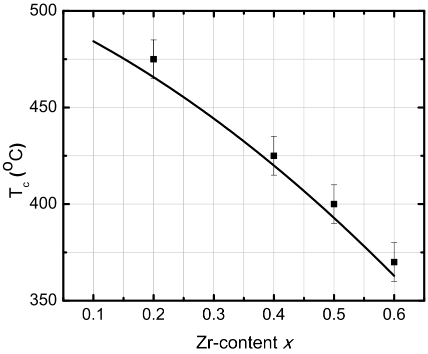

Figure 6.3: Ferroelectric transition temperature of PZT films as function of Zr-content, measured data (squares) and phenomenological data (line) from ref. [2] [3]

6.3 Misfit strain

The single domain and polydomain phenomenological theory developed by respectively Pertsev *et al.* [2] and Kukhar *et al.* [3], showed the stability of different crystallographic phases as a function of biaxial misfit strain for PZT compositions between $x = 0.2$ and $x = 0.6$. This theory has been discussed in detail in sec. 2.2.5. In order to perform a good comparison, the experimental misfit strain values should be determined in a way similar to the definitions in the phenomenological models. The method should take into account the spontaneous strain and the substrate induced strain. The following method allows comparison to the results of Pertsev [2] and Kukhar [3]. Typically, misfit strain S_m can be calculated following

$$S_m = \frac{a_1 - a_0}{a_0} \tag{6.1}$$

where a_1 is the in-plane lattice constant and a_0 the cubic reference lattice constant, calculated by a volume-conservation argument as $a_0 = (a_1^2 \cdot a_3)^{\frac{1}{3}}$. a_3 is the out-of-plane lattice parameter. This definition is used on the argument that the polarization is directly coupled to the deformation of the crystal from the (high temperature) cubic paraelectric phase. S_m can be determined independent of strain history and no high-temperature measurements are needed.

6.3.1 Misfit strain in the c/a-phase

As discussed in ch. 4, for the c/a-phase films, the lattice strain is independent of misfit strain. The film is stress-free, since the domain fraction is adjusted to the substrate induced strain. It should be noted that domain tilting due to the crystallographic matching at the domain-wall changes the in-plane strain by a factor $\cos(\omega)$. This effect is negligible for a typical tilt angle ω of 2° and therefore is not considered in the determination of the effective strain value. For PZT films consisting of a, b and c-domains, misfit strain is defined as

$$S_{m,j} = \phi_c S_c + \phi_a S_a + \phi_b S_b \tag{6.2}$$

with S_c, S_a and S_b the misfit strain values of the individual stress-free domains and ϕ_a, ϕ_b and ϕ_c are the domain fractions of the a b and c-domains. Since in-plane four-fold symmetry is assumed, $\phi_a = \phi_b = \frac{1-\phi_c}{2}$. The values are discussed in the following sections.

6.3.2 Misfit strain in the r/r-phase

For the r/r phase, no method to determine experimentally the misfit strain value is known. The r_1 to r_8 have equal monoclinic tilt angle α and polarization along the (111) of the unit-cell. The r_1 to r_4 domains are positively polarized in the out-of-plane direction and r_5 to r_8 are negatively polarized in the out-of-plane direction, as is illustrated in fig. 6.1. All four types of domain with similar out-of-plane polarization are equivalent in the out-of-plane direction and the relative domain fraction of the domains r_1 to r_4 does not affect the macroscopic out-of-plane polarization. This leads to the conclusion that the misfit strain value S_m can be approximated by a single domain, although the reciprocal space maps of this composition indicate the presence of a polydomain monoclinic phase. Another reason is based on analysis of the functional properties, as will be discussed in sec. 6.4.

6.3.3 Misfit strain values

The resulting S_m values are plotted as function of the thermal expansion coefficient of the corresponding substrate in fig. 6.4, for all used compositions. For $x = 0.2$ and 0.4, the S_m values are larger than of PZT films with $x = 0.5$. This is caused by the large spontaneous strain for $x = 0.2$ and 0.4. The trend of S_m on α_s is expected to be linear, since eq. (4.4) in ch. 4 showed that ϕ_c depends linearly on α_s, and eq. (6.2) S_m depends linearly on ϕ_c. For the single domain films, the expected linear relation between the misfit strain S_m and the thermal expansion coefficient of the substrate α_s is expressed by eq. (6.1). Using a least-squares method, a good linear fit is obtained, a linear relation between the thermal expansion coefficient of the substrate α_s and the misfit strain value S_m for all compositions.

6.3.4 Misfit strain - relative lattice parameter diagrams

Experiments in ch. 4 have shown that for the c/a-phase, the lattice strain is equal for the domain types a, b and c, and is independent of the substrate-induced strain. This agrees to the polydomain phenomenological model [3]. In order to illustrate this, fig. 6.5 (a)-(b) shows the relative lattice parameters a/a_0 as a function of misfit strain. Data is compared to relative lattice parameters - misfit strain ($\frac{a}{a_0}$,

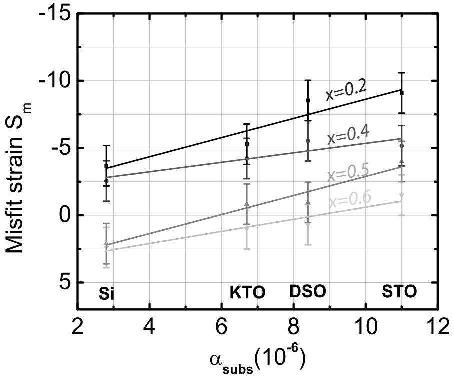

Figure 6.4: The misfit strain as function of the thermal expansion coefficient of the substrate α_s, for different compositions of PZT. A linear fit is applied for each composition.

S_m) diagrams, reproduced from Kukhar *et al.* [3] (indicated by the gray lines). For $x = 0.2$, the lattice strain remains constant as function of S_m. Unfortunately data is not provided by the polydomain model for this composition [3]. A constant trend of a_1/a_0 and a_3/a_0 is expected, similar to $x = 0.4$. For $x = 0.4$, the parameters are almost constant and these values agree well to the model. It should be noted that the model provides an additional parameter a_2, which corresponds to the relative lattice parameter in the direction perpendicular to a_1 and a_3. However, in the experimental data, no structural difference between a_1 and a_2 is observed. The experimental values are actually intermediate of a_1 and a_2 model curves. Possibly, the presence of the a_2 lattice parameter in the model, might be the consequence of the fact that *b*-domains are not incorporated in the model. For 'single domain' samples at $x = 0.5$ and 0.6 the relative lattice parameters are not shown. Since both S_m and a/a_0 are calculated from these lattice parameters values, actually the same data is plotted on the horizontal and the vertical axis. This would lead to a linear graph through zero and no useful information about the strain state of the film would be present in these graphs.

The domain fractions for *c*/*a*-phase films (as determined in ch. 4), as function of S_m are shown in fig. 6.5 (c) and (d), for x=0.2 and 0.4. A negative trend is observed, showing that a compressive strain increases the *c*-domain fraction [6]. For $x = 0.5$ and $x = 0.6$ no *c*/*a*-domain fraction applicable.

6.3.5 Misfit strain - temperature phase diagrams

Figure 6.6 shows the misfit strain / temperature (S_m, T) phase diagrams of PZT films with $x = 0.2$, 0.4 and x=0.5 on Si, KTO, DSO and STO substrates. The experimental data are obtained from temperature dependent x-ray diffraction (fig. 6.2), and plotted on top of the phenomenological models. S_m is calculated through eq. (6.1) and (6.2), using the lattice parameters and domain fractions measured

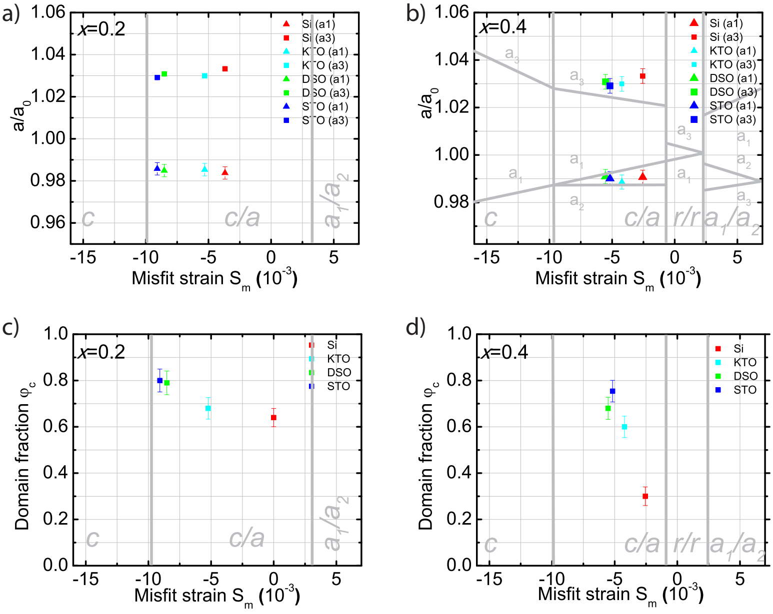

Figure 6.5: Experimental data (point) of the relative lattice parameters a_1/a_0 (△), and a_3/a_0 (□) as function of misfit strain for a) $x = 0.2$, b) $x = 0.4$. LD data [3] (lines)(LD data is not available for $x = 0.2$). Domain fractions as function of misfit strain for c) $x = 0.2$, d) $x = 0.4$. STO is denoted blue, DSO green, KTO cyan and Si red.

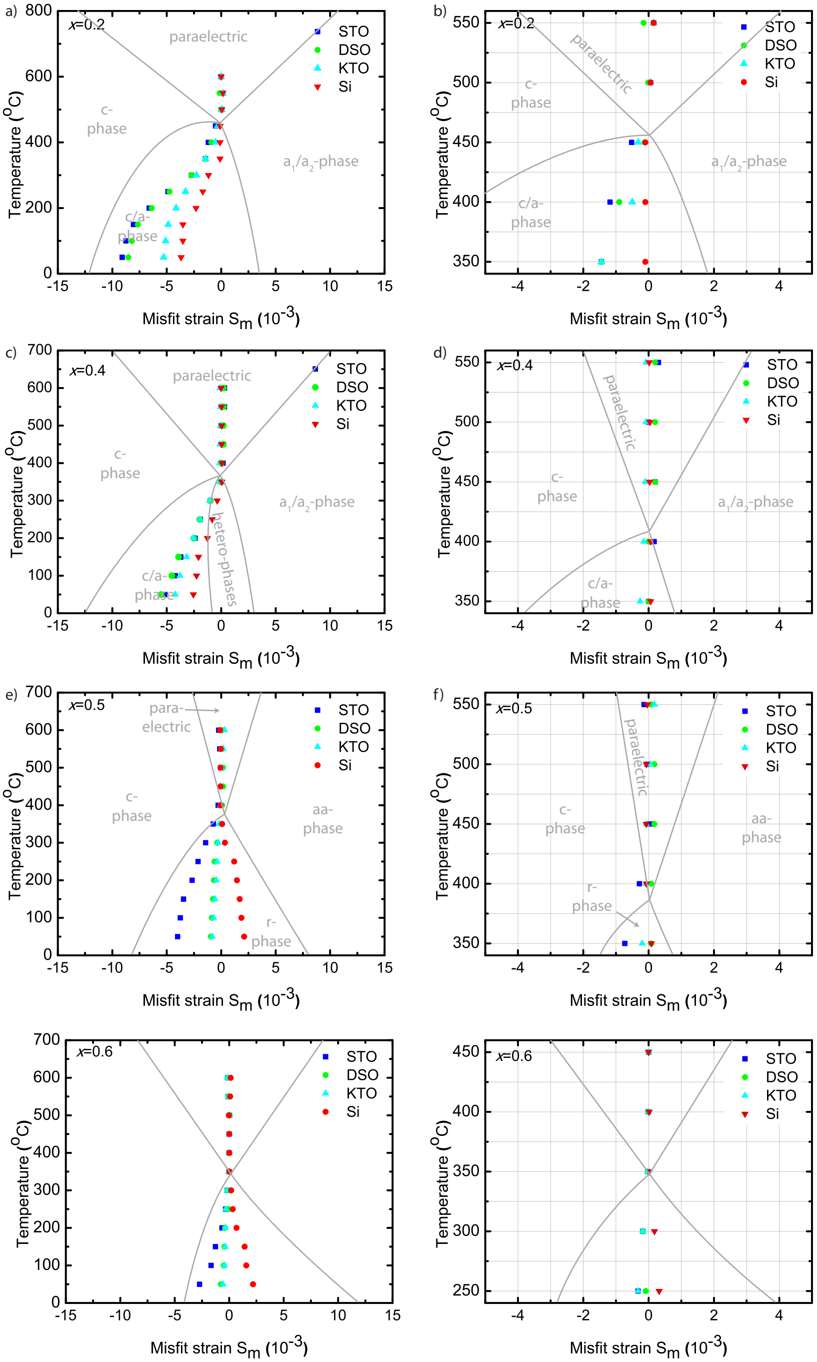

Figure 6.6: Misfit strain - temperature diagrams for PZT with (a) $x = 0.2$, (c) $x = 0.4$ and (e) $x = 0.5$ with measured data on Si, KTO, DSO and STO and zoom in of the ferroelectric transition region in (b), (d) and (f). The polydomain model [3] used for x=0.2 and 0.4 and single domain [2] for $x = 0.5$, illustrated by the gray lines. For $x = 0.6$, S_m is zero on all substrates and therefore not shown.

between T=50° and T=600°. The used LD models are single domain [2] for the composition x = 0.5 and 0.6, and polydomain [3] for the compositions x = 0.2 and 0.4. Above T_c, the single domain calculation (eq.(6.1)) is used, for all compositions.

For PZT films with $x = 0.2$ and 0.4, all films on STO, DSO and KTO fall into the region of the c/a-phase. For PZT films with $x = 0.4$, a number of hetero-phases are described the polydomain model [3], for which the polarization is unstable for a rotation away from the (001) axis for the c/a-phase or a (111) axis for the r/r-phase. No indications of the presence of hetero-phases are observed in the experimental data. For PZT films with $x = 0.5$, the films on all substrates are in the single domain r-phase at room temperature (RT). Positive S_m values are observed for films with composition $x = 0.5$ on Si, since $a_1 > a_3$. All lattice parameter curves are passing through the multiphase point at the lowest temperature of the paraelectric phase region. Above this temperature, the crystal is paraelectric and cubic. This point corresponds to the T_C of bulk PZT. This means that the misfit strain is 0 at this point. In the ferroelectric phase, stress-relaxation is taking place for the polydomain structure for PZT films with $x = 0.2$ and 0.4. For the composition $x = 0.5$, a nanoscale domain structure develops, as discussed in chapter 5 and the stress is relaxed. Above T_C, within the error margins the misfit strain value is zero.

6.3.6 Misfit strain - composition phase diagram

The room temperaturemisfit strain / composition phase diagram of PZT is shown in fig. 6.7. In order to make an easy comparison of the experimental data with the models, three plots are made. Fig. 6.7(a) shows the single domain misfit strain / composition phase diagram [2], fig. 6.7(b) shows the polydomain misfit strain / composition phase diagram [3] and fig. 6.7(c) shows the proposed misfit strain / composition phase diagram. The obtained misfit strain S_m values are inserted in all misfit strain - composition phase diagrams. The phase from the reciprocal space maps is compared to the location of the data points in the S_m-x phase diagram. For PZT films with $x = 0.2$ and 0.4, the films are in the c/a-phase, for the composition $x = 0.5$ the films are in the r-phase and for the composition $x = 0.6$ the films are in the r/r-phase. The discrepancy of the single domain model with experimental value is large, since the r-phase does not agree for PZT films with x=0.2, 0.4, and 0.6. The polydomain model [3] agrees for nearly all experimental data points. However, the results that are obtained by x-ray diffraction do not indicate that the phase boundaries between c/a and r/r-phase shifts to a lower x as function of misfit strain, as is predicted by the polydomain model [3]. For PZT films with $x = 0.4$ on Si, the point is close to the boundary between c/a and r/r-phase. In the proposed phase diagram, this boundary is drawn vertical at a certain composition between PZT films with $x = 0.4$ and $x = 0.5$. As seen in chapter 4 and 5, this boundary is not a sharp phase transition, but a region with a gradual change of crystallographic phase. Therefore, a single domain r-phase is added to fig. 6.7(c) for PZT films with $x = 0.5$.

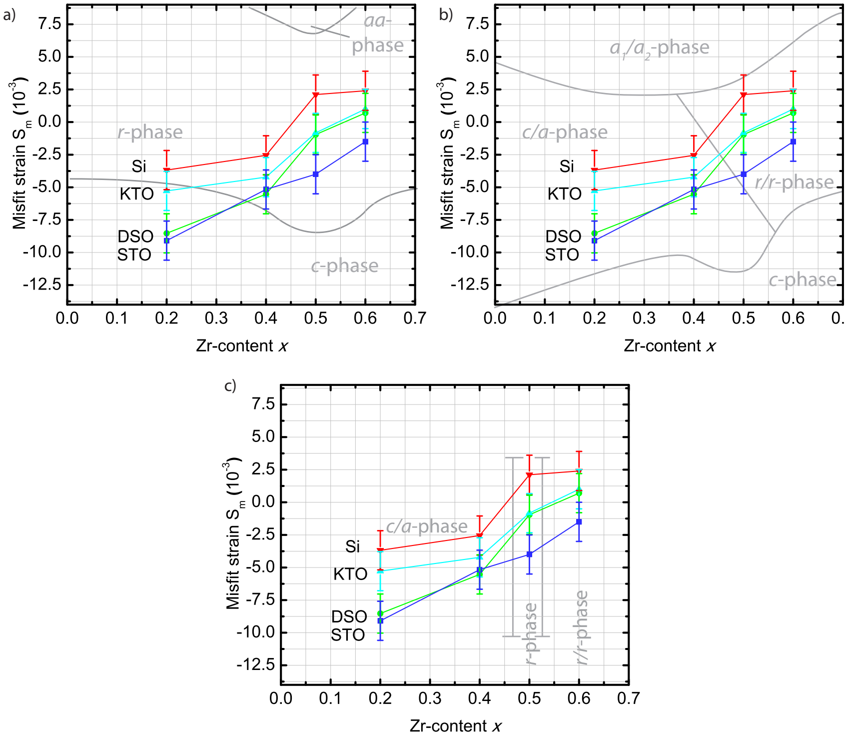

Figure 6.7: Misfit strain - composition diagram of PZT films, STO, DSO, KTO and Si. a) Data compared to single domain model [2], b) data compared to polydomain model [3], c) Proposed model based on crystallographic and functional properties, with the data. The lines between data points are guides for the eye. The gray lines indicate the obtained phases.

6.4 Functional properties

In this section the experimental functional properties are presented and compared to the phenomenological models. The PZT films with $x = 0.2$ and 0.4 films will be compared to the polydomain model [3] and the PZT films with $x = 0.5$ and 0.6 are compared to the single domain model [2]. The arguments for this choice will be explained in detail in this section.

6.4.1 Ferroelectric properties

The polarization loops on STO, DSO, KTO and Si substrates are shown in fig. 6.9, for all studied compositions. The remanent polarization at zero applied electric field is higher than a factor 0.75 of the saturation polarization at the maximum applied electric field, therefore the loops show a high degree of squareness for all samples. P_r of all films is tabulated in table 6.2 and shown as function of S_m in fig. 6.11.

It can be seen that for all compositions the remanent polarization decreases for increasing S_m value. In order to compare the data to the phenomenological models, the phenomenologically predictions from Pertsev *et al.* [2] and Kukhar *et al.* [3] are plotted using gray lines. Unfortunately no P_r data are present in the polydomain model [7]. Therefore, for PZT films with the compositions $x = 0.2$ and 0.4, a common analysis using the domain fraction is used for films with the composition $x = 0.2$ and 0.4. A clear relation of P_r on S_m is shown. Unfortunately no P_r data is present in the polydomain model [3].

The remanent polarization dependence of S_m may be analyzed in more detail, since the remanent polarization in the out-of-plane direction P_r depends linearly on the c-domain fraction ϕ_c, according to the relation $\mathrm{P}_r = \phi_c \mathrm{P}_s$, with P_s the spontaneous polarization of the bulk [7]. For PZT films with $x = 0.2$ and $x = 0.4$, ϕ_c is used from fig. 6.5(e) and (f) is used to calculate P_r values. Used values are $\mathrm{P}_s = 72\ \mu\mathrm{C/cm}^2$ for the composition $x = 0.2$ and $\mathrm{P}_s = 59\ \mu\mathrm{C/cm}^2$ for the composition $x = 0.4$, from bulk data as established by Haun [8]. The data is shown in fig. 6.8. For PZT films with $x = 0.2$, the experimental data are somewhat lower than the line $P_r = P_s$. For PZT films with $x = 0.4$, the data agrees. However the films on Si shows a slightly deviating value. For this PZT film with $x = 0.4$, the model indicates a $\phi_c P_s$ of 18 $\mu\mathrm{C/cm}^2$, originating from a measured ϕ_c of 0.3, while the experimental data shows a P_r of 35 $\mu C/\mathrm{cm}^2$. The discrepancy can be caused during the measurement of the P_r. The applied electric field in the out-of-plane direction may pole in-plane polarized region into out-of-plane polarized regions, thus effectively increasing the c-domain fraction. This mobility under an applied electric field has been shown to be larger for ϕ_c values between 0.3 and 0.7 than for values of 0.8 [9].

For PZT films with $x = 0.5$, the S_m dependence of P_r is present in the experiments. The data is compared to the single domain model, since sec. 6.4.2 will show that this model is more appropriate to fit to the dielectric constant [2]). For

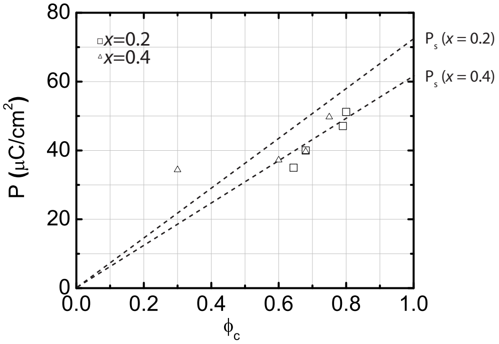

Figure 6.8: Polarization as function of the domain fraction for PZT with $x = 0.2$ and 0.4. Data points are the remanent polarization and the line is the predicted remanent polarization using $P_r = \phi_c P_s$.

PZT films with the composition $x = 0.6$, P_r is changing slightly between the film on several substrates. The data values are 10-20 $\mu C/\text{cm}^2$ lower than the model. Possible reason for this is that a fit of the monoclinic unit-cell to the substrate is inducing an additional tilt, therefore reducing the effective out-of-plane polarization component, depending on S_m.

6.4.2 Dielectric properties

The dielectric constants ϵ_r are tabulated in table 6.2 for all compositions and substrates, and plotted as function of S_m in fig. 6.11 on all substrates for PZT films with (d) $x = 0.2$ and 0.4, (e) $x = 0.5$ and (f) $x = 0.6$. The values are obtained using a CV measurement around E=0 V/m, as explained in sec. 3.4.3. The phenomenological models [2] [3] are plotted in gray.

For the PZT films with $x = 0.2$, the dielectric constant increases as function of S_m. For the PZT film with $x = 0.4$, a similar trend is observed with slightly higher values. ϵ_r of the PZT film with $x = 0.4$ on DSO is higher, which agrees to the more slanted P-E loop that is observed for this composition. It can be seen that the slope of the P-E loop $\frac{\delta P}{\delta E}$ at E = 0 V/m is proportional to the dielectric constant at E = 0 V/m. For the PZT film with $x = 0.2$, no polydomain data is present [3], however a similar trend at lower values than for the PZT film with $x = 0.4$ can be expected from analysis of the equation of the polydomain model [3]. For the PZT film with $x = 0.4$, the polydomain model [3] is plotted and agrees closely to the experimental data. The experimental values for the PZT film with $x = 0.5$ agree with the single domain model [2], as well as the observed trend of increasing ϵ_r as function of S_m. For the PZT film with $x = 0.6$, the experimental ϵ_r value of Si and KTO is close to those predicted by the single domain model. The ϵ_r values for DSO and STO are slightly lower.

It is noted that no fitting is applied in any of the graphs, apart from changing

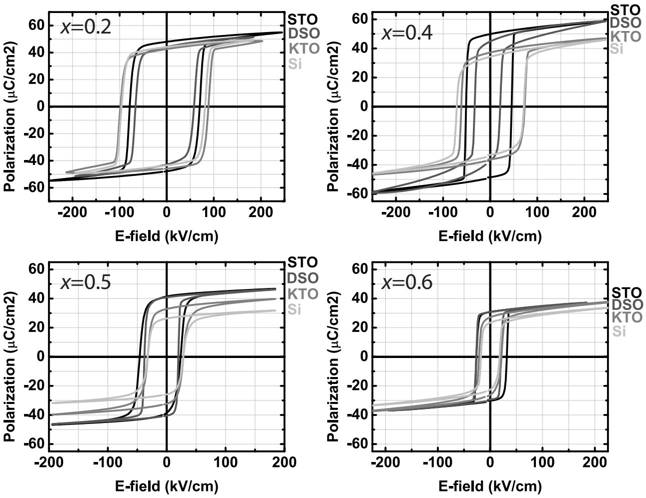

Figure 6.9: Polarization loops for all substrates for different compositions x = 0.2, 0.4, 0.5 and 0.6

either single [2] or polydomain model [3]. Based on the observation of nanoscale domains for PZT films with the composition $x = 0.5$, the use of a polydomain model [3] for this composition is suggested. However, unrealistic large dielectric constants are present in the polydomain model [3]. An example of this effect can be seen in fig. 6.11(d). In the r/r-phase, the dielectric constant of the polydomain model [3] is exceeding 8000. For $x = 0.2$ and 0.4, for which the films have S_m values that correspond to the c/a-phase, a good fit is obtained. For films with $x = 0.5$ and 0.6, the polydomain model [3] yields large dielectric constants for S_m values between -2.5·10^{-3} and 2.5·10^{-3} where the experimental S_m are located. Because of the large discrepancy with experimental data, the single domain model [2] is used for these compositions. In the polydomain model [3] there is a large contribution from the DW mobility to the ϵ_r, which is taken into account in the graph of Kukhar *et al.*. This can amount to 50 % of the ϵ_r value. If the domain-walls do not contribute, the film is effectively in the single domain state. This will be discussed further in the discussion section.

6.4.3 Piezoelectric properties

Figure 6.10 shows the d_{33}-E loops of PZT films for all compositions (for details, see sec 3.4.3). These loops agree to the d_{33}-E loops obtained from LD-modelling for the single domain phase, as shown in fig. 2.9 in sec. 2.2.4. The piezoelectric coefficient d_{33} near the coercive field is decreasing for increasing misfit strain S_m. The remanent $d_{33,r}$ values are given in table 6.2. The $d_{33,r}$ values are shown as function of S_m in fig. 6.11 for PZT films with (g) $x = 0.2$ and 0.4, (h) $x = 0.5$ and (i) $x = 0.6$. In general, the magnitude of the piezoelectric coefficient is less dependent on S_m than P_r and ϵ_r. For PZT films with the compositions $x = 0.2$

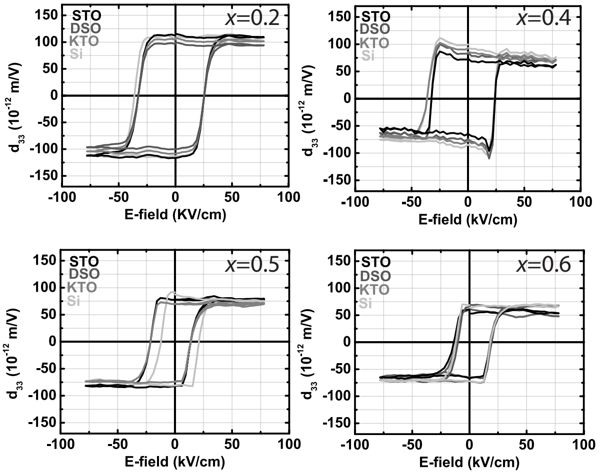

Figure 6.10: Piezoelectric coefficient d_{33} loops for all substrates for all compositions $x = 0.2$, 0.4, 0.5 and 0.6

Table 6.2: Table of remanent polarization P_r ($\mu C/cm^2$), dielectric constant ϵ_r and piezoelectric coefficient d_{33} ($10^{12} m/V$) for different substrates and compositions

Zr, x	$x = 0.2$			$x = 0.4$			$x = 0.5$			$x = 0.6$		
	P_r	ϵ_r	d_{33}	P_r	ϵ_r	d_{33}	P_r	ϵ_r	d_{33}	P_r	ϵ_r	d_{33}
Si	35.0	300	110	34.4	600	101	22.9	610	105	23.0	300	70
KTO	40.0	250	100	37.2	370	94	31.6	520	100	23.7	290	63
DSO	47.1	250	90	39.7	450	83	35.9	405	95	26.9	158	57
STO	51.2	180	80	49.7	350	72	40.6	315	90	27.5	125	50

and 0.4, the piezoelectric coefficients show a weak dependence on S_m with values going from 80 to 110 pm/V from STO to Si substrates. The polydomain model [3] does not provide data on the piezoelectric coefficients for these compositions. For PZT films with $x = 0.5$ and 0.6, a similar weak dependence on S_m is observed. For PZT films with $x = 0.5$, d_{33} values are close to the values that are predicted by the single domain model [2]. For PZT films with $x = 0.6$, the values are slightly lower than the predicted d_{33} value of 100 pm/V. Similar to the analysis of the dielectric constant, the polydomain model [3] is expected to overestimate the piezoelectric coefficients, due to a large domain-wall contribution. Although, the model does not provide exact values for the piezoelectric coefficient of PZT films in the r/r-phase, it can be seen that the single domain model shows a good fit for PZT films with $x = 0.5$ and 0.6.

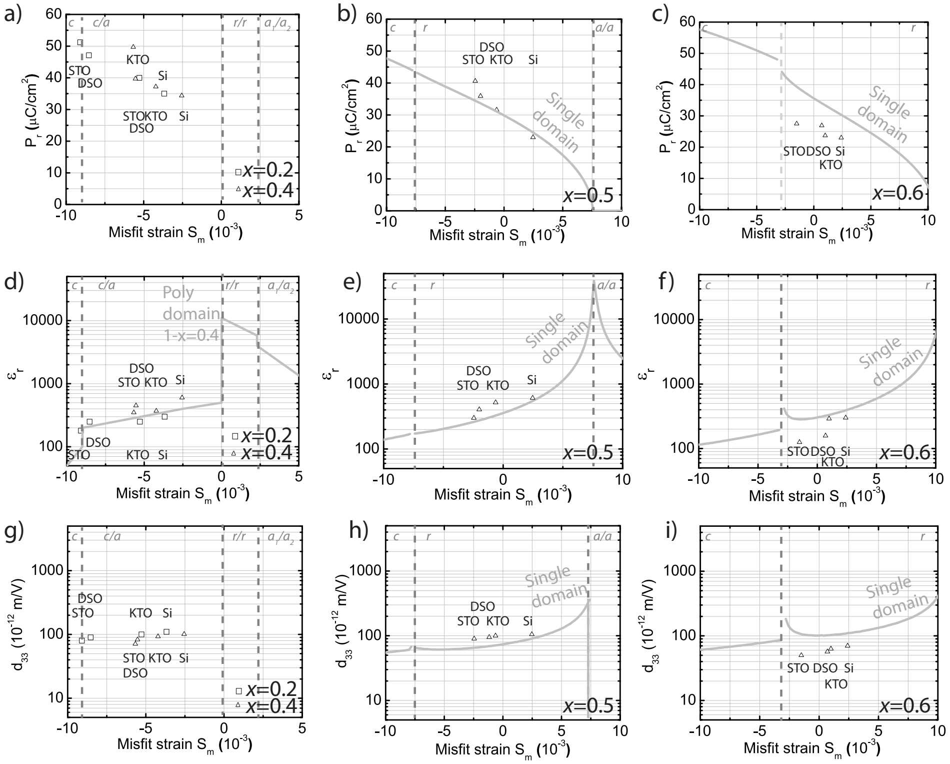

Figure 6.11: Remanent polarization as a function of S_m for a) $x = 0.2$ □, 0.4 △, b) $x = 0.5$, c) $x = 0.6$. Dielectric constant at electric field E=0 kV/cm as a function of S_m for a) $x = 0.2$ □, 0.4 △, b) $x = 0.5$, c) $x = 0.6$. Piezoelectric coefficient $d_{33,r}$ values for a) $x = 0.2$ □, 0.4 △, b) $x = 0.5$, c) $x = 0.6$. Gray lines present data taken from the single domain Pertsev *et al* model [2] and polydomain Kukhar *et al* model [3] and data points have similar symbols to the experimental data points for comparison. No phenomenological data for $x = 0.2$ is available. Therefore P$_r$ is calculated using the domain fraction and spontaneous polarization according to eq. (6.4.1). For $x = 0.4$ only ϵ_r data is available from the polydomain model [3]. For $x = 0.5$ and $x = 0.6$, the single-domain model is used.

6.5 Discussion

Misfit strain - composition diagram for polydomain films are a useful concept for visualizing crystalline phases in PZT thin film. However, uncertainty remains on the determination of the misfit strain values for the c/a-phase. The phenomenological polydomain model [3] does not incorporate the b-domains in the model. The misfit strain is calculated as the weighted sum of the misfit strain values of the individual domains, following $S_m = \phi_c S_m, c + (1 - \phi_c) S_{m,a}$, with $S_{m,c} = (a_1 - a_0)/a_0$ and $S_{m,a} = (a_3 - a_0)/a_0$ and $a_0 = (a_1^2 a_3)^{(1/3)}$. Ignoring the strain of the b-domains, $S_{m,b}$, has a significant impact on the total strain value S_m. Taking $S_{m,b}$ into account according to eq. 6.2, generally results in half the strain value.

The ferroelectric transition temperatures of PZT are between 350 and 480°C. However a shift of hundreds of degrees, as reported in ref. [10] and ref. [11], is not observed. Also no indications for the hetero-phases, for which the polarization is unstable, are found. This can be explained by the fact that they are equivalent in crystallography and that their properties are very close to the properties of the c/a-phase and therefore cannot be easily distinguished.

The functional properties show a remarkable fit of experimental data to the phenomenological models, considering that no fitting is used. The phenomenological models use coefficients that were obtained several decades ago on bulk PZT ceramics [8]. The data can be described best using the polydomain model of Kukhar *et al.* [3] for PZT with $x = 0.2$, $x = 0.4$, while $x = 0.5$ and $x = 0.6$ matches best with the single domain model of Pertsev *et al.* [2].

For films that are close to the boundary between the c/a-phase and r/r-phase in the polydomain model [3], a discrepancy between the model data and the experimental data is found. The model values for ϵ_r and d_{33} are much larger than observed. It is thought to be a consequence of the overestimation of ϵ_r by taking domain-wall displacement into account [9]. These finding indicate that the predictions of giant piezoelectric coefficients near the phase boundary between boundaries of c/a-phase, r-phase and the a_1/a_2-phase cannot be realized.

For PZT films with $x = 0.5$, the presence of nanoscale domains was suggested in ch. 5. This would imply the use of a polydomain model [3]. However the single domain model [9] shows a superior fit to the experimental data. The effect can be explained by the observance of the small domain-wall energies for this composition. According to Kittel [12] this leads to wide domain-walls, in which the polarization gradually rotates. The single domain model [9] describes films with polarization components in all three cartesian directions. The effects of the boundary conditions at the domain-walls which are used in the polydomain model [3] are not very strong if the domain-walls are diffuse. Therefore it is thought that the single domain is appropriate for modeling of the functional properties.

For PZT films with $x = 0.6$ a slight discrepancy between some data points and the single domain model is observed. This may be caused by the polydomain structure which has been observed by x-ray diffraction but is not incorporated in the single domain model. The addition of domain-wall effects in the model for monoclinic *r/r* phase would be beneficial for the understanding of the properties. The effect of strain on lattice strain and monoclinic domain tilting is unknown so far and a closer study would elucidate many aspects of the monoclinic and rhombohedral crystalline properties in films.

6.6 Conclusions

In conclusion, the effect of composition and misfit strain on epitaxial polydomain $Pb(Zr_x,Ti_{1-x})O_3$ films of Zr-content $x = 0.2$, 0.4, 0.5 and 0.6 is demonstrated. Reciprocal space mapping obtained by x-ray diffraction showed that PZT films with $x = 0.2$ and 0.4 are in the tetragonal c/a-phase, $x = 0.5$ is in a single domain r-phase and 0.6 is in a polydomain rhombohedral r/r-phase. Subsequently, relative lattice parameters / misfit strain diagrams, temperature / misfit strain diagrams and misfit strain / composition diagrams are constructed and compared to the Pertsev's and Kukhar's Landau-Devonshire (LD) model for biaxially strained thin films misfit strain-composition diagram of PZT is constructed. The transition temperature agrees to the LD models. Ferroelectric and dielectric properties are compared to LD-models as well. The out-of-plane remanent polarization shows an inverse non-monotonic relationship to misfit strain for all studied phases. The dielectric constant as a function of misfit strain shows a non-monotonic relationship for all compositions. The piezoelectric coefficients show a variation of maximum 10 % for PZT films with $x = 0.2$, 0.4 and 0.5 and 50 % for PZT films with $x = 0.6$. For PZT films with $x = 0.2$ and 0.4, the polydomain model of Kukhar fits the experimental results, while the single domain model is suited for PZT films with $x = 0.5$ and 0.6.

6.7 References

[1] M. Nguyen, M. Dekkers, E. Houwman, R. Steenwelle, X. Wan, A. Roelofs, T. Schmitz-Kempen, and G. Rijnders. Misfit strain dependence of ferroelectric and piezoelectric properties of clamped (001) epitaxial $Pb(Zr_{0.52}, Ti_{0.48})O_3$ thin films. *Appl. Phys. Lett.*, 99(252904):1244, 2011.

[2] N. Pertsev, V. Kukhar, H. Kohlstedt, and R. Waser. Phase diagrams and physical properties of single-domain epitaxial $Pb(Zr_{1-x}, Ti_x)O_3$ thin films. *Phys. Rev. B.*, 67(5):054107, 2003.

[3] V. Kukhar, N. Pertsev, H. Kohlstedt, and R. Waser. Polarization states of polydomain epitaxial $Pb(Zr_{1-x}, Ti_x)O_3$ thin films and their dielectric properties. *Phys. Rev. B.*, 73(21):214103, 2006.

[4] S. Streiffer, C. Parker, A. Romanov, M. Lefevre, L. Zhao, J. Speck, W. Pompe, C. Foster, and G. Bai. Domain patterns in epitaxial rhombohedral ferroelectric films. *I*. geometry and experiments. *J. Appl. Phys.*, 83:2742, 1998.

[5] R. Uecker, B. Velickov, D. Klimm, R. Bertram, M. Bernhagen, K. Rabe, M. Albrecht, R. Fornari, and D. Schlom. Properties of rare-earth scandate single crystals ($Re = Nd - Dy$). *J. Cryst. Growth*, 310(10):2649–2658, 2008.

[6] S. Alpay and A. Roytburd. Thermodynamics of polydomain heterostructures. iii. domain stability map. *J. Appl. Phys.*, 83:4714, 1998.

[7] V. Kukhar, N. Pertsev, and R. Waser. Thermodynamic theory of epitaxial ferroelectric thin films with dense domain structures. *Phys. Rev. B.*, 64(21):214103, 2001.

[8] M. Haun, E. Furman, S. Jang, and L. Cross. Thermodynamic theory of the lead zirconate-titanate solid solution system - part 1: Phenomenology. *Ferroelectrics*, 99:13–25, Nov 1989.

[9] N. Pertsev and A. Emelyanov. Domain–wall contribution to the piezoelectric response of epitaxial ferroelectric thin films. *Appl. Phys. Lett*, 71(25):3646, 1997.

[10] P. Janolin, F. Le Marrec, J. Chevreul, and B. Dkhil. Temperature evolution of the structural properties of monodomain ferroelectric thin film. *Appl. Phys. Lett.*, 90:192910, 2007.

[11] A. Sambri, S. Gariglio, A. Torres Pardo, J Triscone, O Stephan, J Reiner, and C Ahn. Enhanced critical temperature in epitaxial ferroelectric $Pb(Zr_{0.2}, Ti_{0.8})O_3$ thin films on silicon. *Appl. Phys. Lett.*, 98(012903):1–3, 2011.

[12] C. Kittel. Thickness of domain walls in ferroelectric and ferroelastic crystals. *Sol. State. Comm.*, 10(1):119–121, 1972.

Chapter 7

Advances in PiezoMEMS using Large Area Pulsed Laser Deposition

Abstract

PiezoMEMS using Pb(Zr_x,Ti_{1-x})O_3 films with $x = 0.52$ are fabricated by large area pulsed laser deposition. The films show a remanent polarization of 10 $\mu C/cm^2$, a dielectric constant of 1400 and a piezoelectric deflection at the center of 500-μm-diameter membrane of 17 nm/V at constant frequency well below its first resonance frequency, and 612 nm/V at the first resonance. The first resonance frequency ranges from 1.2769 MHz to 77.6 kHz for 250 μm to 1 mm diameter membranes and Q-factors of 87 to 236 for 250 μm to 1 mm diameter membranes. Interdigitated electrodes with a pitch of 5 μm were fabricated and show functionality with comparable properties to the parallel geometry devices. A device geometry with a patterned bottom electrode results in improved wire bonding yield.

7.1 Introduction

The integration of PZT thin films with silicon technology is the major driver for the research that is described in this thesis. A part of the efforts have been directed at the development of applications of PiezoMEMS using Pb(Zr_x,Ti_{1-x})O_3 films with $x = 0.52$ and large area pulsed laser deposition. The sensing and actuating capabilities of PiezoMEMS are used in many applications, such as inkjet printheads [1], energy scavengers [2, 3], micro-pumps [4], bio-sensors [5], micromachined ultrasound transducer (MUTs) [6, 7]. The use of pulsed laser deposition shows dense films with high functional properties. The recent development of large area pulsed laser deposition allows for fabrication with high throughput and low-cost, and has removed a major economical obstacle for the application of these complex oxide based devices.

Many devices that are based on dicing and glueing of bulk PZT ceramics show a limited compactness and resolution. Using PiezoMEMS, miniaturization of the size of the inkjet printing nozzles increases the printing resolution and decreases the ink consumption. Using deep reactive ion etching, arrays of membranes with a small pitch can be fabricated [8, 9]. This might be advantageous in case of limited space, for example in pMUTs that are situated in the tip of an endoscopic probe. The small device volume and low leakage currents offer a low-power consumption which might be an added value for wireless applications.

The PZT films for PiezoMEMS can be deposited by chemical methods [10–12], or physical vapor deposition [13–16]. Pulsed laser deposition (PLD) is a physical vapor deposition method, that delivers dense and homogenous films. Piezoelectric coefficients of $d_{33,f}$ of 180 pm/V [17] and $\mathrm{e}_{31,f}$ of -21 C/m^2 [18] have been obtained, which are relatively high in comparison to reports from literature [19]. A deposition speed of 1 μm per hour can be reached. The complete multilayer can be deposited in a single process run. An additional advantage is the option to deposit atomic monolayers to improve the device functionality. For example, the use of $SrRuO_3$ and $LaNiO_3$ between the platinum electrode and functional PZT increases the long-term stability drastically [20]. The development of large area pulsed laser deposition has allowed the deposition of PZT thin films on wafer scale. The development of standardized processing methodologies allows the simultaneous fabrication of several types of applications on a single wafer.

In this chapter, the characteristics are studied of a single-element piezoMEMS with PZT films with $x = 0.52$, fabricated by large area pulsed laser deposition in a parallel plate device geometry and interdigitated electrode geometry. First the ferroelectric, dielectric and piezoelectric properties are measured of the parallel plate geometry elements of 250, 500, 750 and 1000 μm diameter. Mechanical properties such as the resonance frequency and quality factors are characterized. A device geometry using interdigitated electrodes is fabricated and characterized. The device geometry for increasing the wire-bonding yield is explained.

7.2 Fabrication and experiments

7.2.1 Design

The studied PiezoMEMS devices consist of a silicon membrane covered by a piezoelectric films and electrodes in parallel plate geometry. Fig. 7.1(b) and (c) show the side-view and top-view of a device structure. The elements are designed with several diameters, influencing the deflection amplitude, resonance frequencies and Q-factors. In order to increase the wire-bonding yield, a patterned bottom electrode is added. Therefore, a shortcut between the top and bottom electrodes is

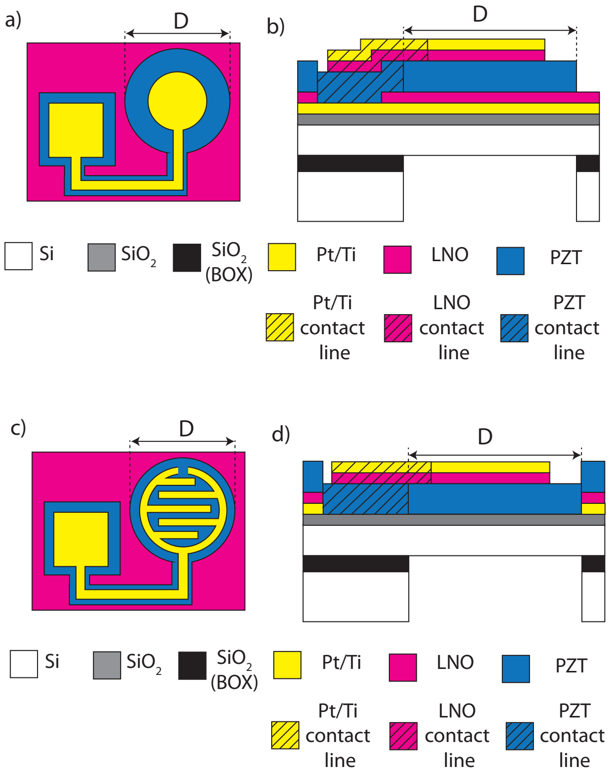

Figure 7.1: a) Top-view device geometry of D= 250 μm b) side view device geometry with wire bond pad and contact line.

avoided, in case a wire-bond damages the parallel plate geometry. The patterning is performed by locally etching of the platinum bottom-electrode, before deposition of the layers by large area pulsed laser deposition. The properties of the PZT of device-structure are unchanged. The quality of the PZT layer underneath the wire-bonding pad does not deteriorate, which would lead to an increase of the leakage current.

Next to the mentioned parallel plate geometry, a device using an interdigitated electrodes geometry is fabricated on an element with a diameter of 750 nm. Here the bottom electrode is removed and the top electrode forms a so-called fingerlike pattern, see fig. 7.1(c) and (d). The need for a bottom electrode deposition and optional bottom electrode patterning disappears. The applicable functional coefficients for this geometry are the in-plane remanent polarization P_1, the longitudinal in-plane piezoelectric coefficient d_{11} and and the longitudinal in-plane dielectric coefficient ϵ_{11}. The tensile strain that is induced by the silicon substrate, may increase the in-plane polarization fraction and alter the dielectric and piezoelectric coefficient, as seen in ch. 6. In fact, a high piezoelectric coefficients using this geometry have been reported in literature [9, 21].

7.2.2 Fabrication

Figure 7.2 shows the process flow of the device fabrication. The steps showing the application and patterning of the photoresist are not shown, only etch steps are shown. A silicon-on-insulator (SOI) wafer consist of the following layers: 100 nm platinum (Pt), 15 nm titanium (Ti), 521 ± 6 nm oxide, 10 μm silicon device layer, 500 nm buried oxide (BOX), 380 μm silicon handle and a $\sim$800 nm silicon oxide. The Pt and Ti layers are deposited by sputtering. The functional layers deposited by large area pulsed laser deposition (Solmates system) are 5 nm bottom electrode of $LaNiO_3$ (LNO), 1 μm piezoelectric $Pb(Zr,Ti)O_3$ and 100 nm top electrode LNO and 20 nm Pt top electrode.

Step 1 shows deposition of Ti and Pt on the SOI. Step 2 shows the patterning of the bottom electrode. Step 3 shows the deposition of LNO / PZT / LNO by large area pulsed laser deposition and Ti / Pt by sputtering. X-ray diffraction on the PZT showed a texture with preferred (001)-orientation. More detailed description of the crystalline properties can be found in chapter 3. Step 4 shows the etching of the Ti/Pt by reactive ion beam etching (RIBE). Step 5 shows the etching of the LNO/PZT/LNO stack, by a wet-etch using a diluted buffered-hydrofluoric acid (BHF) solution. Each layer requires individual resist application and patterning steps. Step 6 shows the deposition of SiO_2 by plasma-enhanced chemical vapor deposition (PECVD), which functions as a mask for the deep reactive ion etching (DRIE) of the membrane cavities. Step 7 shows the etching of the PECVD oxide by reactive ion etching (RIE). Step 8 shows the DRIE etching of the cavities. A protective polyimide (PI) layer on the functional layers is used. Subsequently the BOX layer is etched using RIE. Step 9 shows the dicing into 20x20mm chips. The top electrode coverage is 80%, for all diameters, which has been found optimum for the deflection amplitude. The diameter of the cavity is equal to the PZT diameter. The electrode contact lines are 5 mm wide and 20 nm thick. Resist stripping is executed by O_2-plasma. A 20x20 mm chip is mounted on a print plate and wire bonds are connect the bond pads to the print plate. A water tube with the transducer (receiving mode) or microphone (transmission mode) is place on top. Wire-bonding was done on a Kulicke & Soffa Analog Bonder (4522). A resulting wafer consisting of cantilevers, membranes, energy harvesters, pMUTs and bioMEMS devices is shown in fig. 7.3.

7.2.3 Experiments

The P-E loops are measured using a Aixacct TF2000 Analyzer system at 100 Hz and the C-V loops are measured on a Keithley 4200-SCS at 1kHz and small-signal voltage of 200 mV. Electromechanical properties are measured by Laser Doppler Vibrometer (LDV) using a Polytech MSA-400 Micro System Analyzer in combination with a lock-in amplifier by Stanford Research Systems SR 830 at 8kHz and small-signal voltage of 200 mV. Deflection amplitude is measured using the doppler shift of a laser interferometer in air. The signal is filtered at certain frequency, using a lock-in amplifier. 3 dimensional surface scan of the electromechanical deflection is done by the Polytech MSA-400 Micro System Analyzer. The device are

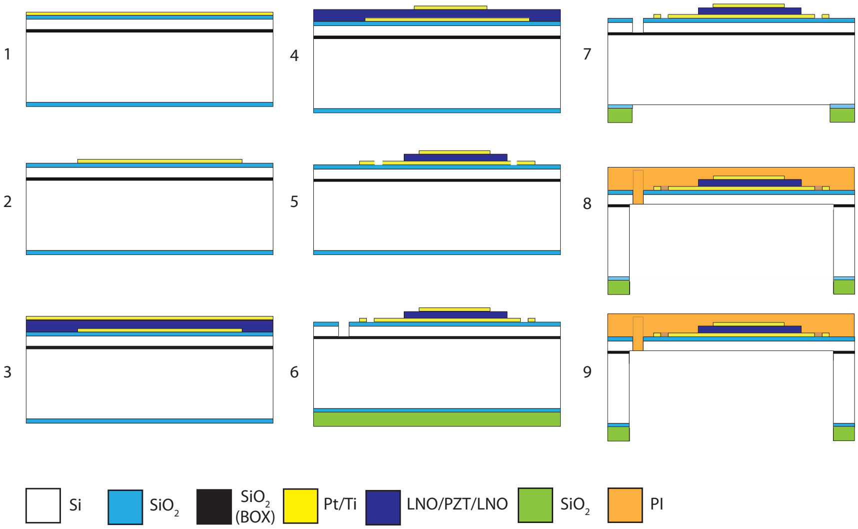

Figure 7.2: Summary of the process flow for wafer scale processing of the devices

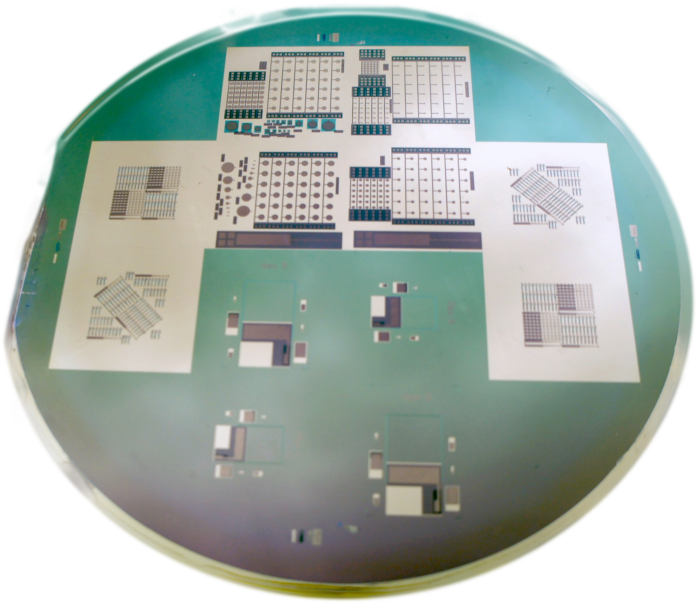

Figure 7.3: Picture of PZT wafer consisting of pMUTs, energy harvesters, beams for measurement of the transversal piezoelectric coefficient and cantilevers for mass detection.

actuated using a chirp signal of 350 mV in the range of 50 kHz to 2MHz, with a constant power value in the frequency domain. The 3 dimensional image represents the average RMS deflection over all frequencies, where the first resonance deflection is the most important signal.

7.3 Results

7.3.1 Wirebond-ready geometry

Wirebonding on the device geometry with the patterned bottom electrode shows a yield of 95%, in contrast to using a standard geometry, for which a yield of 20% is obtained. Since the bottom LNO layer is deposited after bottom electrode patterning, this layer is contacting the top electrode near the wire-bond pad. As anticipated, this contact does not short the device, since the in-plane conductivity of the 5 nm thick LNO layer is sufficiently low.

7.3.2 Ferroelectric, dielectric and piezoelectric properties

Figure 7.4 shows the switching current (I-E) loop, the polarization (P-E) loop and the dielectric (ϵ_r-E) loop, for an element of diameter of 750 μm. Elements with diameters of 250, 500 and 1000 μm have been found nearly similar to the shown 750 μm loops. Fig 7.5 shows the cross-sectional electromechanical deflection of a single element of (a) 250, (b) 500, (c) 750 and (d) 1000 μm. The presented deflection is the RMS average over the frequency range between 0.1 and 1.5 MHz. The first resonance deflection dominates the signal. Fig. 7.6(a) shows the frequency response the membranes. The first resonance frequencies are 77.6 kHz, 157.3 kHz, 348.5 kHz and 1.2769 MHz, for 1000, 750, 500 and 250 diameter membranes. The Q factor is defined as the ratio between the resonant frequency (f_r) and the width of the resonant peak at its half height (Δf), i.e. $Q = f_r/\Delta f$. The Q-factor 236, 144, 124 an 87 for 1000, 750, 500 and 250 diameter membranes, measured at the first resonance mode. The values are shown in fig. 7.6(b). Only the radial symmetrical resonance modes are observed, i.e. the first and the fourth. For actuating voltages higher than 350 mV also other resonance frequencies were interfering with the deflection signal.

7.3.3 Interdigitated electrode geometry

The devices with interdigitated electrodes, as illustrated in fig. 7.1(c) and (d), show functionality with comparable properties as the parallel geometry devices, as seen in fig. 7.7. A non-uniform electric field are present, due to the electrode geometry. This leads to an uncertainty in the applied electric field. It should be noted that the effective film thickness is approximately 5 μm. Therefore the applied voltage should be higher, since for a parallel plate capacitor $E = V/d$ with

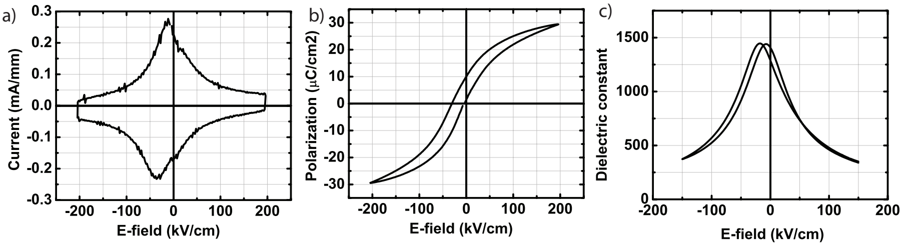

Figure 7.4: Functional properties of the element with a diameter of 750 μm, showing the a) switching current loop, b) polarization loop and c) dielectric constant loops

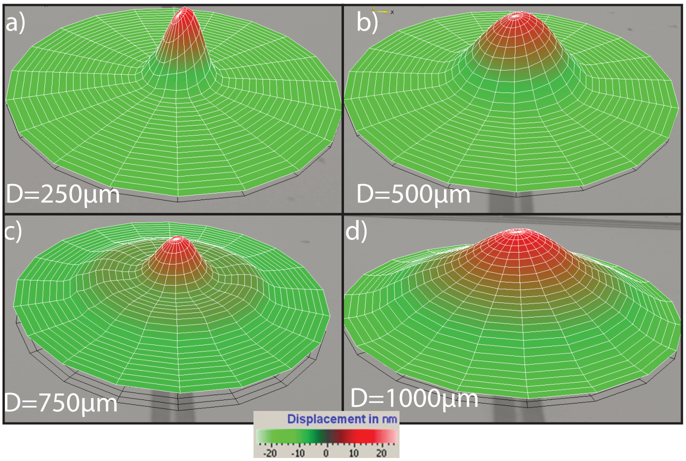

Figure 7.5: The element deflection integrated over the full spectrum, for diameter of a) 250 μm, b) 500 μm, c) 750 μm and d) 1000 μm.

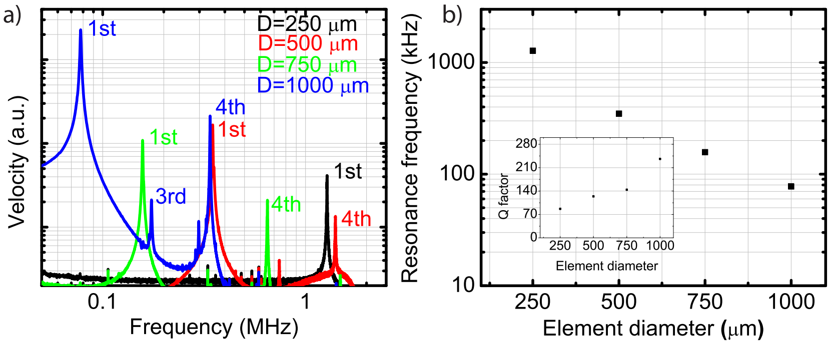

Figure 7.6: a) Deflection spectrum of all membranes, and b) the resonance frequency as function of diameter

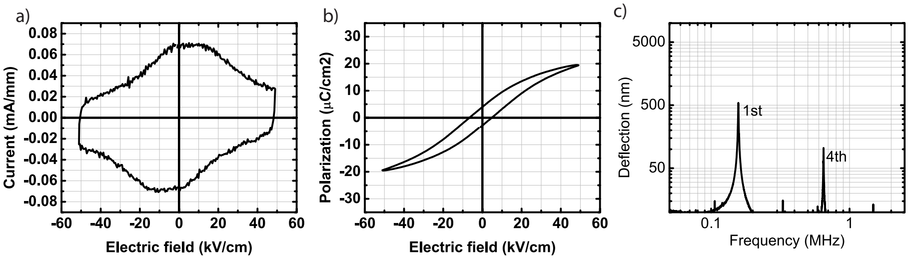

Figure 7.7: Functional properties of the pMUT element with interdigitated electrodes with a diameter of 750 μm, showing the a) switching current loop, b) polarization loop and c) deflection as function of frequency

E the electric field, V the applied voltage and d the film thickness. The maximum electric field is limited by the measurement equipment. The lower P_r values are related to the low applied electric field.

7.4 Conclusions

In conclusion, piezoMEMS consisting of PZT films, oxide electrodes and silicon membranes are fabricated using large area pulsed laser deposition. The films show a remanent polarization of 10 $\mu C/cm^2$, a dielectric constant of 1400 and a piezoelectric deflection at the center of 500-μm-diameter membrane of 17 nm/V at constant frequency well below its first resonance frequency, and 612 nm/V at the first resonance. The resonance frequency is found to range from 77.6 kHz to 1.2769 MHz for 1000 to 250 μm diameter membranes. A Q-factor of 236 to 87 for 1000 to 250 μm diameter membranes. Interdigitated electrode with pitch of 5μm were fabricated and shows comparable functionality to the parallel plate devices. A device geometry with a patterned bottom electrode results in improved wire bonding yield.

7.5 References

[1] B.H. Kim, S. Kim, J.C. Lee, S.J. Shin, and S.J. Kim. Dynamic characteristics of a piezoelectric driven inkjet printhead fabricated using mems technology. *Sens. Act. A.*, 173(1):244–253, 2012.

[2] D. Isarakorn, D. Briand, D. Janphuang, A. Sambri, S. Gariglio, J. Triscone, F. Guy, J. Reiner, C. Ahn, and N. de Rooij. The realization and performance of vibration energy harvesting mems devices based on an epitaxial piezoelectric thin film. *Smart Mater. Struct.*, 20(025015), 2011.

[3] K. Karakaya. The effect of the built–in stress level of aln layers on piezoelectric vibration energy harvesters. pages 1–7, Sep 2008.

[4] D.J. Laser and J.G. Santiago. A review of micropumps. *J. Micromech. Microeng.*, 14:R35–64, 2004.

[5] G. Campbell D. Maraldo, K. Rijal and R. Mutharasan. Method for label-free detection of femtogram quantities of biologics in flowing liquid samples. *Anal. Chem.*, 79:2762—70, 2007.

[6] D.E. Dausch, J.B. Castellucci, D.R. Chou, and O.T. van Ramm. Piezoelectric micromachined ultrasound transducer (pmut) arrays for 3d imaging probes. *IEEE Ultras. Symp.*, pages 930–933, Oct 2006.

[7] D.E. Dausch, J.B. Castellucci, D.R. Chou, and O.T. von Ramm. Theory and operation of 2-d array piezoelectric micromachined ultrasound transducers. *IEEE Transact. on Ultras., Ferroel. and Freq. Control*, 55(11):2484–2492, 2008.

[8] J. Baborowski. Microfabrication of piezoelectric mems. *J. Electroceram.*, 12(1):33–51, 2004.

[9] P. Muralt. Recent progress in materials issues for piezoelectric mems. *J. Am. Ceram. Soc.*, 91(5):1385–1396, 2008.

[10] T.A. Berfield, R.J. Ong, D. A. Payne, and N. R. Sottos. Residual stress effects on piezoelectric response of sol-gel derived lead zirconate titatnate thin films. *J Appl Phys*, 101(024102):1–7, 2007.

[11] Y. Otani, S. Okamura, and T. Shiosaki. Recent developments on mocvd of ferroelectric thin films. *J. Electroceram.*, 13(1):15–22, 2004.

[12] H.C. Lee and W.J. Lee. Characterization of $Pb(Zr,Ti)O_3$ thin films fabricated by plasma enhanced chemical vapor deposition on Ir-based electrodes. *J. Vac. Sci. Technol. A.*, 20:1939, 2002.

[13] T. Maeder, P. Muralt, L. Sagalowicz, and N. Setter. In-situ sputter deposition of pt and pzt films on platinum and RuO_2 electrodes. *Microel. eng.*, 29(1-4):177–180, 1995.

[14] B.E. Park, S. Shouriki, E. Tokumitsu, and H. Ishiwara. Fabrication of $PbZrTiO_3$ films on Si structures using Y_2O_3 buffer layers. *Jpn. J. Appl. Phys.*, 37:5145–5149, 1998.

[15] C.B. Eom, R.B. Van Dover, J.M. Phillips, D.J. Werder, J.H. Marshall, C.H. Chen, R.J. Cava, R.M. Fleming, and D.K. Fork. Fabrication and properties of epitaxial ferroelectric heterostructures with $SrRuO_3$ isotropic metallic oxide electrodes. *Appl. Phys. Lett.*, 63(18):2570–2572, 1993.

[16] J.F.M. Cillessen, M.W.J. Prins, and R.A. Wolf. Thickness dependence of the switching voltage in all-oxide ferroelectric thin-film capacitors prepared by pulsed laser deposition. *J. Appl. Phys.*, 81:2777, 1997.

[17] Solmates B.V. Internal communication. Technical report, Mesa+ Institute for Nanotechnology, University of Twente, 2011.

[18] X. Wan. Unpublished. 2012.

[19] A. L. Kholkin. Electromechanical properties and domain-related effects in ferroelectric thin films. *Ferroelectrics*, 221(1):219–228, 1999.

[20] M.D. Nguyen. *Ferroelectric and piezoelectric properties of epitaxial pzt films and devices on silicon.* PhD thesis, University of Twente, 2010.

[21] H. Yu, L. Zou, K. Deng, R. Wolf, S. Tadigadapa, and S. Trolier-Mckinstry. Lead zirconate titanate mems accelerometer using interdigitated electrodes. *Sens. Act. A.*, 107:26—35, 2003.

Chapter 8

Summary

The deposition of perovskite oxide thin films on silicon wafers is attracting great interest, since it promises the possibility of mass-production of thin film devices with functional mechanisms such as piezoelectricity, ferroelectricity, superconductivity, magnetism, and dielectricity. Piezoelectric Micro Electro Mechanical Systems (PiezoMEMS) using $\mathrm{Pb(Zr}_x\mathrm{,Ti}_{1-x}\mathrm{)O}_3$ (PZT) films on silicon are often viewed as forerunner in this trend, with promising applications such as inkjet printheads, piezoelectric micromachined ultrasound transducers and energy harvesters. The recently achieved high-quality epitaxial PZT films on silicon substrates by pulsed laser deposition offer the opportunity to study the fundamental relation between ferroelectric and crystallographic properties.

This thesis studies the effects of strain and composition on the crystallographic and functional properties of PZT thin films. A wide range of strain values and compositions are achieveable and their mutual interactions are studied. In the used epitaxial PZT films, the effects that are not related to the intrinsic properties are minimized, such as grain boundaries, mixed orientations, space charge or misfit dislocations. The films are grown in a functional device geometry and are of a thickness that is regularly used in applications, such as PiezoMEMS. At this thickness, the films are relaxed from epitaxial strain. Owing to the high temperature deposition in pulsed laser deposition and subsequent cooling to room temperature, the thermal strain becomes the dominant parameter in determining the properties of the PZT heterostructures. An important aspect of PZT films and strongly dependent on the composition, is domain formation. For low Zr-content, the strain is relaxed by forming large tetragonal domains, while for PZT near the morphotropic phase boundary, nanoscale domains occur with an unknown stress relaxation mechanism. Several analytical and thermodynamical models may be used to link the crystallography to the functional properties.

In chapter 3, several aspects of epitaxial PZT heterostructures on silicon are described. The fabrication and characterization are explained, followed by a discussion of the growth of epitaxial buffer layers on silicon, the control of crystal orientation on these buffer layers and the resulting quality of the epitaxial PZT heterostructures on silicon. It is found that strontium titanate (STO) and yttria-stabilized zirconia (YSZ) buffer layers can be grown epitaxially on silicon. The PZT grown on the STO-buffered silicon substrate shows the best quality and is therefore preferred for the intrinsic study of the properties of the PZT films on silicon.

In chapter 4, the relation between domain fraction, domain inclination and substrate-induced strain in epitaxial PZT films is studied. PZT films with $x =$ 0.2, 0.4 and 0.45 are in the tetragonal c/a-phase, and the domain fraction is found to depend strongly on the strain while the lattice parameters remain constant. Next to tilted a and b-domains, tilted c-domains are observed in the a and b-directions with a tilt angle that is dependent on the strain. A model was derived for the domain tilting as function of domain fraction and strain and shows a good fit to the experiments. On silicon, the c-domain fractions are low and the film approaches the a_1/a_2-phase for which increased dielectric and piezoelectric properties are predicted.

The crystallographic properties near the MPB in PZT thin films has been underexposed in literature. Therefore, $Pb(Zr_x,Ti_{1\text{-}x})O_3$ films with $x = 0.48$ to 0.52 are characterized in chapter 5. Several indications of an adaptive phase with nanoscale textures are presented. A small or negative domain-wall energy results in domain structure in which the domain fraction can easily be adjusted to strain and electric field. A homogeneous single domain phase is observed by x-ray diffraction with reciprocal space mapping, that is explained by the x-ray scattering effects on nanoscale domains. Piezo force microscopy and transmission electron microscopy images suggest the presence of domains with a size smaller than 20 nm. The adaptive phase theory from literature was adapted for PZT films with a, b and c domains. The experimental results are well described by the general invariance condition that couples the intrinsic lattice parameters to the measured lattice parameters. It is shown that this relation is valid as function of composition, substrate-induced strain and temperature.

Chapter 6 demonstrates the effect of composition and misfit strain on epitaxial polydomain $Pb(Zr_x,Ti_{1-x})O_3$ films of Zr-content x=0.2, 0.4, 0.5 and 0.6. Reciprocal space mapping obtained by x-ray diffraction showed that PZT films with x=0.2 and 0.4 are in the tetragonal c/a-phase, x=0.5 is in a single domain r-phase and 0.6 is in a polydomain rhombohedral r/r-phase. Subsequently, relative lattice parameters / misfit strain diagrams, temperature / misfit strain diagrams and misfit strain / composition diagrams are constructed and compared to the Landau-Devonshire (LD) model of Pertsev and Kukhar for biaxially strained thin films. The transition temperature agrees to the LD models. Also the ferroelectric, dielectric and piezoelectric properties are compared to LD-models. The out-of-plane remanent polarization shows an inverse non-monotonic relationship to misfit strain for all studied phases. The dielectric constant as a function of misfit strain shows a non-monotonic relationship for all compositions. The piezoelectric coefficients show a variation of maximum 10 % for PZT films with $x = 0.2$, 0.4 and 0.5 and 50 % for PZT films with $x = 0.6$. For PZT films with $x = 0.2$ and 0.4, the polydomain model of Kukhar fits the experimental results, while the single domain model is suited for PZT films with $x = 0.5$ and 0.6. The experimental values show a remarkable good match to the phenomenological theory, provided the right choice of the single-domain or polydomain model.

In chapter 7, PiezoMEMS consisting of PZT films, oxide electrodes and silicon membranes are fabricated using large area pulsed laser deposition. The films show a remanent polarization of 10 μC/cm^2, a dielectric constant of 1400 and a piezoelectric induced deflection at the center of 500-μm-diameter membrane of 17 nm/V at constant frequency well below its first resonance frequency, and 612 nm/V at the first resonance. The resonance frequency is found to range from 77.6 kHz to 1.2769 MHz for 1000 to 250 μm diameter membranes. A Q-factor of 236 to 87 for 1000 to 250 μm diameter membranes is observed. Interdigitated electrodes with a pitch of 5 μm were fabricated and show comparable functionality to parallel plate devices. A device geometry with a patterned bottom electrode results in improved wire bonding yield.

To conclude, these different topics demonstrate the relation between crystallographic and functional properties of epitaxial PZT films with thicknesses often used in applications such as PiezoMEMS. The effects of strain and composition and their mutual interactions show the freedom that is present to tune the functional properties of PZT thin films and its applications. The successful integration of high-quality PZT thin films with silicon opens a pathway to create perovskite oxide thin film devices with a large range of new functionalities.

Chapter 9

Samenvatting

De depositie van dunne lagen van perovskiete oxidische materialen op silicium wafers trekt veel aandacht, want het belooft massa-productie van dunne laagsystemen mogelijk te maken, die gebaseerd zijn op functionele eigenschappen zoals piëzo-elektriciteit, ferroelectriciteit, supergeleiding, magnetisme en diëlektriciteit. Piëzo-elektrische Micro Electro Mechanische Systemen (PiezoMEMS) bestaande uit $Pb(Zr_x,Ti_{1-x})O_3$ (PZT) lagen op silicium worden vaak gezien als voorloper in deze trend, met veelbelovende toepassingen zoals bijvoorbeeld inkjet printkoppen, piëzo-elektrische micromachined ultrasone transducers en energie-generators. De onlangs verkregen epitaxiale PZT dunne lagen van hoge kwaliteit op silicium substraten door middel van gepulste laser depositie bieden de mogelijkheid om de fundamentele relatie tussen ferro-elektrische en kristallografische eigenschappen te bestuderen. In deze epitaxiale lagen is het effect van de korrelgrenzen, gemengde oriëntaties, lading en kristal-dislocaties op de eigenschappen geminimaliseerd.

Dit proefschrift heeft tot doel de effecten van de mechanische rek- of drukspanning (hier genoemd: rek) en compositie op de kristal en functionele eigenschappen van PZT dunne lagen te bestuderen. Een groot bereik van rek en composities zijn bereikbaar en onderlinge interacties zijn bestudeerd. De lagen worden gegroeid in een geometrie inclusief elektroden met een laag-dikte die wordt gebruikt in toepassingen zoals bijvoorbeeld PiezoMEMS. Bij deze dikte zijn de lagen grotendeels gerelaxeerd van epitaxiale rek. Door de gepulste laser depositie op hoge temperatuur uit te voeren en de daaropvolgende afkoeling tot kamertemperatuur, wordt de thermische rek de dominante parameter voor het bepalen van de eigenschappen van de PZT heterostructuren. Domein vorming is een belangrijk aspect in PZT lagen en is sterk afhankelijk van de compositie. In het geval van een laag Zr-gehalte wordt de rek gerelaxeerd door de vorming van grote tetragonale domeinen, terwijl voor PZT in de buurt van de morfotropische fase grens (MPB), nanoschaal domeinen optreden met een onbekend rek-relaxatie mechanisme. Verschillende analytische modellen en thermodynamisch kunnen worden gebruikt om de kristallografie koppelen aan de functionele eigenschappen.

In hoofdstuk 3 worden verschillende aspecten van epitaxiale PZT heterostructuren op silicium beschreven. De fabricage en karakterisering worden toegelicht, gevolgd door een beschrijving van de groei van epitaxiale bufferlagen op silicium, de controle over de kristallijne oriëntatie van deze bufferlagen en de resulterende kwaliteit van de epitaxiale PZT heterostructuren op silicium. Het blijkt dat $SrTiO_3$ (STO) en YSZ bufferlagen epitaxiaal worden gegroeid. Het STO-gebufferde silicium substraat toont de de beste kristal kwaliteit en heeft derhalve de voorkeur voor het onderzoek naar de intrinsieke eigenschappen van de PZT lagen op silicium.

In hoofdstuk 4 wordt de relatie tussen domein-fractie, domein-kanteling en substraat-geïnduceerde rek in epitaxiale PZT lagen bestudeerd. Lagen met $x =$ 0,2, 0,4 en 0,45 zijn in de tetragonale c/a-fase en de domein-fractie blijkt sterk afhankelijk te zijn van de rek, terwijl de rooster-parameters constant zijn. Naast gekantelde a en b-domeinen, worden gekantelde c-domeinen waargenomen in de a en b-richtingen, waarbij de kantelhoek afhankelijk is van de rek. Hiervoor is een model afgeleid dat een goede overeenkomst heeft met de experimenten. Op silicium zijn de c-domein fracties laag en de fase benadert de a_1/a_2-fase, waarvoor verhoogde diëlektrische en piëzo-elektrische eigenschappen worden voorspeld.

De kristal eigenschappen nabij de MPB in PZT dunne lagen zijn onderbelicht in literatuur. Daarom worden PZT lagen met $x =$ 0,48 tot 0,52 geanalyseerd in hoofdstuk 5. Verschillende indicaties voor de aanwezigheid van een adaptieve fase met nanoschaal domein-texturen worden gepresenteerd. Een kleine of negatieve domein-wand energie resulteert in een domein-structuur waarin de domein-fractie sterk gevoelig is voor de rek en electrisch veld. Een homogene monodomeinstructuur is gemeten, dat verklaard kan worden door de röntgenverstrooiing effecten op nanoschaal domeinen. Piëzo kracht microscopie en transmissie elektronen microscopie suggereren de aanwezigheid van domeinen met een afmeting kleiner dan 20 nm. De adaptieve fase theorie uit de literatuur is aangepast voor PZT lagen met a, b en c-domeinen. De experimentele resultaten worden goed beschreven door de algemene invariantie voorwaarde dat de intrinsieke rooster parameters en de gemeten rooster parameters koppelt. Het blijkt dat deze relatie geldt als functie van compositie, substraat-geïnduceerde rek en temperatuur.

Hoofdstuk 6 laat het effect zien van de compositie en de rek op epitaxiale polydomein PZT lagen voor Zr-gehaltes $x =$ 0,2, 0,4, 0,5 en 0,6. Het afbeelden van de reciproke ruimte door middel van röntgendiffractie toont aan dat PZT lagen met $x =$ 0,2 en 0,4 in het tetragonale c/a-fase zijn, met $x =$0,5 in de monodomein r-fase zijn, en met $x =$0,6 in een polydomein rhombohedrische r/r-fase zijn. Vervolgens zijn het relatieve rooster-parameters / rek fase diagram, het temperatuur / rek fase diagram en rek / compositie fase diagram geconstrueerd en vergeleken met de Landau-Devonshire (LD) model van Pertsev en Kukhar voor bi-axiaal opgerekte dunne lagen. De transitie-temperatuur van PZT komt overeen met de LD-modellen. Ook de ferro-elektrische, diëlektrische en piëzoelectrische eigenschappen zijn vergeleken met de LD-modellen. De remanente polarisatie in de richting uit het vlak, beschrijft een inverse niet-monotone relatie tot de rek voor alle onderzochte fasen. De diëlektrische constante als functie van rek laat een niet-monotone relatie zien voor alle composities. De piëzo-elektrische coëfficiënten variëren maximaal 10 % voor PZT lagen met $x = 0{,}2$, 0,4 en 0,5 en 50 % voor PZT lagen met $x = 0{,}6$. Voor PZT lagen met $x = 0{,}2$ en 0,4, het polydomein-model van Kukhar komt overeen met de experimentele resultaten, terwijl het monodomein-model geschikt is voor PZT lagen met $x = 0{,}5$ en 0,6. De experimentele waarden vertonen een opmerkelijke goede match met de fenomenologische theorie, mits de juiste keuze voor het monodomein- of polydomein-model is gemaakt.

In hoofdstuk 7, PiezoMEMS zijn gefabriceerd, bestaande uit PZT lagen, oxidische elektroden en silicium membranen, met behulp van groot-oppervlak gepulste laser depositie. De lagen vertonen een remanente polarisatie 10 μC/cm^2, een diëlektrische constante van 1400 en een piëzo-elektrische geïnduceerde doorbuiging van 17 nm / V bij een constante frequentie onder de eerste resonantie frequentie in het midden van een 500 μm diameter membraan, en van 612 nm / V bij de eerste resonantie frequentie. De resonantie frequentie varieert van 77,6 kHz tot 1,2769 MHz voor 1000 tot 250 μm diameter membranen. De Q-factor varieert van 236 tot 87 voor 1000 tot 250 μm diameter van membranen. Geïnterdigiteerde elektrodes met onderlinge afstand van 5 μm zijn vervaardigd en laten vergelijkbare functionaliteit zien als parallelle plaat geometrieën. Een geometrie met een gepatroneerde onderelektrode resulteert in een verbeterde slagingskans van de ultrasone draad bevestiging (wirebond) methode.

Tot slot, de verschillende onderwerpen besproken in dit proefschrift tonen de relatie aan tussen de kristal eigenschappen en functionele eigenschappen van epitaxiale PZT lagen met een dikte vaak gebruikt in toepassingen zoals PiezoMEMS. De effecten van rek en compositie en hun onderlinge interacties laten de vrijheid zien die aanwezig is om de functionele eigenschappen van PZT dunne lagen en de toepassingen te bepalen. De succesvolle integratie van hoogwaardige PZT dunne lagen met silicium, opent een route om een groot aantal nieuwe functionaliteiten te gebruiken op basis van perovskiete oxidische dunne lagen.

Dankwoord

Nu komt een goed moment om even op adem te komen, ik hoop dat u dit proefschrift gelezen heeft met net zoveel plezier als ik het geschreven heb. De tijd voor een nieuw avontuur is gekomen, maar graag wil ik eerst een flink aantal mensen bedanken zonder wie dit onderzoek niet tot stand had kunnen komen.

Allereerst Guus, bedankt voor de grote vrijheid die je me hebt gegeven en het vertrouwen om zelfstandig een eigen onderzoekslijn te bepalen. Je kritische blik en visie op het vakgebied zijn fenomenaal. Evert, je oog voor detail en de essentie zijn indrukwekkend. Jouw enthousiasme voor de ferroelectrica is inspirerend en ik ben trots dat we in staat zijn geweest een aantal 'magische' verbanden te leggen. Gertjan, de altijd open deur en diepgravende discussies waardeer ik zeer. Mark, bedankt voor je enthousiasme en waardevolle adviezen, en ook voor het beschikbaar stellen van de STO/Si substraten die het onderzoek in deze vorm mogelijk maakten. Dave je interesse en aanmoedigingen zijn altijd een grote stimulans geweest.

Met veel plezier heb ik in het piezo-team gewerkt. In deze gevarieerde groep vullen we elkaar altijd goed aan: Xin, Minh, Matthijn en Evert bedankt! Arjen, bedankt voor de fijne samenwerking aan onder meer de contact-gas-wafer-heater en het large area-pld systeem. Met de studenten Kai, Werner, Bas, Miran, Tom en Daniel heb ik leuke onderzoeksonderonsjes meegemaakt. Ook de projectpartners, waaronder Solmates, Thermofisher, TSST en TST, en collega-onderzoekers van het SmartPie project waardeer ik zeer.

Graag wil ik de technici met de gouden vingertjes bedanken voor de prettige samenwerking en de goede sfeer in het lab: Frank, Dick, Henk, Dominic en Pino. Marion en José, bedankt voor jullie ondersteuning op administratief vlak. Verder alle collega's van de vakgroepen ICE, TST en BPI bedankt. Daarnaast wil ik graag de prettige samenwerking met het Mesa+ analyselab, de cleanroom staff en de service engineers van onder meer Bruker (Nano) noemen. En natuurlijk het schoonmaakteam, dat ervoor zorgt dat de naam 'de cleanroom' eer aan gedaan wordt. Natuurlijk wil ik alle geselecteerden van het IMS-futsalteam waarmee ik het genoegen heb gehad om een balletje te tika-taka-en bedanken!

Tot slot wil ik alle groepsleden van Inorganic Materials Science bedanken voor het uitstekende teamwork in en om het lab, de interessante discussies tijdens besprekingen en de gezelligheid op andere momenten. De altijd spraakmakende meningen, verhalen en grappen aan de koffietafel, vrimibo's, werkweken, conferenties, (zaal)voetbalwedstrijden en promotiefeestjes zijn onvergetelijk!

Ruud